Imperial College London
Department of Biomedical Engineering

Development of a platform for automated, two-photon targeted quad patch-clamping of neurons.

Gema Isabel Vera Gonzalez

A thesis submitted to Imperial College London for
the degree of Doctor of Philosophy and the Diploma of Imperial College

December 2022

Preface

This dissertation is the result of work carried out by the author in the Neural Coding and Neurodegenerative Disease Laboratory of the Bioengineering Department at Imperial College London in the period between October 2018 and December 2022. The work was supervised by Prof. Simon Schultz and by Dr. Stephen Brickley and was funded by the Doctoral Training Program (2018/2019) by the Bioengineering department.

This project is different from traditional PhD projects in that it is based on the work by Luca Annecchino, a previous PhD student, whose work was published in Annecchino et al. (2017). Furthermore, after my first year working on the project, another PhD student, Phatsimo Kgwarae, was brought on, as the amount of work was too extensive for a single person. Therefore, some of the work presented here was not exclusively conducted by me, but I have tried to attribute clear authorship where relevant throughout the thesis. In general terms, some of the software from Luca has stayed, but a great majority of it has been optimized and/or reprogrammed completely. None of the hardware on the rig stayed, with the exception of the single electro-pneumatic pressure system. Regarding the distribution between Phatsimo and I, anything relating to setting up the hardware and its maintenance was done by me (with the exception of the electronic pressure system), as well as any work related to the mice red(procuring them, handling them and finding ways to improve the fluorescence of our samples, which included various methods explained on the Methods chapter). Solution preparations and other 'wet' lab duties were also exclusively handled by me. I was the one with the manual patch-clamp expertise and biological background. On his side, Phatsimo had a more technological background to take care of the pressure system and to bring to fruition some of the software implementations (that we decided on together or that I suggested given my patch-clamp experience). That is not to say he did all of the programming, as much of it was done in collaboration. The software implementations that were done only by him have been attributed appropriately, but everywhere else, if no comments are made, the reader may assume that they were done collaboratively.

Statement of Originality

I declare that the contents of this thesis are entirely my own work, unless otherwise stated, and that any additional sources of information have been duly cited.

Copyright Declaration

The copyright of this thesis rests with the author. Unless otherwise indicated, its contents are licensed under a Creative Commons Attribution-Non Commercial 4.0 International Licence (CC BY-NC). Under this licence, you may copy and redistribute the material in any medium or format. You may also create and distribute modified versions of the work. This is on the condition that: you credit the author and do not use it, or any derivative works, for a commercial purpose. When reusing or sharing this work, ensure you make the licence terms clear to others by naming the licence and linking to the licence text. Where a work has been adapted, you should indicate that the work has been changed and describe those changes. Please seek permission from the copyright holder for uses of this work that are not included in this licence or permitted under UK Copyright Law.

Acknowledgements

First and foremost, I want to thank my supervisor, Prof. Simon Schultz for all the guidance he has provided over the years and for everything he has taught me, which has been invaluable towards the completion of this thesis. I also want to thank Dr. Stephen Brickley and Dr. Jesper Sjöström, for all their help throughout the PhD and for providing me with crucial insight on the neuro and patch-clamping parts of the project. Finally, on the mentor side, I'd like to thank Dr. Amanda Foust, for supporting me both in my teaching endeavors and funding opportunities, but also for all her optical expertise and help.

Special thanks go as well to Dr. Matteo Rizzi for providing invaluable assistance and knowledge with the virus injections and to all the CBS personnel that helped with the animal work. I also want to thank Dr. Nawal Zabouri for all her help and input during my final months of PhD, it was greatly valued and appreciated.

Of course, I also want to thank Phatsimo Kgwarae, my companion on this project, who has been indispensable not only scientifically but also personally on all those endless experiment days. He has been the best team partner anyone could ask for.

My utmost gratitude goes as well towards all the members of my lab, who have helped me at one point or another, and especially to those who also became friends I could rely on. Particular

thanks go to Dr. Carmel Howe, for having infinite patience with me in her role of postdoc (and almost big sister) and constantly giving me counsel, both in professional and personal matters. Likewise, I thank Dr. Sihao Lu for all his tolerance in explaining (more than once, thanks to my goldfish memory) how things work in the lab and solving my doubts. Also to Dr. Gerald Moore and Dr. Florian Zirpel for teaching me how to patch-clamp and handle animals. I also want to thank Jeevan, Ann, Seigfred, Yimei, Jina, Yu,... as well as those on the other labs I was lucky enough to be a part of: Airi, Christina, Hovy, Amanda,...

I also want to thank all my other friends in London, I shared with them truly the best moments throughout my PhD and they picked me up when most needed: Nuria, Javi, Nacho, Julià, Patri, Will, Aimee, Elena, Davide, Lisa and many others.

I also want to thank Alfredo, for all his love, and for showing me that life can always be better and happier.

Finally, I want to especially thank my family for their unconditional support that goes beyond what anyone could hope for. I could have never achieved anything I have without them. I cannot express how much I value them and love them.

Abstract

Whole-cell patch-clamp allows for the study of ion channel biophysics, membrane properties, and synaptic responses in intact brains. Multi-patching promises to elucidate the functional and connectivity properties of neuronal microcircuits, but the high skill and labour required (and low throughput) hinders its widespread dissemination. Automated multi-patching may solve this problem, but current 'blind' autopatchers are impractical for targeting non-primary cell types or perform connectivity studies. We have developed an automated two-photon targeted quad-channel patch-clamping technology platform for *ex vivo* electrophysiology, extending the system of Annecchino et al. (Neuron 2017, 95:1048-55), as a promising step towards an *in vivo* targeted, quad-patching setup.

The platform comprises a two-photon microscope, four micromanipulators (Sensapex/Scientifica) fitted with mechanical stability clamps (to improve pipette resistance against vibration, tissue deformation and pressure changes), custom-developed electronically-controlled pressure regulator, patch-clamp amplifier and DAQs. Control is via a custom-developed LabView program which acquires frames directly from the microscope. After each trial, pipettes are automatically cleaned and returned to their previous positions, allowing for their reuse. A 'follow' function is available to allow the user to move a single pipette and have the rest follow, both in the z and x/y coordinates, to facilitate patching in new, undisturbed brain regions. Temperature control for the perfusion system is also possible within the software. The output and cell information of each channel is automatically recorded for each trial. Basic injection and connectivity protocols are also available to run within the program, making the software a complete set for the basic needs of any experimenter, regardless of their skill set.

Our targeted quad patch-clamp system allows scalable and reproducible electrophysiology studies to be conducted across a variety of laboratory settings, offering for the first time robotically automated recording of subthreshold signals from multiple genetically and optically targeted cells simultaneously.

Contents

Preface i

Abstract v

1 Introduction to automated two-photon targeted whole-cell patch-clamp 1

1.1 Introduction and motivation 1

1.2 Two-photon microscopy 9

1.3 Overview of the technical specifications 10

1.3.1 Experimental setup 11

1.3.2 Pipette navigation and target cell engagement (image guided systems) . . 13

1.3.3 Automated analysis of images and visual feedback 13

1.3.4 Expanding to automated multi-patching 15

1.3.5 Control of pipette internal pressure 16

1.3.6 Practical considerations 18

1.4 Data Acquisition 19

1.4.1 Procedures for robotic 'blind' and image guided whole-cell recordings *in vivo* 19

1.4.2 Example recordings from 'blind' (single and multi-neuron) and targeted *in vivo* patch-clamp experiments 22

1.5 Performance evaluation 24

1.6 Overview 29

2 Methods **30**

2.1 Protocols 30

2.1.1 Internal solution for brain slices 30

2.1.2 Artificial Cerebrospinal Fluid (aCSF) solutions for *ex vivo* slices 32

2.1.3 Slicing protocol for *ex vivo* fluorescent slices 33

2.1.4 Slicing protocol for *ex vivo* non-fluorescent slices: bath loading of FURA 2-AM 36

2.1.5 Virus injections and other methods for the generation of fluorescent samples 39

2.2 Rig preparation for the start of the experiment 42

2.3 Software protocol for a typical experiment 43

3 Hardware Setup **45**

4 The software: RITA **51**

4.1 Introduction to RITA's algorithm 52

4.2 Preceding work: Annecchino system 55

4.3 Implemented changes, expansions and added functionalities. 57

4.3.1 New Interface 57

4.3.2 Paralellization: Re-entrant VIs. 61

4.3.3 Sensapex manipulator compatibility 62

4.3.4 Dual MultiClamp 700B interfacing 66

4.3.5 Temperature control 68

4.3.6 Central Processing Unit (CPU) Usage . . . 68
4.3.7 Experiment notes . . . 70
4.3.8 Current injection protocols . . . 71
4.3.9 Optimization of the targeting algorithm . . . 73
4.3.10 Follow manipulator function . . . 80
4.3.11 Pipette self-cleaning for reuse . . . 80
4.3.12 Manufacturing of the pressure system . . . 82
4.4 RITA's internal architecture . . . 82

5 *Ex vivo* results and validation for 'blind' multi-patching 88
5.1 Example of a pair of successfully patched cells . . . 89
5.2 Example of three successfully patched cells . . . 93
5.3 Example of four successfully patched cells . . . 94
5.4 Statistics . . . 94
5.5 Conclusion . . . 97

6 *Ex vivo* results and validation for two-photon targeted multi-patching 98
6.1 FURA 2-AM loaded slices . . . 99
6.1.1 Example of a pair of successfully patched cells . . . 99
6.1.2 Example of three successfully patched cells . . . 101
6.1.3 Example of four successfully patched cells . . . 104
6.1.4 Statistics . . . 107
6.2 Slices expressing GFP . . . 109
6.2.1 Example of a pair of successfully patched cells . . . 111

6.2.2 Example of three successfully patched cells . . . 112
6.2.3 Statistics . . . 118
6.3 Conclusion . . . 118

7 Final discussion and future work **119**

Bibliography **124**

Appendix A Instructions to install and assemble the standalone pressure system **133**

A.1 Hardware setup . . . 133
A.2 Software installation . . . 135
A.3 Troubleshooting . . . 136
A.3.1 PID values . . . 136
A.3.2 Arduino code . . . 137
A.3.3 Incorrect COM port . . . 138

List of Figures

1.1 Patch-clamp modes. 3

1.2 Patch-clamp process. 4

1.3 Connectivity between a pair of manually patched pyramidal neurons. 6

1.4 Connectivity between four manually patched pyramidal cells. 8

1.5 Single versus two-photon excitation. 10

1.6 Two-photon guided patch-clamp setup. 12

1.7 Shadowpatching. 14

1.8 Steps of the multipatcher algorithm from Kodandaramaiah et al. (2018). 15

1.9 Continuous pressure system schematic (simplified). 17

1.10 Discrete pressure system schematic (simplified). 18

1.11 Automated whole-cell patch-clamp procedure. 21

1.12 Example recordings from 'blind' (single and multi-neuron) and targeted *in vivo* patch-clamp experiments. 23

2.1 Slicing area picture. 35

2.2 CamKII-GFP (AAV9) p0 virus injection expression. 40

2.3 CamKII-GFP (AAV9) virus expression vs. FURA 2-AM bath loading expression. 41

3.1 Picture of the experimental setup. 46

3.2 Final configuration of the four manipulators, as seen by the position of the pipettes under infrared imaging. 47

3.3 CAD drawing of the mechanical clamps. 48

3.4 Close up of the experimental setup. 50

4.1 Pipette angles. 53

4.2 Algorithm for the targeted quad *ex vivo* mode presented in this thesis. 55

4.3 Algorithm for the targeted single *in vivo* mode presented in (Annecchino et al., 2017) 56

4.4 GUI of the software developed by Annecchino et al. (2017). 58

4.5 New GUI of the software. 59

4.6 New GUI of the software. 60

4.7 Pressure control VI. 62

4.8 Step VI structure. 64

4.9 Structure of manipulator query VI. 64

4.10 Send step VI for Sensapex manipulator. 65

4.11 Multiclamp Commander 700B. 67

4.12 VI for communication between RITA and MultiClamp Commander 700B. 67

4.13 Experiment notes. 71

4.14 Current injections protocol panel within RITA. 72

4.15 View of the four pipettes under two-photon microscopy at different focus planes. 76

4.16 Iterative vs. single axial approach target to tip distance (targeting optimization results). 78

4.17 Single axial approach algorithm results (distance between target and tip) before final calibration (targeting optimization). 79

4.18 RITA's cleaning controls. 80

4.19 CAD design for the cleaning Tergazyme wells. 81

4.20 Structure of RITA's main VI. 83

4.21 Structure of the Manipulator Daemon VI. 87

5.1 Stages of the automated multi patch-clamp process and corresponding pipette resistance and pressure changes in a 'blind' trial along time. 91

5.2 Current injections for two cells patched in 'blind' mode. 92

5.3 Current injections for three cells patched in 'blind' mode. 93

5.4 Current injections for four cells patched in 'blind' mode. 94

5.5 'Blind' patch success rate in brain slices. 95

5.6 Resting membrane potential, input and series resistance distribution of the cells patched by RITA in 'blind' mode. 97

6.1 A two-photon image of two patched neurons. 99

6.2 Stages of the automated process and corresponding pipette resistance and pressure changes in FURA 2-AM loaded slices for two patched cells. 100

6.3 A two-photon image of three patched neurons. 101

6.4 Stages of the automated process and corresponding pipette resistance and pressure changes in FURA 2-AM loaded slices for three patched cells. 103

6.5 A two-photon image of four patched neurons. 104

6.6 Stages of the automated process and corresponding pipette resistance and pressure changes in FURA 2-AM loaded slices for four patched cells. 106

6.7 Success rates for *ex vivo* trials using dye-loaded (FURA 2-AM) brain slices. . . . 107

6.8 Time to break-in, resting membrane potential, input and series resistance distribution of the cells patched by RITA in two-photon targeted mode (FURA 2-AM). . . . 108

6.9 CFS curves comparison for FURA 2-AM bath loaded slices and CamKII-GFP p0 injections. . . . 110

6.10 Current injections for two two-photon targeted patched cells (CamkII-GFP (AAV9) p0 injections). . . . 111

6.11 Example of a pair of successfully patched cells with GFP-CamkII (AAV9) expression. . . . 112

6.12 Stages of the automated process and corresponding pipette resistance and pressure changes for two successfully-patched GFP-expressing cells. . . . 113

6.13 Connectivity between two cells. . . . 114

6.14 Example of three successfully patched GFP-expressing cells. . . . 116

6.15 Current injections for three two-photon targeted patched cells (CamkII-GFP p0 injections). . . . 117

7.1 Possible algorithm for the *in vivo* mode. . . . 119

A.1 Numbered and labelled parts of the standalone pressure system. . . . 134

A.2 GUI of the Matlab App. . . . 135

A.3 GUI of the extended Matlab App that allows the user to adjust the PID values. 136

A.4 Reuploading the code to the Arduino Board. . . . 137

Chapter 1

Introduction to automated two-photon targeted whole-cell patch-clamp

1.1 Introduction and motivation

"As long as our brain is a mystery, the universe, the reflection of the structure of the brain will also be a mystery."

Santiago Ramon y Cajal

Despite all the years that have passed since neuroscientist Ramon y Cajal studied the structure of the brain, the number of unknowns seems to only keep growing. The indecipherable nature of the brain keeps attracting scientists from all backgrounds in an attempt to elucidate little pieces of the puzzle.

Following a top-down approach, technologies such as EEG (electroencephalogram) or EcoG (electrocorticogram) are extremely useful, as they provide waveforms that give insights into the general state of the brain. Following a bottom-up approach, however, it seems only reasonable to start by studying the most reduced unit of the system: the cells.

Excitable cells such as neurons have a tightly controlled internal milieu, with ion concentration gradients across the plasma membrane establishing a negative equilibrium potential of around -70 millivolts (mV). Ion channels, which are membrane-bound proteins that allow charged

molecules to cross an otherwise impenetrable phospholipid bilayer, are responsible for said equilibrium. Upon stimulation (such as neurotransmitters in ligand-gated ion channels), cells can increase their potential towards more positive values, until what is known as the threshold potential is reached. At this point, voltage-gated sodium channels (and/or calcium channels, depending on the cell type) change to their open configuration, triggering a huge influx of ions that further depolarize the cell, which marks the beginning of an action potential (AP). Voltage-gated potassium channels then repolarize the cell through an efflux of potassium ions, closing the cycle and finishing the AP. APs are key in cell-to-cell communication, as they are signals that can be directly transmitted or trigger chemical transmission of information to motor cells, glands or other neurons, through electrical and chemical synapses, creating a flow of information throughout the nervous system.

This electrical activity can be directly or indirectly monitored in several ways: from electrode arrays to calcium and voltage dyes, to individual recordings such as single patch-clamp. While each technology has its virtues and disadvantages, patch-clamp electrophysiology is among the most reliable methods for monitoring neuron function and determining cell type.

Despite the high dexterity required and relatively low throughput, it provides the highest temporal and spatial resolution among all of the techniques. It was first invented by Nobel prize winners Neher and Sakmann, in the 1970s (Neher and Sakmann, 1976), based on the knowledge produced by Hodgkin and Huxley with their axon squid experiments (Hodgkin and Huxley, 1939, 1952). Since then, it has been used to study cells with electrical activity, often neurons and cardiomyocytes (Hamill et al., 1981; Antzelevitch et al., 1991, 2007; Wellis et al., 1990)

There are many variations to the patch-clamp process, first described by Hamill et al. (1981). In its simplest form, the cell-attached, subtle suction (or the release of positive pressure) is used to create a seal between a cell and a pipette. Rapidly pulling out the pipette at this point leads to inside-out mode, while applying further suction without retraction leads to whole-cell mode. Gentle retraction from whole-cell mode leads to outside-out mode (Fig.1.1). Both inside-out and outside-out modes are used to study ion channels isolated from the rest of the cell, as small patches of membrane are attached to the pipette and can be tested in different conditions. Whole-cell mode is used to study the electrical activity of the cell, both supra and below spiking (AP) threshold. From now on, whenever we talk about patch-clamp, we will be

talking about whole-cell mode recording (WCR).

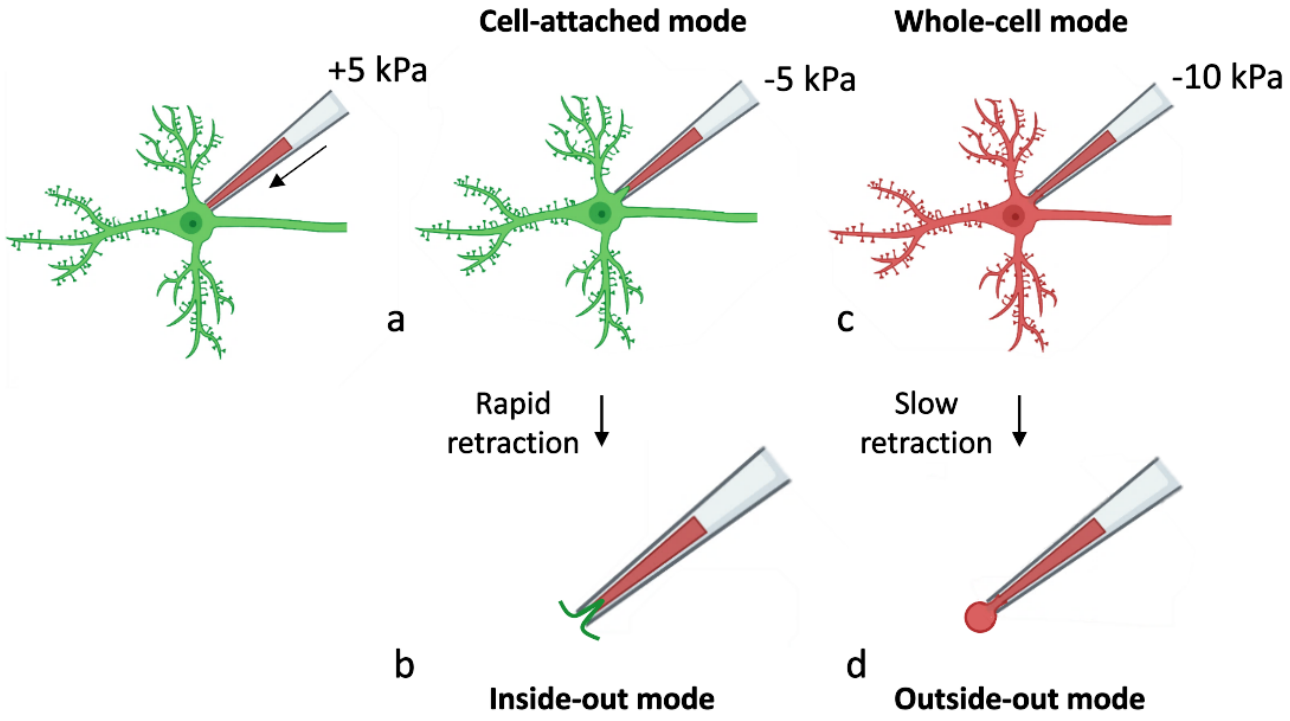


Figure 1.1: Patch-clamp modes. (a) Cell attached, (b) Inside Out, (c) Whole-cell, (d) Outside out. Figure adapted from Annecchino and Schultz (2018)

Therefore, in whole-cell patch-clamp mode, the glass micropipette (with an electrode inside) approaches the cell with positive pressure. This pressure is released upon dimpling of the membrane (as observed under infrared imaging, it is a 'bubble' that grows in size around the pipette on the cell, after initial contact between the pipette and the cell). At this point, negative pressure is applied if needed, until the tip forms a tight seal around the membrane. This is known as a gigaseal, because the impedance is in the gigaohm range (GΩ). Further suction is then used to create a small perforation in the cell membrane through aspiration; in this way gaining access to the electrical and molecular activity of a neuron in otherwise intact tissue (Fig. 1.2). The first time that a WCR was achieved *in vivo* was in anaesthetized cats by Pei et al. (1991), while the first WCR *in vivo* in mice was in 2001 by Margrie et al. (2001, 2002), anesthetized and awake respectively.

In the last decades, mice has seen a surge as a research model, owing to their cost-efficiency, reduced size and fast reproductive cycle, but also thanks to the wide variety of transgenic lines available. Owing to recombinant technologies that can alter their genome down to single nucleotides (Doetschman et al., 1987; Thomas and Capecchi, 1987), mouse lines representative

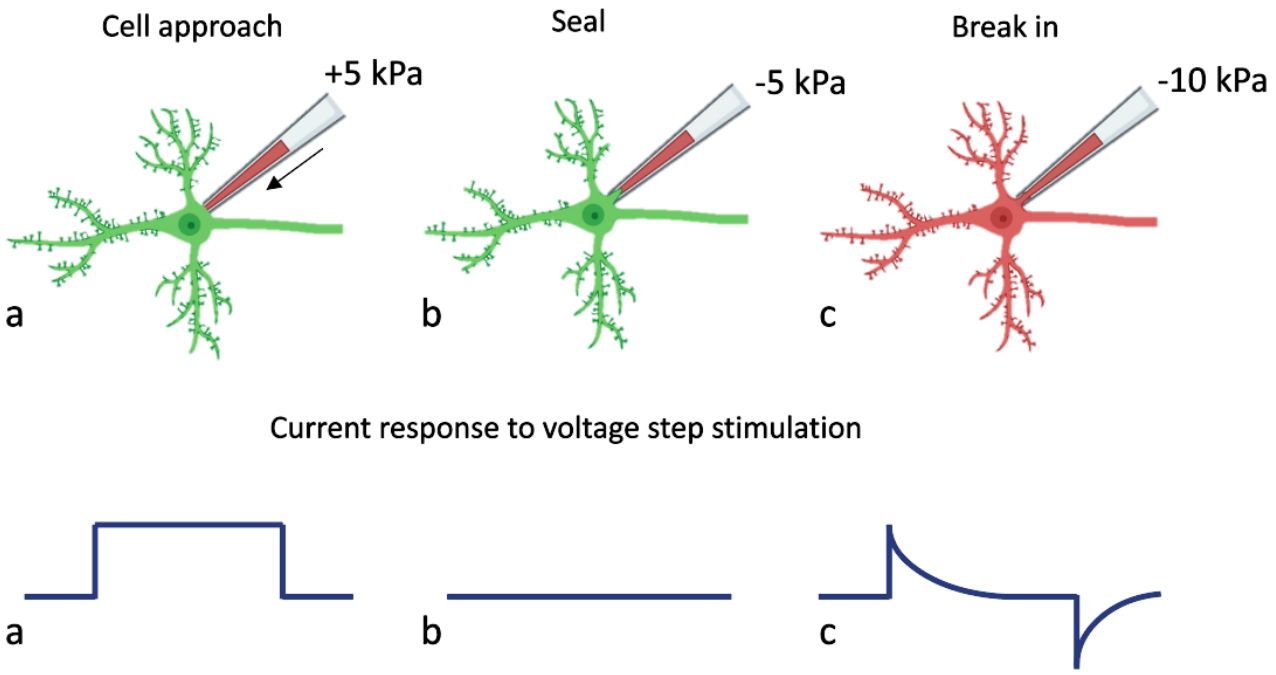


Figure 1.2: Patch-clamp process. (a) A periodic step voltage signal is sent to the electrode, while the current is monitored. A pipette with positive pressure slowly approaches the cell to be patched, until a dimple on the cell membrane can be seen. (b) Positive pressure is then released and negative pressure is applied (if needed) to form the seal. A successful seal (a seal in the gigaohm range), will yield a flattened current response. (c) Further negative pressure applied to the pipette will break into the cell, starting the whole-cell configuration. The current response (c, bottom) will then be characteristic to the capacitive properties of the cell membrane, where current applied to the membrane initially charges and discharges the cell membrane. If the break-in process is not successful, the signal will resemble the step function in (a).

of many diseases (e.g. 5XFAD for Alzheimer's), knock-in and knock-out lines for specific crucial genes in cellular processes, transgenic lines expressing fluorescent proteins and everything in between can be produced or is readily available. Furthermore, viral vectors that allow quick modification the expression of Green Fluorescent Protein (GFP) is often coupled with the desired genetic manipulation as an easy way to check the efficiency of the transfection, which makes these lines ideal for use in targeted patch-clamp (Mainen et al., 1999; Lundstrom, 2001; Fischer et al., 1998; Takada et al., 1997).

Robotic automation of the patch-clamp technique has improved throughput without compromising the quality and the duration of recordings (Kodandaramaiah et al., 2012; Annecchino and Schultz, 2018) and can encourage the widespread diffusion of the technique.

Combining automated patch-clamp with two-photon imaging allows selection of specific cell types and has the potential to integrate anatomical, physiological and pharmacological information, therefore reconciling target cell characteristics and network behaviour (Annecchino et al., 2017; Suk et al., 2017). Importantly, this provides us with the capability to test hypotheses concerning how circuits involving particular cells or cell types operate during physiological and pathological states. This method, known as TPTP (Two-Photon Targeted Patching) (Komai et al., 2006; Margrie et al., 2003), uses pipettes filled with a fluorescent dye and cells that express fluorescent proteins. The emission spectra of the fluorescent cells and the pipette dye must be sufficiently separate to allow the experimenter to differentiate dead cells that have been filled with the pipette dye through diffusion, from alive cells that express their own fluorescent proteins. Viral vector injections (Komai et al., 2006) or genetically encoded vectors in transgenic animals (Meyer et al., 2002) are traditionally used to produce tissues containing cells that express fluorescent proteins.

Patch-clamp also has the potential to provide even more complex biological information when combined with single-cell transcriptomics (Cadwell et al., 2016; Mun et al., 2020). For example, transcriptomic changes underlying neuronal computation and development can be effectively studied.

The advantages of robotic patch-clamp can potentially be even more impactful when attempting simultaneous recordings from multiple cells (Markram et al., 1997; Crochet and Petersen, 2006; Kodandaramaiah et al., 2018). Paired patch-clamp recordings enable unambiguous measurements of the connectivity between two neurons and allow testing for the presence of both electrical and chemical connections with high temporal accuracy, as well as revealing subthreshold correlations (Fig. 1.3). Comparable sensitivity enabling the detection of synaptic connectivity has not yet been routinely demonstrated with other techniques such as genetically-encoded calcium indicators (GECIs) like GCaMP, or genetically-encoded voltage sensors (Lin and Schnitzer, 2016; Yang and St-Pierre, 2016). Given the technical difficulty of performing multiple *in vivo* patch-clamp recordings, robotic automation appears very promising.

Although *ex vivo* and *in vivo* multi-patching has been conducted in neurons (Jouhanneau and Poulet, 2019; van Welie et al., 2016; Poulet and Petersen, 2008), the skill and labour required for multi-patching poses a challenge that has hindered its widespread diffusion (Kodandaramaiah et al., 2012). This challenge could be tackled by automating the process. Nevertheless, the use

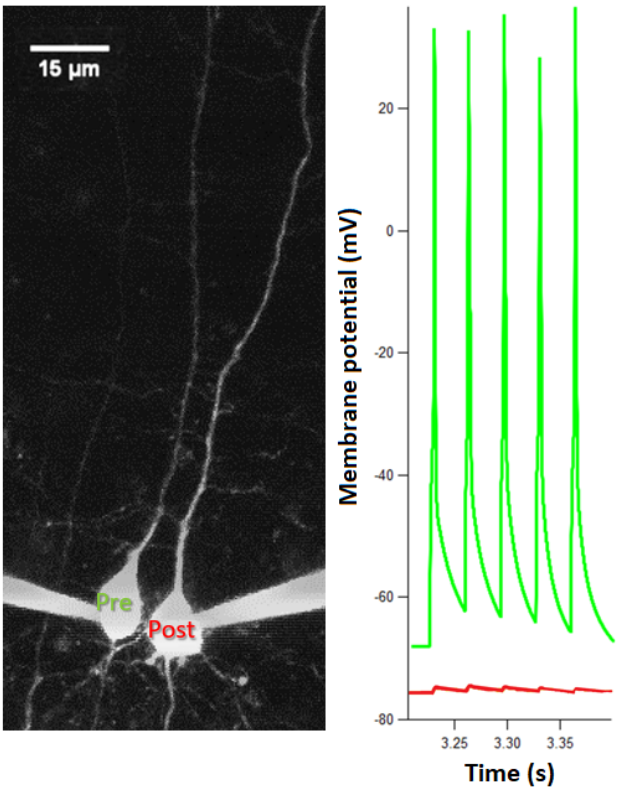


Figure 1.3: Connectivity between a pair of manually patched pyramidal neurons. (Left) Pair of current-clamped layer V pyramidal neurons in the primary visual cortex of a p13 (postnatal day 13) mouse. I patched them manually while learning how to do quad patch-clamp. The cell labelled Pre(synaptic) has an excitatory synapse onto the cell labelled Post(synaptic). (Right) Voltage versus time plot for the Pre (green) and Post (yellow) cells patched in the image. Excitatory Post-Synaptic Potentials (EPSPs) can be observed on the Post cell in response to a 50 Hz, 5-pulse excitatory train on the Pre cell, denoting a facilitating synapse from Pre to Post.

of the patch-clamp technique in live animal preparations has traditionally been limited to 'blind' (non-visually-targeted) recordings (Pei et al., 1994; Margrie et al., 2002). In this technique, cells are detected by a change in impedance and the first cells encountered on the electrode path are selected as targets. 'Blind' multi-patch-clamp has previously been automated *in vivo* (Kodandaramaiah et al., 2012, 2018). Although these systems can greatly improve throughput and might be the only option for deep structures in the brain (*in vivo*), they have several disadvantages. Firstly, it leads to a very reduced throughput for specific types of cells, such as interneurons, which are key players in brain function, but only account for approximately 15%-30% of the cortical cell population in rodents (Tremblay et al., 2016; Rubenstein and Rakic, 2013). Furthermore, in this kind of blind, automated multi-patching, the connections of neurons within a certain cell type (e.g. interneurons) cannot be studied, nor the specific connection between two different types of neurons (e.g. interneurons and relay cells or pyramidal cells and Martinotti cells). Not only that, but multi-patching without imaging can lead to a perceived false decrease in connectivity as this parameter is highly correlated to inter-somatic distance (Jouhanneau and Poulet, 2019); patching cells further than 200 µm away will likely decrease the chances of observing a connection, while patching too close without imaging can lead to the disruption of axons and dendrites of the previously sealed cells with the next pipette, which could destroy the connections. Moreover, since 'blind' systems detect cells based on changes of impedance, they tend to patch in the part of the cell membrane that was first encountered, rather than the slightly off-center position within cells that has been linked to the best seal-success rate (Zhao et al., 2022), and this has been linked to a decrease in yield (Holst et al., 2019). Hence, it is clear that many issues can be solved by using two-photon microscopy to target fluorescently labelled neurons. An example of the kind of connectivity studies that can be done when several cells are patched in a visually guided manner can be seen in Figure 1.4. In this sense, the number of cells patched is critical, as the number of possible connections for N neurons is N(N-1), meaning that a pair of neurons will only have two connections to check, whereas 3 neurons will have 6 and 4 will have 12 (Perin and Markram, 2013), as connections are directional and having one cell synapse onto another does not imply that the reciprocal is true. Therefore, it is key to find a good compromise in terms of the number of cells (that the system can patch) and how feasible in terms of complexity it is.

With increasing automation of other experimental steps - craniotomies (Ghanbari et al., 2019), trajectory obstacle avoidance (Stoy et al., 2017), pulsatile motion prediction and correction

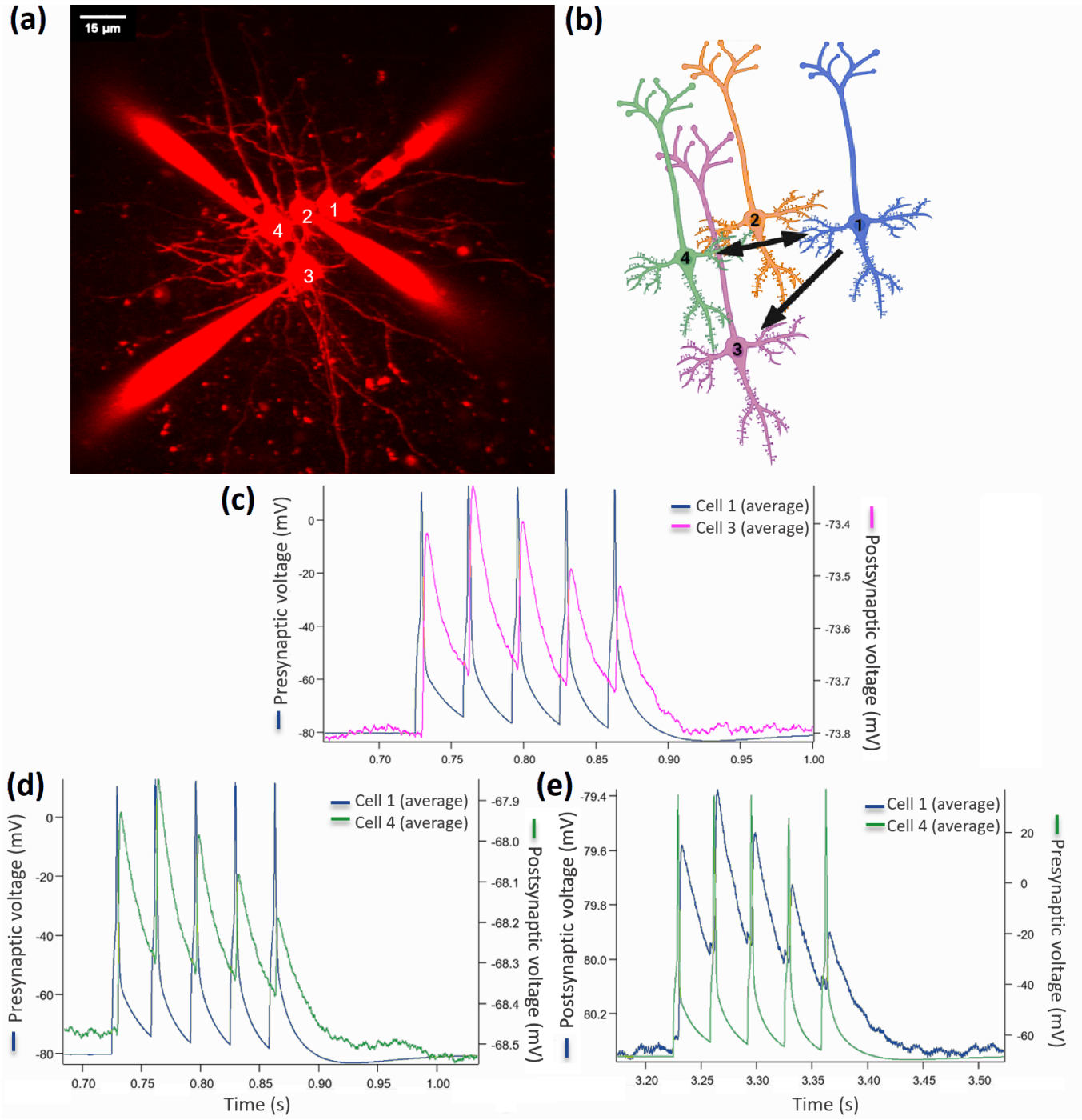


Figure 1.4: Connectivity between four manually patched pyramidal cells. (a) Four current-clamped layer V pyramidal neurons in the primary visual cortex of a p15 (postnatal day 15) mouse. I patched them manually while learning how to do quad patch-clamp. (b) Schematic representing the excitatory connections found between the cells, which were unidirectional from cell 1 to cell 3, and bidirectional between cells 1 and 4. Interestingly, cell 2, which was physically situated between cells 1 and 4 was not connected to any of the patched cells. (c) Voltage versus time for both the presynaptic cell (cell 1 in blue, left axis) and the postsynaptic cell (cell 3 in pink, right axis). The presynaptic cell was excited with a 50 Hz 5-pulse train, and EPSPs can be observed in the postsynaptic cell as a result. This connection was unidirectional. Traces are the averages of a 25-minute recording. (d) Same plot but for cells 1 (blue, presynaptic) and 4 (green, postsynaptic). (e) Same plot but for cells 1 (blue, postsynaptic) and 4 (green, presynaptic).

(Stoy et al., 2021) and pipette reuse (Kolb et al., 2016; Landry et al., 2021) - there is the potential for further reduction in experimental variability due to human factors.

1.2 Two-photon microscopy

Two-photon microscopy (2PM) relies on the near-simultaneous absorption by a fluorophore of two photons of lower energy and longer wavelength than those needed for one photon excitation (Fig. 1.5). Each photon carries roughly half the energy needed to excite the molecule, which will emit a photon of higher energy and shorter wavelength than the excitation photons when it returns to its original state. Due to their longer wavelengths (inversely proportional to their energy), usually in the near-infrared, the excitation photons have reduced scattering. I, the fluorescence intensity, is proportional to the density of the excitation photons, d, such that $I \propto d^2$ (Helmchen and Denk, 2005). Consequently, femtosecond lasers are used, as they provide a high flux of photons. Mode-locked titanium:sapphire (Ti:Sapphire) lasers are typically used, as they have high repetition rates (>10 MHz) for high power pulses. Low background noise is achieved without the need to use a pinhole (like in confocal microscopy), because the probability of near simultaneous absorption outside the excitation area is extremely unlikely (excitation volumes are as low as femtoliters). Both characteristics combined lead to a penetration depth of up to a millimetre, far greater than confocal microscopy. This is especially relevant in this project, as cells situated deeper into the tissue are likely healthier and have more intact connections than more superficial cells. Moreover, two-photon microscopy leads to reduced photobleaching and photodamage when compared to confocal microscopy (mainly due to the fact that in confocal microscopy the sample area illuminated by the energy source is bigger than in two-photon), which is highly relevant in long experiments (Denk et al., 1990). Closely followed by three-photon microscopy (which can provide depths of up to 1.3 mm), 2PM is the most widespread technique to image fluorescent features in live samples (Horton et al., 2013).

The laser light used in two-photon microscopy is usually modulated by Pockels cells and directed to the sample using galvanometric mirrors. Like a galvanometer, these mirrors rotate in response to the electric current passing through them, and are thus used to direct the laser onto the sample in a scanning fashion along the field of view (e.g. scanning each pixel, from left to right, for each pixel row, and then from top row to bottom row of pixels). The excitation

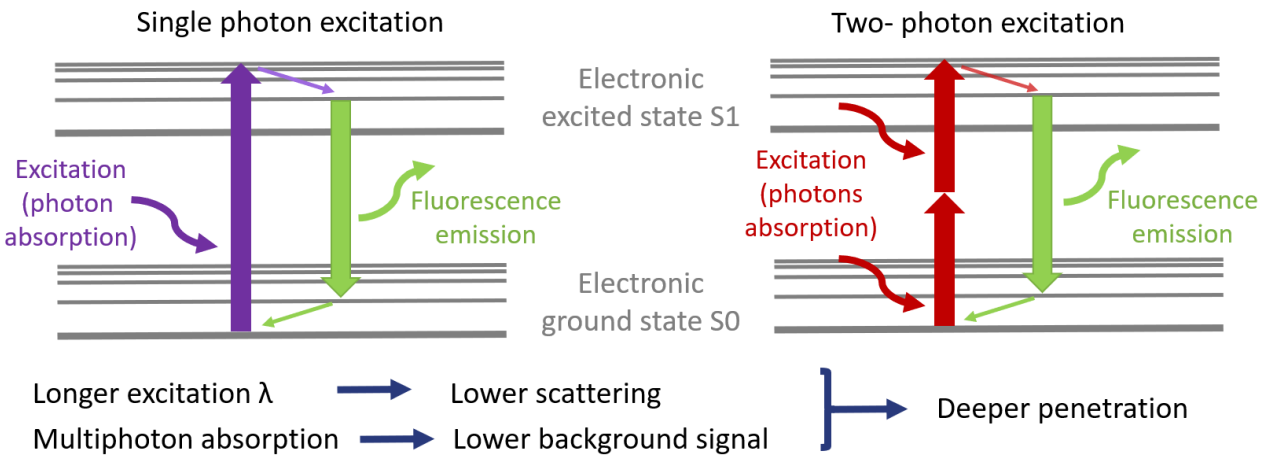


Figure 1.5: Single versus two-photon excitation. (Left) Excitation photon is absorbed by fluorophore, sending it to a higher electronic state. During the relaxation to the ground electronic state, fluorescence is emitted. (Right) Near-simultaneous absorption of two photons of half the energy (as compared to single-photon excitation) achieve the same fluorescence as in the first case, with several advantages: (1) Lower energy means longer wavelengths, usually in the near-infrared, which in turn leads to lower scattering. (2) Near simultaneous absorption is statistically unlikely outside the excited area, leading to a lower background signal. Both characteristics combined lead to deeper penetration than single-photon.

photons emitted by the sample are then split by a dichroic mirror and filtered to fit the spectra (commonly red and green filters) and finally collected by two photomultiplier tubes. The signals are transmitted to the computer where microscope acquisition software (e.g. SciScan in LabView or ScanImage in MATLAB) are used to adjust any necessary parameters. Due to non-linear interactions between the photons and the fluorophores' molecular structures, the excitation wavelengths used for 2PM are not exactly double that of the ones used in 1PM (Bestvater et al., 2002). As an example, Xu and Webb (1996) concluded that Rhodamine B, Fluorescein, and DiI have a two-photon fluorescence absorbance peak considerably lower than twice their one-photon peak wavelength.

1.3 Overview of the technical specifications

In the next subsections, common setup and algorithms for both 'blind' and two-photon targeted patching are discussed, with the actual systems being presented in the Performance evaluation section (1.5).

1.3.1 Experimental setup

Automatic whole-cell recording systems have been implemented using standard hardware and software available in conventional electrophysiological setups (Annecchino and Schultz, 2018). This includes one or more micromanipulators, a signal amplifier, a digital/analogue acquisition board, a data acquisition software and a personal computer. The only unconventional components are (1) an electro-pneumatic pressure regulator system to control the internal pressure of the pipette, and (2) an algorithm to monitor the pipette impedance signal in real-time, and execute pressure and manipulator controls accordingly. Such a system is sufficient for performing automated 'blind' whole-cell recording (WCR).

Two-photon guided WCR requires a two-photon microscope in addition to tissue labelled with fluorescent reporters (Fig. 1.6). To excite the sample, a commercial mode-locked laser (such as a Ti:Sapphire laser) and two galvanometric scanning mirrors (or alternative sample scanning device such as acousto-optic deflectors) are needed. The resulting fluorescence signal is split into specific wavelength bands by dichroic beam splitters and optical filters, and collected by one or more photo-multiplier tubes (detectors, PMTs). Two-photon images of fluorescently labelled cells are reconstructed and streamed, in real-time, to dedicated software responsible for object identification, target selection and tracking. Tracking information is then used to control the manipulator and adjust the trajectory and dynamics of pipette navigation towards the target. Finally, in both 'blind' and image-guided experiments, sealing and break-in are performed automatically by the computer-controlled pressure system.

There are also automated patch-clamp systems that use traditional upright bright-field microscopes with infrared light sources. In traditional bright-field microscopy, light is attenuated as it passes through the sample, thus making denser areas appear as darker than less dense ones. With the use of infrared light sources, penetration is improved. In thin brain slices, this type of microscopy is useful to image cells and other salient features. Differential Interference Contrast (DIC) is also commonly used in *ex vivo* mode. In this type of imaging, polarized light is split into two spatially separated optical paths that go through the sample and are combined before observation, with the contrast in the sample arising from their interference. These two types of imaging have been used in automated patch-clamp systems to do the cell tracking in brain slices, therefore being image-guided but not two-photon targeted. These systems cannot be used *in vivo*. The advantages and disadvantages of said systems are discussed in the

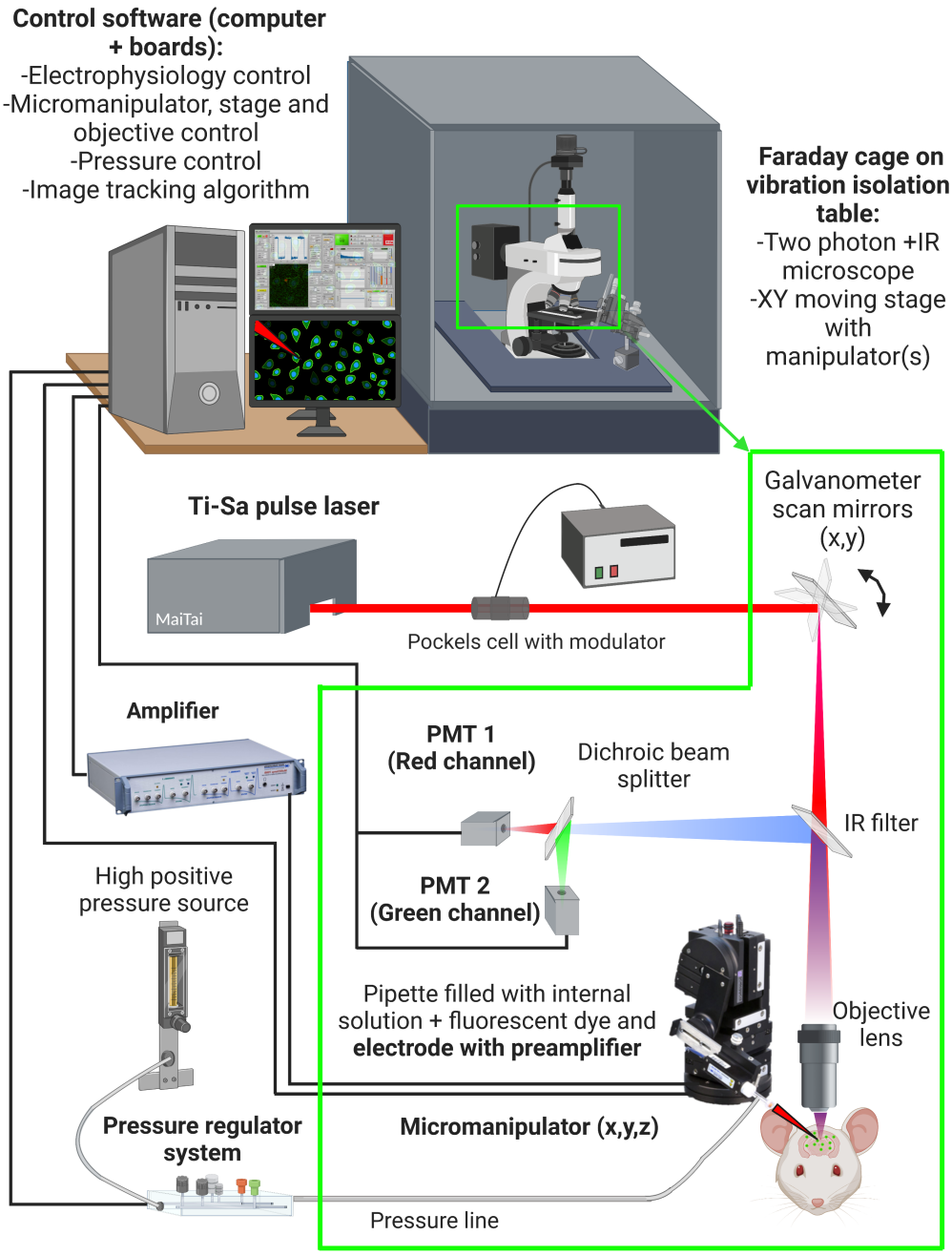


Figure 1.6: Two-photon guided patch-clamp setup. It consists of a conventional commercial two-photon microscope, a mode-locked Ti-Sapphire laser, a patch setup equipped with at least one programmable three-axis micromanipulator, a signal amplifier, an analogue to digital converter board, a computer, and a custom-made electro-pneumatic actuator for controlling micropipette internal pressure. 'Blind' patch-clamp is achieved with the same setup but excluding the imaging components (microscope and laser). For multipatching, more manipulators and amplifiers are required, and the pressure system and software expanded. Adapted from Annecchino et al. (2017).

Performance evaluation section (1.5).

1.3.2 Pipette navigation and target cell engagement (image guided systems)

The insertion of a sharp pipette into soft tissue leads to non-negligible mechanical strain and stress. The mechanical response of the tissue undergoing morphological deformation may change the shape and position of the target. Therefore we need to compensate for pipette-induced movements while moving the pipette through the tissue. One way to do this is by persistently monitoring the target and/or pipette position using a computer vision tracking algorithm, and using it to provide closed-loop visual servoing for controlling pipette navigation. Automatic fine control of the pipette position for navigation and target engagement relies on real-time analysis of the light signature of the fluorescent targets in the tissue. During the target engagement procedure, the position of the target is continuously reassessed and the approach trajectory of the pipette re-adjusted.

1.3.3 Automated analysis of images and visual feedback

Automated two-photon targeted patch-clamp systems developed so far have used similar image analysis methods, with some small differences such as programming language and image processing libraries used. OpenCV is an example of such a library, and is compatible with multiple platforms including Python, C, C++ and Java. It is used in the system by Wu et al. (2016)(Python). MATLAB (Mathworks, Natick, MA, USA) has a dedicated Image Processing toolbox and has been used by Long et al. (2015) and Suk et al. (2017), while similar capabilities are offered by the IMAQ suite available for LabVIEW (National Instruments, Austin, TX, USA), used by Annecchino et al. (2017), our predecessor.

Commercial two-photon microscope acquisition software (e.g. LabView-based SciScan, Scientifica Ltd, or MATLAB-based ScanImage, Vidrio Technologies LLC) can be used to acquire and stream image frames to an automated image analysis module in the system. Image averaging, optimisation and segmentation (Otsu, 1979), are then used to detect salient objects in the scene, separate bright cell(s)/pipette(s) from the background and identify candidate tar-

gets. The system described by Annecchino et al. (2017) performs local thresholding: a spatial modulation of the threshold value by dividing the image into windowed segments and then calculating a threshold value specific to that local neighbourhood of pixels. Global thresholding can be a viable approach if it accounts for inter-object intensity variation. Such an algorithm might involve performing multiple segmentations over a range of threshold values followed by a selection of the threshold value that gives the closest match for the target segment to a stored reference, similar to methods used by Wu et al. (2016); Suk et al. (2017). All salient objects are then geometrically classified in terms of area, contour, bounding rectangle and centre of mass and used to define a set of pixel masks. Measurements from pixel intensities within the masks can then be used to assess the depth and degree of focus of the neuron target(s).



Figure 1.7: Two-photon targeting versus shadowpatching. (Left) Two-photon targeting: fluorescent cells and pipette filled with fluorescent dye against a non-fluorescent background. (Right) Shadowpatching: Fluorescent dye flows out of the pippette into the brain, and it diffuses throughout the tissue but not inside the cells, due to their cell membranes, which act as a barrier.

Focus and depth can be assessed by measuring the sharpness of the identified object contour. This can be calculated as the difference between the average intensity of the pixels belonging to the internal boundary region of the object and the average intensity of the pixels belonging to the external boundary region, normalised by the average intensity of pixels within the internal boundary region (Annecchino et al., 2017). The target's depth is taken as the z-position of the focal plane of maximum contrast or intensity. A different approach should be adopted for target tracking, however, if 'shadowpatching'. In this technique, an extracellular dye is used to produce 'shadows', so that the cells appear as dark shapes within a fluorescent background (Kitamura et al., 2008) (Figure 1.7). In this context, the reduced axial variation in the fluorescence signal one would have with individually labelled neurons, makes it more challenging to determine

a target's z-coordinate. An alternative tracking approach could be based on morphological feature matching to establish and follow a target's position.

On *ex vivo* (brain slices) systems using infrared imaging, similar image processing algorithms have been developed, many of them making use of artificial intelligence to automatically detect cells and pipettes based on their shape and contrast (Koos et al., 2021; Kolb et al., 2019).

1.3.4 Expanding to automated multi-patching

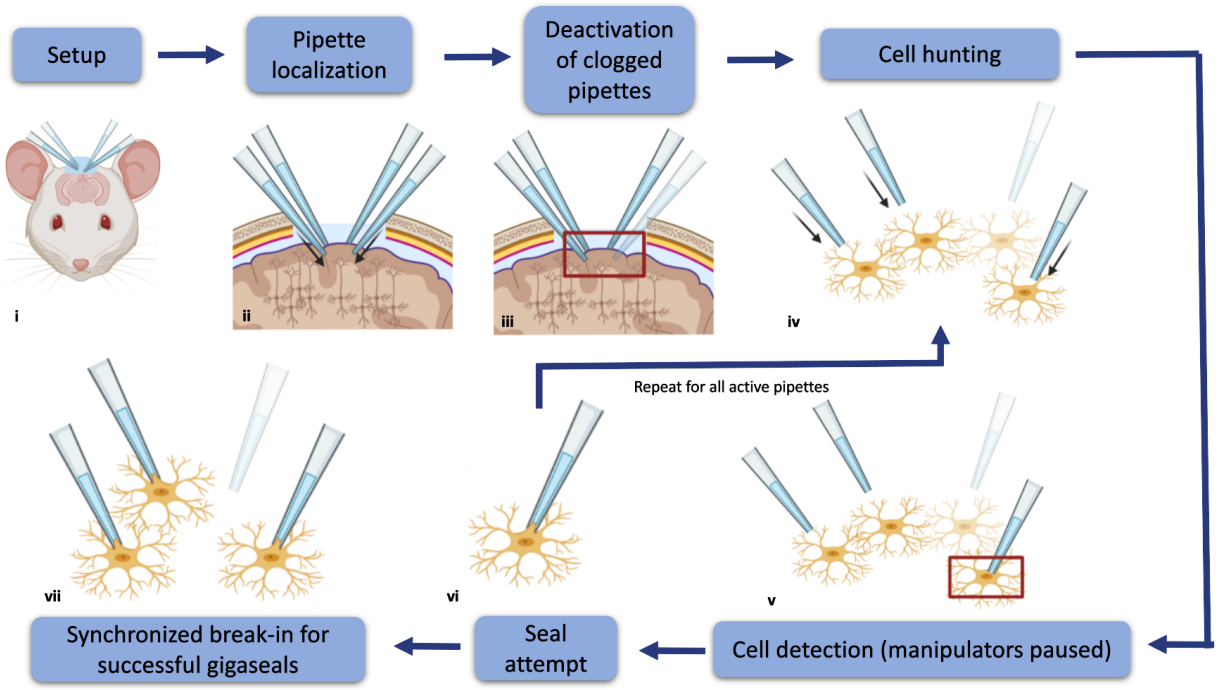


Figure 1.8: Steps of the multipatcher algorithm from Kodandaramaiah et al. (2018). (i) Manual positioning of the pipette tips on the brain surface. (ii) Automatic positioning of the tips over the target brain region and initiation of neuron hunting. (iii) Deactivation of clogged pipettes. (iv) Simultaneous movement of the tips in small steps until (v) a cell is detected. (vi) Sealing is initiated while all other pipettes remain motionless. Steps (iv)-(vi) are repeated until all pipettes have attempted a seal. (vii) Break-in is attempted in seals with resistance above 1 GΩ, simultaneously. Adapted from Kodandaramaiah et al. (2018).

Robotic patch-clamp has been scaled up to allow the independent control of up to twelve manipulators in brain slices (Perin and Markram, 2013) and up to four pipettes in *in vivo* (Kodandaramaiah et al., 2018), both with lower success rates than the single equivalent counterparts. The relative decrease in performance when attempting multiple recordings is related

to the fact that each pipette moves and creates additional tissue deformation that affects all cells. Furthermore, in 'blind' patching, the pipettes encounter different cells at different times. This can be challenging especially when it is critical to prevent any relative motion between the pipette tip and the target cell (i.e., during sealing). Additionally, in a 'blind' paradigm there might the possibility of pipette collision if the pipettes are not positioned far away from each other. Visual targeting can likely prevent pipette collision and potentially enable strategies to compensate for tissue and target deformation induced by multiple penetrating pipettes, but it does not eliminate them completely. Additionally, concurrent navigation control of multiple pipettes and the tracking of their target cells can be a comparatively demanding task due to the limited imaging area. Generally, for 'blind' patching, an all-at-once strategy whereby sealing is attempted at the same time after all pipettes are in close contact with their target cell, appears to be less successful than a one-at-a-time strategy, whereby pipettes seal their respective cells when encountered, while the rest of the pipettes pause the hunting and only resume once sealing finishes (Kodandaramaiah et al., 2018). The steps of the multipatcher algorithm by Kodandaramaiah et al. (2018) are depicted in Fig. 1.8, which was used as guide to design our 'blind' algorithm. In the case of targeted, however, it is possible to program the pipettes to arrive to the cells at the same time (because the position is known), so it is possible to both have the pipette seal the cell upon arrival (to optimize sealing possibilities) and for all pipettes to do it at the same time (to avoid tissue deformation during this critical process).

1.3.5 Control of pipette internal pressure

The precise and timely control of the pipette internal pressure is crucial for i) keeping the pipette tip clean, ii) obtaining a good seal, and iii) effectively rupturing the cell membrane and achieving a stable whole-cell recording configuration that will yield a high quality recording. Traditionally, the pipette internal pressure is controlled manually by means of a three-way valve and a syringe, and the experimenter uses their mouth to apply suction to help form the seal and break into the cell (Hamill et al., 1981; Margrie et al., 2002; DeWeese, 2007). Several custom-built electro-pneumatic control devices have been implemented as part of robotic 'blind' and image guided patch-clamp systems (Kodandaramaiah et al., 2012; Perin and Markram, 2013; Wu et al., 2016; Annecchino et al., 2017; Suk et al., 2017; Holst et al., 2019; Peng et al., 2019; Kolb et al., 2019; Koos et al., 2021) but they can also be used as part of classic manual patch-

clamp setups to minimise human error and increase precision and sensitivity. These pressure systems have generally been of two types: discrete or continuous, depending on whether the pressure output can only be a limited number of set values (discrete) or the full range is available *continuous*).

Continuous systems like the work of Annecchino et al. (2017) typically employ solenoid valves, one or more pressure sensors, a positive pressure source (air pump, compressed air tank or outlet) and either a negative pressure source or a vacuum ejector (Fig. 1.9). All the components can be connected by silicone or polyurethane tubes or alternatively attached to a plastic platform with drilled-in reservoirs (Annecchino et al., 2017). The airflow through each valve in the system can be controlled with some basic electronic components and data acquisition/control board (i.e., National Instrument DAQ Boards) or a dedicated micro-controller (i.e. Arduino board) running a proportional-integrative-derivative (PID) algorithm for closed-loop control of the pressure (see Annecchino et al. (2017)). Another option for continuous output is using syringes placed on a syringe pump, which imitates more closely the manual version of a pressure system for patch-clamp. Discrete systems usually have regulators that change the

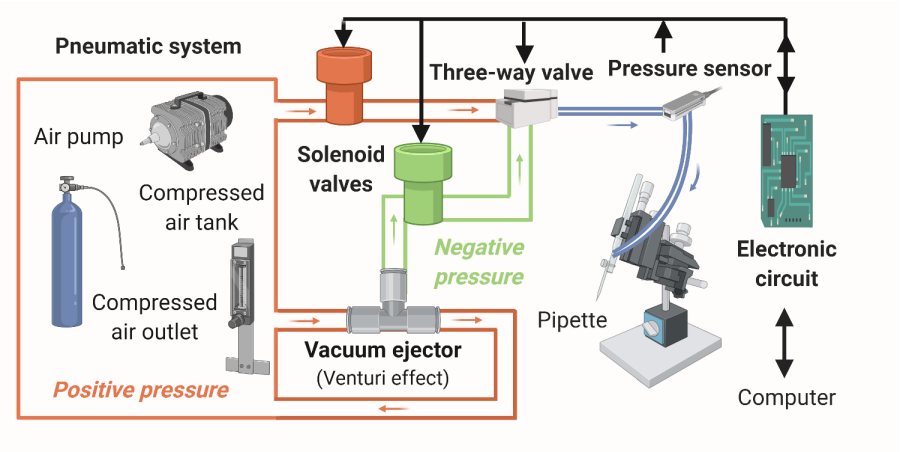


Figure 1.9: Continuous pressure system schematic (simplified). Solenoid valves modulate the airflow in the system to maintain a stable pressure output. The solenoid valves are controlled by a closed-loop control algorithm in an electronic circuit. Negative pressure (suction) can be generated by a vacuum ejector or alternatively sourced from another pump or reservoir. A 3-port valve selects either the positive or the negative pressure branch to the output to manipulate the pipette internal pressure. The sensor is positioned as close as possible to the output. A microcontroller or electronic circuit reads the pressure signal(s) from the sensor(s) and regulates all the valves as required. The black arrows represent the communication direction between the different elements.

positive/negative pressure supplied by the corresponding pressure source to two specific values: 'high' and 'low' pressure, for both positive and negative, giving a total of four set pressure channels, and five including the atmospheric pressure. The set pressure values can then be connected or disconnected from the pipette tip by all-or-nothing valves. Thus, the pressure supplied to the pipette tip can be switched between these five set values in a simple yet effective way 1.10. These systems, like the one in (Kodandaramaiah et al., 2018), are slightly more limited than continuous systems, which can adapt the pressure value to the particular situation.

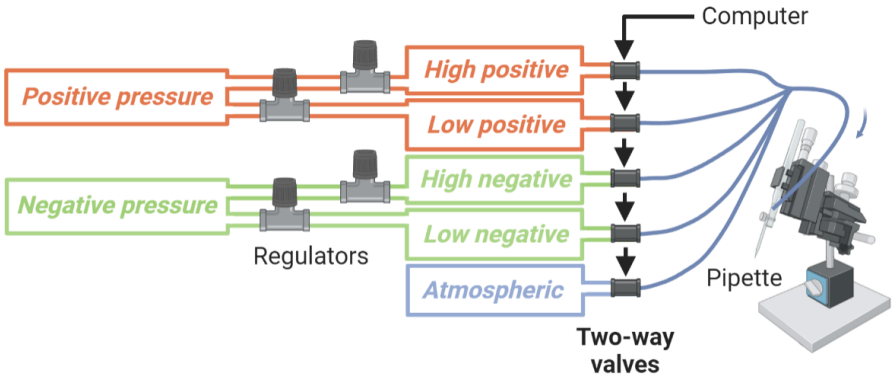


Figure 1.10: Discrete pressure system schematic (simplified). Regulators modulate the airflow to produce four stable set pressure outputs. Only one two-way valve is open at a time, relaying the desired pressure to the pipette tip.

An automatic pressure control system is also necessary to automatise a pipette cleaning process and afford the possibility of reusing the same pipette for multiple patching attempts by cleaning them in between trials (Kolb et al., 2016).

These electro-pneumatic systems can be assembled relatively easily, with instructions available in Desai et al. (2015); Kodandaramaiah et al. (2016); Wu and Chubykin (2017), or bought commercially (Sensapex, 2021; NeuromaticDevices, 2021).

1.3.6 Practical considerations

The patch pipettes and capillaries typically used for automated patch-clamp are the same as those used in manual methods.

For two-photon guided experiments, the internal solution is augmented with a fluorescent dye (e.g. 50 μM Alexa Fluor 594) to make the pipette visible under laser excitation.

Dye filled pipettes under positive pressure can release large amounts of fluorescent internal solution and create substantial background fluorescence. This will eventually degrade image contrast and the ability to visualise the pipette and target cells. One alternative to fluorescent dyes is coating the pipettes with quantum-dots to make them visible under two-photon imaging while avoiding diffusing fluorescent internal solution and degrading contrast. Quantum-dot-coated pipettes seems to be visible even at larger depths when compared to dye filled ones and yield recordings of comparable quality to non-coated glass pipettes (Andrásfalvy et al., 2014). This technique, however, comes with increased associated cost and adds steps to the experiment preparation time.

Pipette tip coordinate updates often rely on position readouts from the micromanipulator. If this is the case, one should bear in mind that these position values carry some level of uncertainty due to the limited precision of the micromanipulator. In addition, unwanted movements from drift and backlash may compound errors even further. These are unintended movements when the device is stationary and excess movements at the end of intended motions respectively. Therefore, when selecting micromanipulators, consideration should be given to devices with the highest precision, drift and backlash control. Also worthy of mention is the fact that old manipulators tend to become more imprecise and may drift, which is acceptable in manual patch but will lead to imprecise approaches in autopatchers. Alternatively, there are algorithms that reacquire the pipette coordinates along the approach, to assure optimal targeting.

1.4 Data Acquisition

1.4.1 Procedures for robotic 'blind' and image guided whole-cell recordings *in vivo*

Depending on the level of automation, the system can automatically perform all the steps involved in the patch-clamp experiment or only a subset. In image guided experiments, object identification and tracking information control manipulator movements that guide pipette

navigation towards the target. In 'blind' experiments, however, the algorithm makes decisions and executes timed actions solely based on the temporal trajectory of the pipette impedance. The simplified stages of an automated algorithm for both 'blind' (B) and image guided (I) experiments are presented in Fig.1.11 and described as follows:

- **Setup (B/I):** The experimenter fills the pipette(s) with internal solution (B) augmented with a fluorescent dye (I), then loads it into the pipette holder and automatically sets the internal pressure to a relatively high value (50-100 KPa). The pipette(s) is manually placed at the centre of the field of view (I) or craniotomy (B) and is manually or automatically driven to the desired depth (i.e. brain surface).

- **Start imaging (I):** The low-magnification objective is exchanged for a water immersion objective. The objective is lowered until in contact with the liquid, at which point image acquisition can be initiated. The dye-filled pipette tip and fluorescently labelled cells (in two-photon guided) are visualised. A computer vision algorithm identifies objects within the streamed images.

- **Acquire pipette tip and target location (I):** The imaging system focuses on either the pipette(s) or the target(s), then these are automatically detected or selected manually and their location coordinates stored. The system automatically calculates the path of the pipette(s) to the target(s).

- **Cell hunting (B/I):** The pipette internal pressure is reduced to a lower positive value ($\sim$10 KPa or 5Kpa). If the pipette is not blocked (determined by the impedance), the manipulator is moved (usually in small steps $\sim$2 μm) until a cell is encountered (B) or the targeted cell is reached (I). (I) In iterative algorithms, the system continually monitors the target position and makes adjustments to the pipette trajectory to compensate for any tissue movement until the target is engaged. Note that while this step occurs in both 'blind' and two-photon targeted mode, in the former case it is true 'hunting', whereas in the latter, the presence of a cell in the locality is known, and the goal of the movement is merely to reduce the cell-pipette distance.

- **Cell detection (B/I):** A monotonic increase in impedance levels over two or more consecutive steps implies that a cell has been detected.

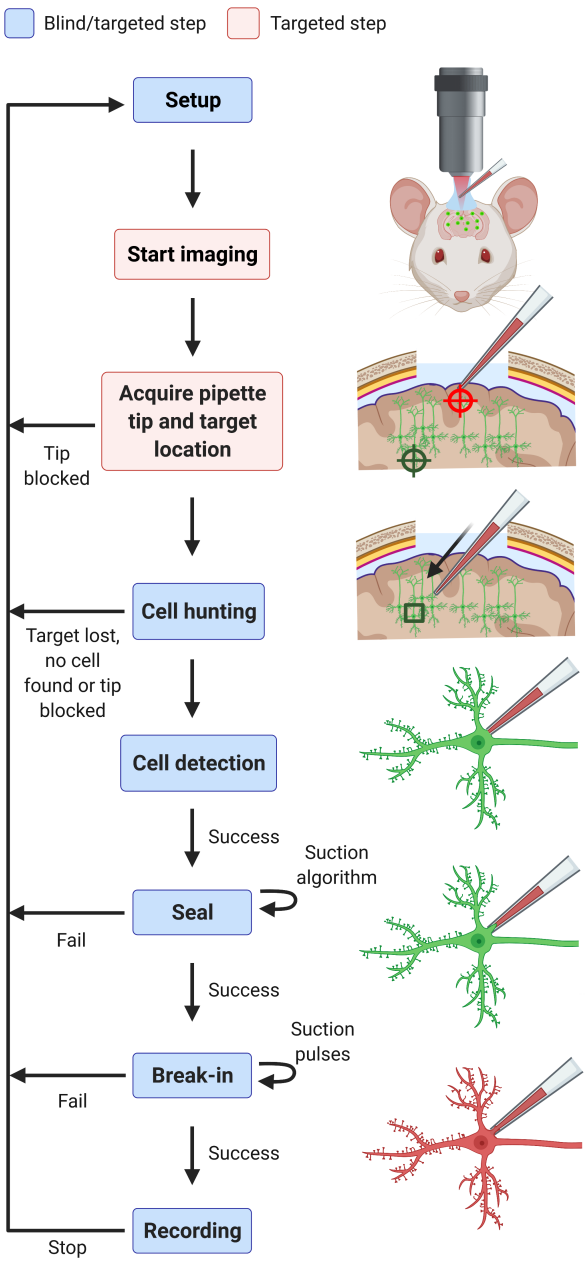


Figure 1.11: Automated whole-cell patch-clamp procedure. (Left) Block diagram of the automated patch procedure. Steps in blue are common to both 'blind' and targeted patch while additional steps for the image guided patch are shown in light red. (Right) Schematic representation of the robotic patching procedure: Setup and pipette placement, tip and target coordinate acquisition (either manual or automatic), pipette positioning, automatic approach, target cell detection, seal formation, and break-in followed by whole-cell recording. Adapted from Annecchino et al. (2017).

- **Seal (B/I):** At this point, the system automatically releases the internal pressure to allow the cell membrane to establish contact with the tip. To facilitate the seal formation, the pipette potential can be set to a negative value close to that of the intracellular potential

of the cell ($\sim$ -65 mV). Light suction may be applied to form a tight seal. These steps can be executed through a set of control algorithms. Seal formation is complete when the pipette resistance remains at or is higher than a user defined seal threshold (usually 1-1.5 GΩ or 'gigaseal').

- **Break-in (B/I):** A WCR is achieved by breaking the patch membrane with one or more suction pulses. The automatic detection of a drop in the impedance signal and characteristic current signal (see Fig. 1.2) indicates a successful break-in.

- **Cell recording (B/I):** A successful break-in and viable WCR configuration is confirmed (1) electrophysiologically by verifying properties like membrane potential, firing properties, access resistance (B/I) and also (2) optically observing the gradual filling of the target cell with fluorescent internal solution (I). At this point the recording can begin.

1.4.2 Example recordings from 'blind' (single and multi-neuron) and targeted *in vivo* patch-clamp experiments

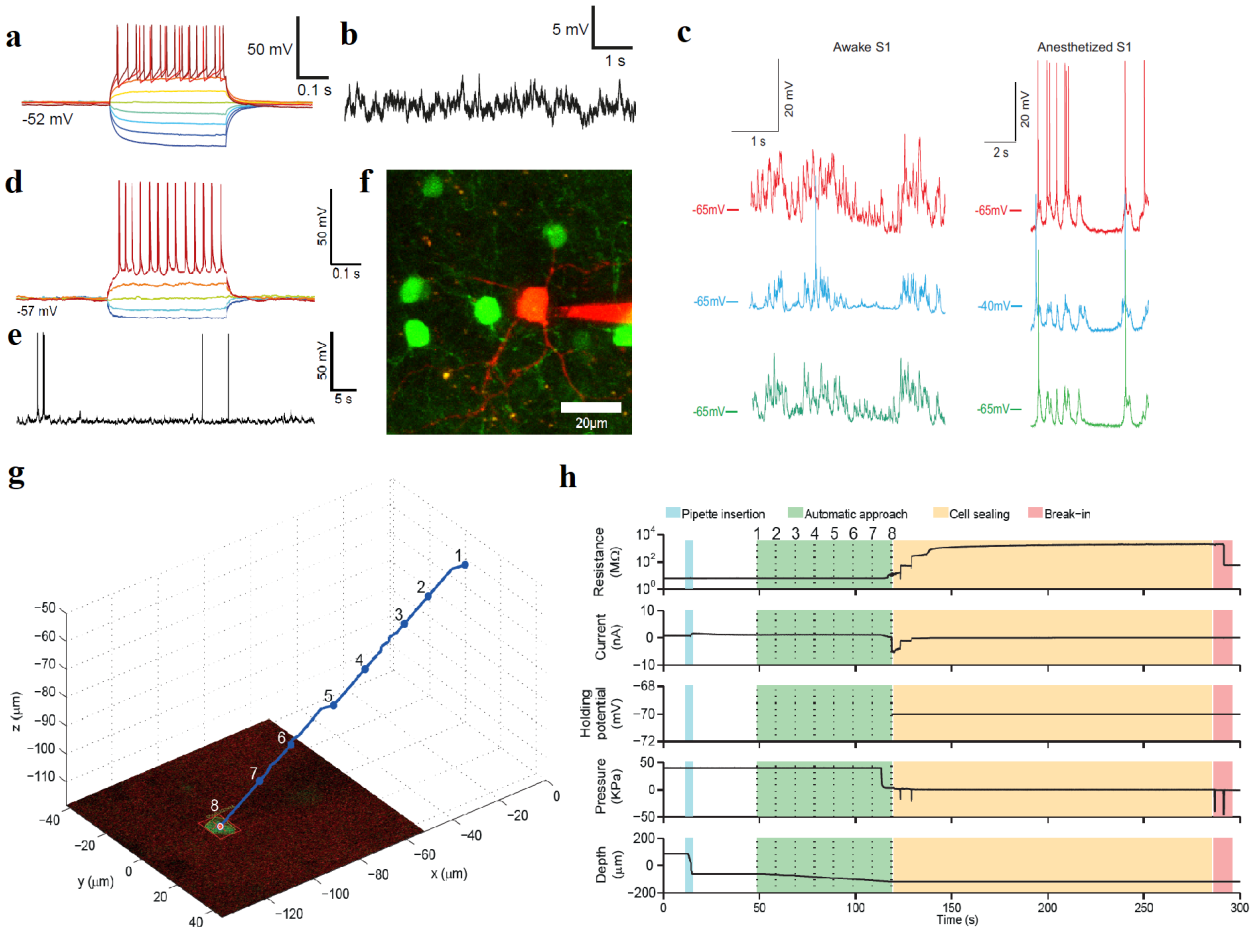


Figure 1.12: Example recordings from 'blind' (single and multi-neuron) and targeted *in vivo* patch-clamp experiments. (a,b) Example of an automatic 'blind' whole-cell single recording *in vivo*. (a) Intrinsic response of a neuron in the mouse cortex during hyperpolarising and depolarising current injections applied through the recording pipette electrode (400 ms-long pulses from -100 to +100 pA in 25 pA steps) and (b) recording for the same neuron at rest. Figures adapted from Annecchino (2016) (c) Examples of automatic 'blind' whole-cell multi-recording *in vivo*. On the left, voltage recordings from three different neurons that were patched at the same time in S1 (somatosensory cortex) of an awake head-fixed mouse. On the right, same but for anaesthetised. Figures adapted from Kodandaramaiah et al. (2018) (d,e) Example of a robotic two-photon targeted whole-cell single recording *in vivo*. Same as (a,b) but for a GAD67-GFP positive interneuron in the mouse cortex. Current injected in 400 ms-long pulses from -100 to +100 pA in 50 pA steps. Figures adapted from Annecchino et al. (2017) (f) Two-photon image of the same neuron as (d,e). (g,h) Pipette approach trajectory and state during a typical robotic two-photon targeted single patching process.(g) Automatic navigation of the pipette toward the target cell, with real-time feedback control of trajectory enabled.(h) Example of time-courses of pipette resistance, current, holding potential, internal pressure and pipette depth during the patching procedure (stages color coded; numeric labels correspond to points on the approach trajectory in (g). Time intervals relative to the different stages of the automated patching algorithm are colour coded. Figures adapted from Annecchino et al. (2017)

1.5 Performance evaluation

Success rates for automated experiments *in vivo* have matched or exceeded manual approaches (Annecchino and Schultz, 2018). However, both *in vivo* and *ex vivo* (brain slices) experiments are still very dependent on high quality experimental preparation, and good internal solution composition.

Table 1 has a summary of the *in vivo* and *ex vivo* systems developed thus far. The *in vitro* (cultured cells) automated systems are not included here due to their already successful and commercialized automation. While patching cultured cells is not nearly as complex as *in vivo* and *ex vivo* systems (and thus they have a reduced need for automation in terms of learning curve), they can gain from higher throughput. Examples of these systems in use can be seen in the work of Finol-Urdaneta et al. (2022) (SyncroPatch 384 by Nanion Technologies) and Lukacs et al. (2021) (IonFlux Mercury by Fluxion Biosciences). For more information on automated patch-clamp in planar arrays, see Annecchino and Schultz (2018); Dunlop et al. (2008); Okada (2012).

The autonomous degree in Table 1 represents the steps that have been automated within the patch-clamping pipeline according to the following:

[1] Pulling pipettes

[2] Filling the pipette with internal solution

[3] Placement of the pipette on the electrode holder

[4] Pipette detection under microscope

[5] Navigation of the pipette towards sample

[6] Final cell approach

[7] Pressure control

[8] Sealing and break-through

[9]Reuse of pipettes through pipette cleaning

However, it should be noted that these are not the only steps being automated, as the first strides towards the automation of craniotomies have been taken (Ghanbari et al., 2019; Rynes et al., 2020).

The time column represents the minutes that the automated steps took, which is relevant not only for time-efficiency purposes but also for yield, as there is a negative correlation between time taken to break-in from pipette insertion and its success rate (Jouhanneau and Poulet, 2019). Yields should, however, be evaluated cautiously as each platform had slightly different conditions for considering a whole-cell recording successful and different techniques are expected to have different yields. For example, 'blind' patching has higher yields than two-photon targeted patching (Jouhanneau and Poulet, 2019), as demonstrated by the fact that Annecchino et al. (2017) had 51.4% success rate when 'blind' patching, which is far above the reported 22.2% for targeted. The results of the platform developed in this thesis are also in accordance, with 'blind' having a higher success rate than targeted. Furthermore, one should also bear in mind that awake mice will always yield lower success rates than anaesthetised in the same way that *in vivo* will yield lower than *ex vivo*, due to higher complexity and movement. Nevertheless, common conditions to consider a whole-cell recording successful were: membrane potential below -40/-50 mV, input resistance below 200/300 MΩ (albeit dependent on cell type/size) and holding current below ±200 pA to maintain the cell at -65 mV, consistent with the literature (Kodandaramaiah et al., 2012; Holst et al., 2019).

As can be seen from Table 1, most *ex vivo* approaches are infrared-guided, while most *in vivo* approaches are 'blind' instead of two-photon targeted, with the exceptions of Annecchino et al. (2017) and Suk et al. (2017), and used anesthetized mice as their sample, with the exceptions of Desai et al. (2015) and Kodandaramaiah et al. (2018), which used both. Long et al. (2015) also uses two-photon targeted imaging, but since they automatized the pipette trajectory but not the actual patch-clamping process, their yield cannot be compared to the others, as it is manual (depicted in grey instead of black on the table). Suk et al. (2017) report that their 'imagepatcher' failed to operate in awake mice, but are hopeful that measures taken to reduce brain movement and improved real-time tracking algorithms could fix this issue.

Holst et al. (2019) mechanizes the pipette preparation steps by including a robotic arm that takes pipettes from a carousel, fills them with internal solution and places them on the electrode holder, a system first described in Go et al. (2013). It does, however, seem to have a lower than

Paper and year	In vitro / In vivo (anesthetized / awake)	Number of micromanipulators	Imaging system	Autonomous degree	Whole cell recording yield	Time (min)
(Kodandaramaiah et al., 2012).	In vivo, anesthetized	1	Blind	[5][6][7][8]	32.9%	5 ± 2
(Perin and Makram, 2013)	Ex vivo (brain slices)	12	IR	[5][7][8]	40-80%	-
(Long, Li, Knoblich, Zeng, & Peng, 2015)	In vivo, anesthetized	1	Two-photon targeted	[4][5][6]	66% in Cux2 mice and 22% in SST mice (Manual)	6.55 ± 0.53
(Desai, Siegel, Taylor, Chitwood, & Johnston, 2015)	In vivo, awake	1	Blind	[4][5][6][7][8]	17.9%	8 ± 1
(Wu, et al., 2016)	Ex vivo (brain slices)	1	IR	[4][5][6][7][8]	43.2% requiring no manual intervention (68.2% otherwise)	1.72 ± 0.05
(Annecchino et al., 2017)	In vivo, anesthetized	1	Two-photon targeted	[5][6][7][8]	22.2% in GAD67-GFP mice	6.1 ± 0.6
(Suk, et al., 2017)	In vivo, anesthetized	1	Two-photon targeted	[4][5][6][7][8]	22.2% for PV neurons, and 20% for CaMKIIa neurons	12 ± 3
(Kodandaramaiah et al., 2018)	In vivo, anesthetized and awake	4	Blind	[5][6][7][8]	30.7% for dual or triple recordings, 0% for quadruple in anesthetized mice.17.5% in awake mice (dual, triple)	10.5 ± 2.6 for one or more successful WCR
(Holst et al., 2019)	In vivo, anesthetized	1	Blind	[2][3][4][5] [6] [7][8]	9%	5.3
(Peng, et al., 2019)	Ex vivo (brain slices)	Up to 10	IR	[4][7][9]	7.9 ± 1.1 neurons with a success rate of 79% ± 11% (Manual)	46.1 ± 4.6 for 10
(Kolb et al., 2019)	Ex vivo (brain slices)	1	IR	[4][5][6][7][8] [9]	51% (cortical cells) and 43% for subcortical	~ 4
(Koos et al., 2021)	Ex vivo (brain slices)	1	IR	[4][5][6][7][8] [9]	63.6% in rat and 37.37% in human	-

Table 1. Summary of the relevant papers on patch-clamp automation for *ex vivo* and *in vivo* applications.

usual yield, which they attribute to the long time that the pre-pulled pipettes are exposed to ambient air in the carousel (making clogging more likely), tissue damage and blind-associated issues such as capillary encounter (Holst et al., 2019).

An alternative to the pipette carousel that still avoids manual work for pipette filling and exchange is the one used in Peng et al. (2019), which is based on a cleaning protocol first described by Kolb et al. (2016). An outer ring filled with Tergazyme is added to the sample chamber, so that once the pipette has been used, it can be self-cleaned and reused. Furthermore, in their work they incorporate a multi-pipette filling device, which, together with the self-cleaning function, can greatly decrease experiment time. Even though their work is still mainly manual, with only the pressure system and a semi-automatic pipette detection systems being computerized, the high yield achieved is praise-worthy. The same setup was used in Planert et al. (2021) to patch more than a thousand human neurons *ex vivo*.

Also worthy of mention is the work of Perin and Markram (2013), that partially automated up to 12 manipulators, the highest number of all. Even though the final approach is manual, their work is still admirable. However, their choice of command for the system (a game console with compound button combinations to initiate steps in the patch-clamp process) seems like an unusual and unnecessarily complicated choice. Interestingly, they present their yield as dependant on the experimenter's experience, giving it a binomial model (experienced vs. inexperienced users). While I wholeheartedly agree with this, I would further expand it to the idea that even within experienced researchers, the variability from day to day (mainly slice quality) is something that will also impact success rate, which is reflected by our daily 'blind' success rate variability (Results Chapter 5). Finally, in the *ex vivo* modality, we find the work of Kolb et al. (2019) and Koos et al. (2021), both offering completely automated, unsupervised infrared-guided patch-clamp with high success rates. Kolb et al. (2019) uses machine vision to reacquire the pipette position along the way to the cell, while Koos et al. (2021) uses deep learning to automatically choose 'healthy' targets, seemingly the first one to do so. All in all, they offer slightly higher success rates than the work by Wu et al. (2016), understandably, as this is an earlier work and actual predecessor of the system presented in Kolb et al. (2019). However, Wu et al. (2016) does offer the possibility of matching up two-photon fluorescent footprints to infrared-imaged cells, to target specific cells types. Bright-field infrared (IR) imaging or DIC are the traditional methods used in manual patch-clamp because they grant high level

of detail in thin samples (such as brain slices) and allow users to see cells dimpling, which is key in obtaining successful seals. On the contrary, dimpling is not seen in two-photon microscopy. Therefore, it would be expected of IR guided systems to achieve a higher success rate than a two-photon guided system. It should be noted, however, that two-photon-guided patching allows types of studies that unlabelled cells/IR-guided systems are incapable of (as explained in the previous sections). Moreover, being two-photon guided lends itself to be used in both *ex vivo* and *in vivo*.

It is also worthy of mention that the system by Kolb et al. (2019) was also used to patch cultured cells with a dual manipulator setup with high success.

Talking about *in vivo* autopatchers, it is remarkable the work done by Kodandaramaiah et al. (2018), where they achieved multi-patching with high success rates. They do point out, however, that yield could be improved by reducing the amount of tubing used in the pressure system. They also say that some cells were lost after sealing and before break-through while waiting for the other cells to be approached and sealed, a problem also present in manual patching.

Other differences in yield between systems are attributed to clogged pipettes due to both reduced pipette pressure (to avoid tissue damage) and entanglement/hitting blood vessels (Desai et al., 2015). In all platforms including pressure control, pipette resistance is checked at the beginning of the process, and the pipette is discarded if considered inadequate (below 3 or above 9 MΩ) or if it becomes clogged or broken (indicated by a drastic change in resistance).

It is clear that patch-clamping can greatly benefit from automation, as the human attention and skill required can be lowered at the same time that greater scalability and yield can be achieved by decreasing variability in pipette trajectory and pressure control (Annecchino et al., 2017; Suk et al., 2017). Furthermore, no current approach allows for autonomous, two-photon targeted multi-patching of cells, neither *in vivo* nor *ex vivo*, a gap that this projects aims to close.

On the whole, for single *in vivo* automated 'blind' patch-clamp, around 75% of attempts lead to a seal and around 50% attempts lead to a WCR within 3-4 minutes on average (Annecchino et al., 2017). Dual or triple concurrent automated 'blind' WCR have also been achieved (in a quad setup) around 29% of attempts in anesthetized animals and 18% of attempts in awake animals within around 10 minutes on average (Kodandaramaiah et al., 2018). Automated two-

photon targeting achieved seals in about half of the trials and between 20-30% of trials led to a WCR within a 6-minute average (Annecchino et al., 2017; Suk et al., 2017). Recordings were comparable in quality and stability in terms of resting membrane potential, input resistance, holding duration and spike magnitude, to manual *in vivo* studies (Margrie et al., 2002; DeWeese, 2007) and 'blind' robotic systems (Kodandaramaiah et al., 2012, 2018), across a range of recording depths. For more information on the state-of-the-art in autonomous patch-clamping, consult the reviews by Annecchino and Schultz (2018), Suk et al. (2019) and Alegria et al. (2020).

1.6 Overview

Patch-clamp is among the most effective tools for obtaining high-fidelity electrical recordings of individual neurons and has enabled the analysis of cell excitability, post and presynaptic responses, neuronal inter-connectivity and high order behavioural states, among many others. Despite providing high-quality data, the patch-clamp technique remains limited by the inherent low throughput and labour intensity. For an experienced experimenter, success rates for 'blind' single whole-cell *in vivo* recordings are reported to fall between 20 - 50% (Margrie et al., 2002). Robotic automation helps mitigating such issues and offers several benefits including faster skill assimilation for operators new to the technique, standardised recording quality, and improved throughput. Reliably scaling up the technique to simultaneous patch-clamp recording from multiple cells enables assays of synaptic coupling and many new research lines in basic and translational neuroscience. Significant strides have been made towards the automation of both 'blind' and two-photon guided approaches as evidenced by the numerous systems presented. Automated 'blind' systems can achieve success rates comparable to human experimenters with improved throughput, and have expanded to patch up to three cells simultaneously. Targeted multi-patching had not been realised until now, due to the difficulties associated with controlling multiple pipettes simultaneously and constraints of two-photon imaging. The work presented in this thesis represents the first ever two-photon targeted, quad patch-clamp system, which will open up endless possibilities in new neuroscience studies.

Chapter 2

Methods

2.1 Protocols

This chapter covers the methods used to prepare everything needed in an experimental day: from the protocols used to produce the electrophysiology solutions, to the fluorescent samples, to the procedure to follow in RITA (the software) to start the experiment. The following chapters cover the hardware and software, respectively.

2.1.1 Internal solution for brain slices

The solution inside the patch-clamp pipette should resemble the contents of the intracellular milieu as much as possible, containing all the ions and energy molecules necessary for normal cell behaviour. The process of making said solution takes a few hours but luckily it only needs to be done once every few months.

1. For 5 mM, 115 mM and 10 mM concentrations of KCl (Potassium Chloride), K-Gluconate (Potassium Gluconate) and HEPES (4-(2-hydroxyethyl)-1-piperazineethanesulfonic acid) respectively, weigh 18.64 and 1346.94 mg of the first two, then add 0.5 mL from 1 M stock of the third. Dissolve into 45 ml of purified water.

2. Adjust pH to 7.2 by slowly adding drops of a 0.5 M KOH (Potassium hydroxide) stock solution. Stir solution while drops are added and pH is measured, for accuracy. Usually,

$\sim$ 500 μL are needed.

3. For 4 mM, 0.3 mM, 10 mM and 0.1 w/v concentrations of Mg-ATP (Adenosine 5'-triphosphate magnesium salt hydrate), Na-GTP (Guanosine 5-triphosphate sodium salt hydrate), Na-Phosphocreatine (Phosphocreatine disodium salt hydrate) and biocytin respectively, weigh 101.44, 7.85, 127.55 and 50.00 mg respectively and dissolve in the solution. Use around 4 mL of purified water to wash off remaining substance from the weighing boat and add to solution.

4. Sonicate for 35 min.

5. Slowly add drops of a 1 M stock solution of KOH until pH falls within 7.2-7.4. Stir and measure throughout. Usually, $\sim$ 350 μL are needed.

6. Adjust osmolarity with sucrose until osmolarity is 310 mOsm. Stir throughout. It is usually around 240 mOsm before any sucrose is added and $\sim$ 0.8 g are needed.

This protocol is used in Jesper Sjöström's lab at McGill University, where I learned to quad patch. I used it without the addition of Biocytin, as this is a molecule traditionally used for post-experimental image reconstruction purposes, which was not necessary in my case. I added my comments on how much is needed during pH and osmolarity adjustments. A variability of up to $\pm$ 3 mOsm is acceptable, but anything below 307 or above 313 mOsm should be avoided, to maximize sealing probabilities. Aliquots of 1 mL can be frozen in Eppendorf tubes to use on the day of the experiment. If pipette cleaning for pipette reuse is available, considerably less internal will be used, as a single pipette with internal can be used for up to 30 trials, as long as the level of internal within the pipette is high enough to reach the electrode, as opposed to needing a pipette filled with new internal solution for every trial. Nevertheless, it is recommended to have the above amount anyway to aid in the filtering process, as most filters require a minimum volume. Another option is smaller aliquots and using centrifuge tube filters.

On experiment day, thaw an internal solution aliquot and, if targeted, add Alexa 594 Hydrazyde 10 mM (0.1 μL to 1mL of internal solution) to visualize pipette tips and patched cells under 2P microscopy. Filter the solution with a 0.2 μm filter to avoid clogging the pipette tips (Sartorius Minisart from Fisher Scientific).

2.1.2 Artificial Cerebrospinal Fluid (aCSF) solutions for *ex vivo* slices

There are three aCSF (artificial cerebrospinal fluid) solutions required for an experiment day of FURA 2-AM bath-loaded brain slices: slicing, resting and imaging aCSF. The concentrations of the different chemicals needed for each of the them can be observed in Table 2.1. Both the slicing and resting solutions are used when dye loading is taking place, during the slicing and loading process respectively, while the imaging aCSF can be used for perfusion during the experiment. If dye loading is not necessary (the brain is already fluorescent or it is a 'blind' experiment), the imaging aCSF can be used for the slicing part of the protocol as well.

	sACSF	rACSF	iACSF
$CaCl_2$	0.5 mM	2 mM	2 mM
KCl	3 mM	3 mM	2.5 mM
$NaHCO_3$	26 mM	26 mM	26 mM
NaH_2PO_4	1 mM	1 mM	1.25 mM
$MgCl_2$	3.5 mM	6 mM	1 mM
Sucrose	123 mM	-	-
Dextrose	25 mM	25 mM	25 mM
NaCl	-	123 mM	125 mM

Table 2.1: Concentrations for slicing, resting and imaging aCSF (artificial cerebrospinal fluid) solutions. $CaCl_2$: Calcium chloride, KCl: Potassium Chloride, $NaHCO_3$: Sodium bicarbonate, NaH_2PO_4: Sodium phosphate monobasic monohydrate, $MgCl_2$: Magnesium Chloride, NaCl: Sodium Chloride

Concentrates for the different aCSFs can be prepared in advance (less than a month) to ease the load on the experiment day. For the imaging concentrate solution (10x), weigh 73.05, 1.86, 1.72 and 21.87 g of NaCl, KCl, NaH_2PO_4 and $NaHCO_3$ respectively, and dissolve in 1 L of purified water. On experiment day, dilute the 10X concentrate with purified water (1 part concentrate, 9 parts diluted water), add the $CaCl_2$ and $MgCl_2$, and glucose until 338 mOsm is reached.

A concentrate (10X) common to both the slicing and resting solutions can be prepared beforehand by diluting 2.232, 21.87 and 1.376 g of KCl, $NaHCO_3$ and NaH_2PO_4 respectively in 1L of purified water. On experiment day, dilute the 10X concentrate with purified water (1 part concentrate, 9 parts diluted water) and add the missing components. Adjust osmolarity to 338 mOsm.

2.1.3 Slicing protocol for *ex vivo* fluorescent slices

This protocol is for mice at postnatal ages 11 to 20 days (p11-p20). Slices stay healthy for +5 hours at this age. After p20, other solutions should be used, as brains are more susceptible to slicing conditions. Sucrose-rich aCSF or NMDG solutions should be used instead (Ting et al., 2014). After p20 using a microfluidic device that improves oxygenation by flowing carbogen underneath the slices can improve bulk loading up to 10 times (and bulk loading of old mice becomes possible) (Mauleon et al., 2013). However, since quad patching is often done in younger animals to increase the likelihood of abundant healthy cells, this method was not tested.

At the start of the day, make 1x concentration of iACSF by diluting the 10X iACSF concentrate with purified water and adding 1 mL/L of $MgCl_2$ (1M stock) and 2 mL/L of $CaCl_2$ (1M stock). Then add D-Glucose/Dextrose, first 8.9 g/L, then small increments of 0.1-0.2 g until reaching 338mOsm or matching target, depending on the osmolarity of the internal. Although the internal solution is supposed to be 310 mOsm, there is variability and it should be measured on the day, then match the difference from 310 in the aCSF: if the internal is 308 mOsm, then the aCSF should be 336 mOsm; if the internal is 313 mOsm, then the aCSF should be 341 mOsm. Basically, for optimal sealing, a difference of 30 mOsm between the two solutions is desired. Bubbling throughout the slicing process and experiment is necessary to avoid Ca+ precipitation. 2 L of aCSF are recommended to have enough for slicing and perfusion during the experiment.

Prepare the area for slicing:

1. Use paper towels to cover the table surface and absorb any blood.
2. Turn on slicer (7000smz-2 Vibrotome from Campden Instruments) and perform the calibration following the instructions on the screen until blade misalignment is as low as possible (~ 0.2 μm), for even brain slicing.
3. Fill a large box with ice and put a beaker, with approximately 250 mL of aCSF, inside the box, so that it is completely surrounded by ice. Add a thermometer to the solution, and monitor the temperature until it reaches 4 ℃. This temperature is recommended to reduce the swelling and inflammation in the brain during its extraction, cutting and slicing. This yields healthier slices for patching.

4. Turn on the bath heater, fill a beaker with aCSF until the brain holder inside (Figure 2.1, number 7) is completely covered in liquid, and place the beaker in the heater. Fill the surrounding space with water until it reaches the brim. A thermometer should be used to measure the temperature of this solution, which should become stable at ~ 37 ℃. This temperature is ideal to return the cells to their natural baseline temperature once the slicing is done.

5. Bubble the aCSF in both beakers with carbogen (5% CO_2, 95% O_2). This provides oxygen to maintain the health of the neurons.

6. Lay the instruments on the surface in order of use. Prepare a cadaver bag as well.

7. Turn on the isofluorane extractor and make sure the valve on the back of the chamber is open if using a system like the one in Figure 2.1. Otherwise prepare the isofluorane bottle and four cotton buds. Alternatively, if schedule I is to be performed, neither of these components is necessary.

8. Place a piece of round filter paper in a Petri dish. This will be used to manually cut the brain and the filter paper prevents the blade from slipping while cutting. Place small pieces of filter paper on the side to dry the brain before gluing it.

Brain extraction should be done as fast as possible for optimal brain slices. Slicing and brain extraction protocol:

1. Start by anesthetizing the mouse with isofluorane until no twitch reflex is found (pinch one of the posterior legs to check). Alternatively, perform schedule I (neck dislocation).

2. Decapitate with large scissors, then cut the skin with smaller scissors along the longitudinal fissure and retract it to the sides. With clean scissors, two side cuts are done on the horizontal plane at the base of the skull and then the skull is cut along the longitudinal fissure. Tweezers are used to fold the skull to the sides, exposing the brain. The brain is then scooped out gently with the help of a spatula. The skull is very malleable at this stage so the danger of cutting the brain while removing it is greatly decreased, but one should still be careful. After extraction the whole brain is submerged in the 4 ℃ aCSF solution.



Figure 2.1: Slicing area. (1) Isofluorane chamber to anesthetize the mouse. (2) Instruments for the extraction of the brain. (3) Filter paper used to glue the brain to the platform that later goes onto the slicing chamber in (6). (4) Notes for record keeping. (5) Ice-cold aCSF. (6) Vibratome to slice the brain. (7) Heater bath for the resting period of the brain slices.

3. Put the cadaver in the bag and seal it. Change gloves.

4. Extract brain from beaker and place on Petri dish. Cover the brain with 4 ℃ aCSF by pouring it from the beaker.

5. With the use of a scalpel or blade, the cerebellum is removed with a coronal cut and the hemispheres are separated along the longitudinal fissure. A slanted cut (45º from the table surface) from the posterior towards the anterior part of the hemispheres is done while the brain hemispheres are lying on the longitudinal cut (the one used to separate the hemispheres). The hemispheres should be forming a 30º angle between them before this cut. The 45º degree cut is done such that the experimenter starts at 1/3 of the dorsal surface of the brain to end on the rostral surface. This slicing is done to preserve the connections between neurons inside layer V of the primary visual cortex, which has mainly been our target region.

6. The slanted cut performed is then used to glue both brain hemispheres to the metallic platform that goes into the slicing chamber.

7. Cover the slicing chamber with cold aCSF and place a diffusor there for bubbling.

8. Use slicer to cut 250 μm brain slices. After slicing, the slices are put into a bath at 37 ℃ in ACSF for 10-30 min (longer in slices) from younger animals. Then the slices are taken to a bath that is at room temperature, where they remain until use.

2.1.4 Slicing protocol for *ex vivo* non-fluorescent slices: bath loading of FURA 2-AM

Calcium indicators such as Oregon Green Bapta-1, Indo-1, Fluo-4 or Calcein are molecules that become fluorescent upon binding of a calcium molecule. Hence, they can be a direct indicator of the amount of calcium in the cell, and indirectly, the electrical activity of the cell (Simons, 1988). Calcium indicators are usually employed to monitor the electric activity of big populations of neurons at the same time (MacLean and Yuste, 2009). When they are not genetically encoded (GECIs) (Nakai et al., 2001), they are usually bulk loaded. Due to their negatively charged nature, they cannot enter the cell in the natural state. Acetoxymethyl (AM) ester derivatives were developed to bypass this problem (Tsien, 1981), as the ester groups block

charges, making the indicators lipophilic and thus allowing them to enter the cell. Once inside, esterases cleave the AM groups, effectively trapping the indicator inside the cell, which is now free to bind a calcium molecule. This process is highly cell dependent, and one of its main limitations is that it cannot provide information about specific action potentials within activity bursts, only about the onset (MacLean and Yuste, 2009).

This protocol in particular was performed with FURA 2-AM and C57BL/6J mice to produce fluorescently labelled neurons to test the automated quad-patching system. It works best in animals between p11 and p16, as age is crucial for proper bath loading. After this age the extracellular matrix becomes less permeable, giving higher background signal and thus lower signal-to-noise ratio for the cells. This protocol is based on Jason McLean's protocol described in Sadovsky and MacLean (2014).

Calcein and Oregon Green Bapta-1 bath loading and injection loading were also tested, but FURA 2-AM gave the best time stability in terms of baseline fluorescence. This is partly due to the fact that, as opposed to many others, it is a negative calcium dye (MacLean and Yuste, 2009), meaning that calcium spikes lead to a decrease in fluorescence. This means that, contrary to positive dyes, it will have a higher baseline fluorescence, which is ideal for our program. Still, this method has its limitations: as the dye can only penetrate the most outer layer, the brightest signal will always come from more superficial cells, which in turn are the worst ones to patch. In general, cells deeper than 100 μm are preferred for patch-clamp, as they are less affected by the slicing process and the chances of their axons being severed are also lower. On top of that, the signal-to-noise ratio of any of the bath loaded calcium dyes will never be comparable to virus-injected fluorescence or genetically encoded fluorescence. In that sense, it is recommended to use these kinds of samples with RITA (our software), as the yield will be higher, but it nevertheless works with loaded FURA 2-AM.

Before the start of the experiment, slicing Artificial Cerebro Spinal Fluid (sACSF) and resting ACSF (rACSF) should be prepared. 0.5 L of each should suffice for an experiment day. Take 50 mL of the concentrate and 450 mL of purified water for each of the two solutions and then add 21.05 g, 4.5 g, 0.25 mL and 1.75 mL of Sucrose, D-Glucose/Dextrose, $CaCl_2$, and $MgCl_2$ respectively for the sACSF and 4.5 g, 3.594 g, 1 mL and 3 mL of D-Glucose, NaCl, $CaCl_2$ and $MgCl_2$ respectively for the rACSF. 1 L of iASCF is recommended for perfusion, see preparation in subsection 2.1.3.

Place 3 mL of raCSF in a small circular chamber. The chamber should be placed inside the incubator/bath heater, and, to improve heat convection, water should be added to the surroundings of the chamber. Add oxygen bubbling to the chamber. The bubbling should not be too high because the DMSO (Dimethyl sulfoxide) in the dye solution creates bubbles, but it should not be too low either as this can be detrimental to the brain slices.

Place the rest of the rACSF in a beaker with a brain holder and bubble with a diffuser.

Add 2 μL of Pluronic F-127 (20% Solution in DMSO) and 13 μL of DMSO to the vial containing 50 μg of FURA 2-AM. Vortex this solution for at least 5 minutes and then leave it resting for at least half an hour (the longer, the better). Some protocols suggest sonication instead of vortexing. However, pluronic may have toxic effects on cells when sonicated, due to polymer degradation (Wang et al., 2012), so vortexing is recommended.

Slice normally, following the protocol in section 2.1.3, using the vibratome at a cutting speed of 0.06 mm/s and with a slice thickness of 400 μm. Place the slices in the small circular chamber for incubation.

After 10-30 min, add the 15 μL of FURA 2-AM solution to the chamber using a pipette. Add directly on top of the brain slices so that the initial concentration is higher. Let it incubate for 45 min at 35 ^{o}C. After this, move the slices onto the oxygenated rACSF and let them rest for 15 min at room temperature.

Use 790 nm on the 2P microscope for optimal visualization.

While RITA works well with FURA 2-AM loaded slices, they are technically challenging to work with, as the dyeing is quite superficial, which, in combination with the uneven slice topography, leads to adjacent cells to be often seen in different planes, which complicates RITA functioning. Furthermore, as mice get older, changes in the extracellular matrix lead to reduced dye penetration, which in turn yield progressively worse fluorescent footprints for the cells. RITA relies on these footprints to find the coordinates of the cells, and on older mice, RITA would often have difficulties finding the coordinates, forcing us to choose different targets and losing time. Therefore, genetically encoded methods were investigated, with the hopes of also getting better cell-to-background signal ratio.

2.1.5 Virus injections and other methods for the generation of fluorescent samples

Expression in individual cell types is essential in understanding the activity and roles of certain populations within the brain circuitry. Different methods can be used to achieve this: transgenic animals, gene delivery by viral vectors, *In Utero Electroporation*, Cre/LoxP technologies, etc (Haery et al., 2019).

In the viral vector category, different strategies have been used in the brain: direct intracerebral injections, intravenous methods (tail vein injection, retro-orbital injection, temporal/face vein injection and intraperitoneal) and administration routes into the cerebrospinal fluid (the cisterna magna, subpial, intracerebroventricular, or the intrathecal space along the spinal cord) (Haery et al., 2019). Direct administration into the brain is the most common, as it requires the least amount of virus and it achieves high expression in the targeted area without other areas being affected. It is also, however, very demanding technically, has the most risks in terms of invasiveness, can damage the target area and leaves an expression gradient. The other two techniques require higher amounts of virus but can achieve wide central nervous system expression. Particularly, intravenous (IV) methods seem the most advantageous as they require no surgical expertise and they are quick and non-invasive (Haery et al., 2019). Tail injections have been described as distressful for the animals and technically challenging (Yardeni et al., 2011). Retro-orbital injections have been described as aesthetically displeasing, but have been successfully employed in the delivery of gene therapy, experimental compounds, bone marrow transplantation (Yardeni et al., 2011), and GCaMP6s widespread expression in the cortex (Hillier et al., 2017). Temporal/face vein injection has often been dismissed due to its small delivery window: it is almost impossible to visualize the vein in neonates older than three days. This, however, is the perfect injection window for this project, as pups are used from p11 to p20 (for their resilience to the slicing process), and expression typically takes a minimum of a week.

Facial vein injections have been proven to work for brain gene delivery (Rahim et al., 2011) and specifically for widespread GFP expression in the brain (Foust et al., 2009), thanks to the leakiness of the developing blood-brain barrier. There are several papers that describe the technique, from its complex beginnings (Sands and Barker, 1999) to video journals that make

it very easy for someone with no experience to perform them successfully (Lampe et al., 2014).

When thinking about the desired level of expression and target cells, while the delivery method is important, the serotype of the viral vector is also crucial. Adeno Associated Virus (AAVs) are famous for their lack of pathogenicity and immune response while achieving robust transgene expression (Pattali et al., 2019). Particularly, Adeno Associated Virus 9 (AAV9) has been proven to achieve widespread neuronal transduction in most animals across their lifespan (Pattali et al., 2019), and specifically Foust et al. (2009) achieved widespread eGFP expression in neurons. Thus, pENN.AAV.CamKII0.4.eGFP.WPRE.rBG (AAV9) was chosen to achieve sparse yet intense labelling of cortical neurons, through facial vein injection following Lampe et al. (2014). pENN.AAV.CamKII0.4.eGFP.WPRE.rBG was purchased from AddGene and it was a gift from James M. Wilson (Addgene viral prep 105541-AAV9 ; http://n2t.net/addgene:105541 ; RRID:Addgene_105541). CamKII (Ca^{2+} / calmodulin-dependent protein kinase II) is a common promoter to target expression of the plasmid in excitatory neurons in the forebrain (Wang et al., 2013). The expression of said virus delivery method can be seen in Figure 2.2, while a 2PM image comparing this method to the FURA 2-AM expression can be seen in Figure 2.3.

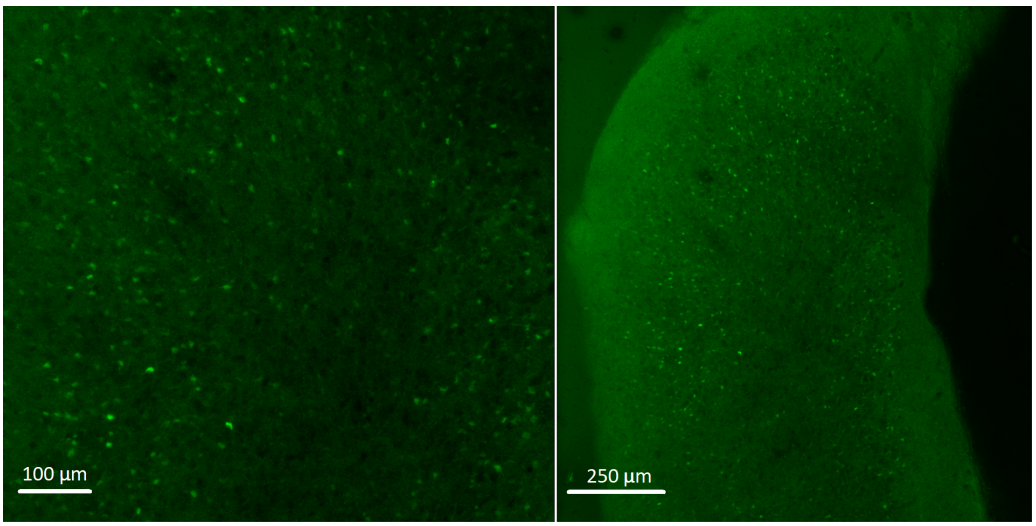


Figure 2.2: PFA-fixed brain cortex sections of a juvenile mouse (between p11-p19), showing fluorescence under a confocal microscope as a result of p0 viral injection of CamKII-GFP (AAV9) virus, on two different magnifications.

For the injection procedure, the dam will remain in a warm chamber while pups are retrieved one by one from cage. Before handling any pup, it is recommended to thoroughly rub the gloves with the dirty bedding, to avoid dam rejection of the pups. Pups must be anesthetized by hypothermia. Pup must be restrained by holding the face between the index and thumb

fingers, and the hind legs with the remaining fingers, with care to avoid breaking the skin. Then, 1 x 10^{11} vector genomes (10 μL) were injected using a bevelled Hamilton syringe into the temporal vein. The facial vein runs dorsal to ventral, is just anterior to the ear and does not move with the skin. The injection of a pup lasts for 1-2 minutes. Once the pup is back to physiological temperature, it is returned to the cage. After the procedure, one should make sure that the mum is interacting with the pups (ideally cleaning and moving them), as this is a good sign of acceptance. To avoid rejection, other strategies are to use ethanol to erase any foreign smells in the pups and/or dam's nose and separating the mum to prevent it from hearing the pups (Lampe et al., 2014).

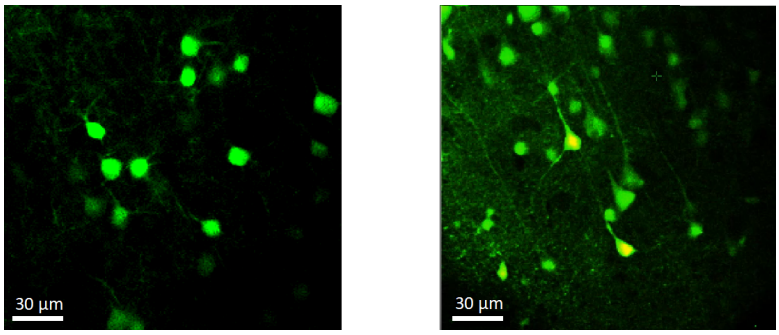


Figure 2.3: CamKII-GFP (AAV9) virus expression vs. FURA 2-AM bath loading expression. (Left) Pyramidal cells showing fluorescence as a result of p0 viral injection of CamKII-GFP (AAV9) virus. Background fluorescence is low. (Right) FURA 2-AM bath loading signal of pyramidal cells in the visual cortex. Background fluorescence is higher and most importantly, fluorescence is uneven due to slice topology. Both images were taken with a 40X immersion objective.

A transgenic mouse line like 'Thy-1 GFP line M' which already expresses a fluorescent protein like GFP (in pyramidal cells of layer V of the cortex, our usual targets) would have been an excellent testing ground for RITA (Feng et al., 2000). These animals are genetically altered and can be bought from providers like The Jackson Laboratory (or created, if such expertise is available) and bred for experiments. While transgenic mice would have been a less time demanding solution to test RITA, as they do not require injections, breeding also takes time to establish a stable colony and more importantly, are expensive to both purchase and maintain. Different issues over time prevented us from breeding a transgenic line, from COVID, to lack of funding, to lack of PPL, to lack of time left in the project. I also contacted many different labs in Imperial to try to get some transgenic mice that we could use, to no avail. In the end, the injections proved to be a good solution, as they seem to give similar expression patterns

to transgenic mice, even if they require constant availability of the experimenter to inject the mice upon birth.

Another method for genetic delivery is *In Utero Electroporation* (IUE). In this method, surgery is performed in pregnant mice to extract the pups, then the desired plasmid is injected into one of their ventricles and then electroporation is used to insert the plasmid into the cells, by means of (negatively charged) DNA migration towards the positive pole electrode. This method is complicated to learn and carries certain risk for the animals, but can be less expensive than virus injection and offers robust expression throughout the whole electroporated area. Not only that, but subgroups of cells can be targeted. For example, if timed correctly, the targeting of the Medial Glangionic Evidence (MGE), where interneurons are present at the initial stages of development before initiating migration to their final destination, will yield expression of the plasmid in most interneurons. Promoters for inhibitory cells like mDlx or FishELL can also be used to assure expression only in the desired cells (Petros et al., 2015). I tried to use this method to produce transgenic mice for our project, but unfortunately, the two people trained in this method unexpectedly left our laboratory before they could train me or anyone else.

2.2 Rig preparation for the start of the experiment

1. Start perfusion in the rig by opening the pressure valve under the rig for suction (there will be a distinctive noise made by the vacuum ejector) and opening the gravity inlet into the sample chamber. If it does not flow, help by applying suction with a syringe. aCSF should be bubbled with carbogen and diffused through the sample throughout the whole experiment. After the experiment, the perfusion system should be rinsed first with ethanol and then with purified water, to avoid clogs.

2. Turn on the inline heater and set the desired temperature.

3. Turn on the four manipulators' control racks, stage rack, galvo scanners control rack, the two amplifiers, shutter controller, PMT modulator, Pockels cell control board and infrared (IR) lamp. Shutter should be in X Gate and Enable mode to allow the computer to control it. Plug in the pressure system.

4. To turn the Ti:Sapphire laser on, turn the key to ON position and then use the Mai Tai

software to turn it on. Check that temperature is not over 24 ^{o}C (check LED display on the cooling system), check level of coolant is high enough and check that the laser is pulsing and no errors are being displayed. Set the desired wavelength. Do not open shutter until you are about to image.

5. Start Multiclamp 700B Commander software.

6. Pull pipettes from glass capillaries. I used filamented ones that come fire-polished (Standard filamented glass capillaries (1B150F-4) from WPI). They were pulled using a horizontal puller (P-1000 from Precision Instruments). Optimal pipette resistance is 4-6 MΩ, but we have seen that with our system 5.5-7 MΩ works best. Pull the pipettes shortly before each patching attempt to avoid clogging. Store them in a closed box for the same reasons.

7. Fill the pipettes with filtered internal solution and place them on the electrode holders. The liquid should reach the electrode to have electrical continuity. The bath electrode should be completely submerged as well for the correct measurement of the electrophysiology signals.

8. Place the brain in the sample chamber (coronal cut configuration) and place a harp on top to avoid movements. The placement of the harp should be such that the strings are vertical, to avoid axon disturbance. Find the desired region in the brain slice under the 4x objective using the IR light. Switch to the 40x and assess the healthiness of the cells.

9. If a targeted experiment is to be performed, turn off room lights and switch off IR. Switch optical path in the microscope to the laser and the PMTs and close rig curtain. Switch the PMT modulator from Safe to Enable.

2.3 Software protocol for a typical experiment

Do not press Run (the arrow) in LabView until Multiclamp Commander is open and the input/output hardware configuration in RITA (our software) is correct. The correct COM ports and channels for each piece of hardware can be checked in NI MAX (NI Measurement Automation Explorer, software by National Instruments), and they stay constant unless something is

plugged or unplugged. The first time RITA is run, calibration for all four manipulators should be performed and values stored, and this should be repeated every time there is a change in their configuration.

1. Press run and start the positive pressure on all working channels. +10 kPa is recommended for lowering the pipettes to the brain surface, and +5 KPa for the actual approach.

2. If in targeted mode, choose cells to be patched. If in 'blind' mode, choose a general area where cells look healthy. Lift the microscope objective as far up as possible while still having a meniscus.

3. Place the pipettes under the microscope and lower them until they are close to the brain surface, either manually or automatically.

4. If in targeted mode, switch back to 2P imaging and acquire both the pipette tips and targets by clicking on them and pressing the corresponding 'Acquire tip/target' button. While targets are in focus, set tracking of cells to ON. Press center targets.

5. Start the test pulse on all working electrophysiology channels and offset the signals (can be done automatically with the press of a button).

6. Press New experiment in the experiment notes section, fill in the relevant information and then press record.

7. If in 'blind' mode, press the Hunt button for all active channels. If in targeted mode, press the Final approach button: RITA will start the patch-clamping process and inform the user when a cell has been detected or sealed.

Chapter 3

Hardware Setup

This short chapter covers the hardware of the platform, which can be observed in Figure 3.1. A close up of the surroundings of the sample chamber can be seen in Figurre 3.4. The software is covered in the next chapter (4).

The platform comprises a Ti:Sapphire laser (Newport/Spectraphysics), a multi-photon microscope (Scientifica Ltd), and a 3DOF (degrees of freedom) micromanipulator per channel (Sensapex or Scientifica) fitted with mechanical stability rods to improve resistance against environmental factors such as floor vibrations, temperature fluctuations and pressure changes associated with patch-clamp, custom-developed electronically-controlled pressure regulator systems, electrophysiology amplifiers, and data acquisition boards.

Despite the fact that a very similar setup was used in the project by Luca Annecchino, I had to set up this rig from scratch from the individual components, because during the first months of my PhD, my laboratory was in the process of moving to a bigger space, and the previous rig had been dismantled before I joined the group. This included setting up, connecting and organizing the distribution of the following components, as well as their subsequent maintenance (was done by me):

1. Faraday cage for the electrical isolation of the electrophysiology equipment with a black curtain in the front. This protects the user from the laser as well as optically isolating the sample while two-photon imaging takes place. This is necessary because the PMTs (PhotoMultiplier Tubes) are very sensitive to light so any external light can trigger an

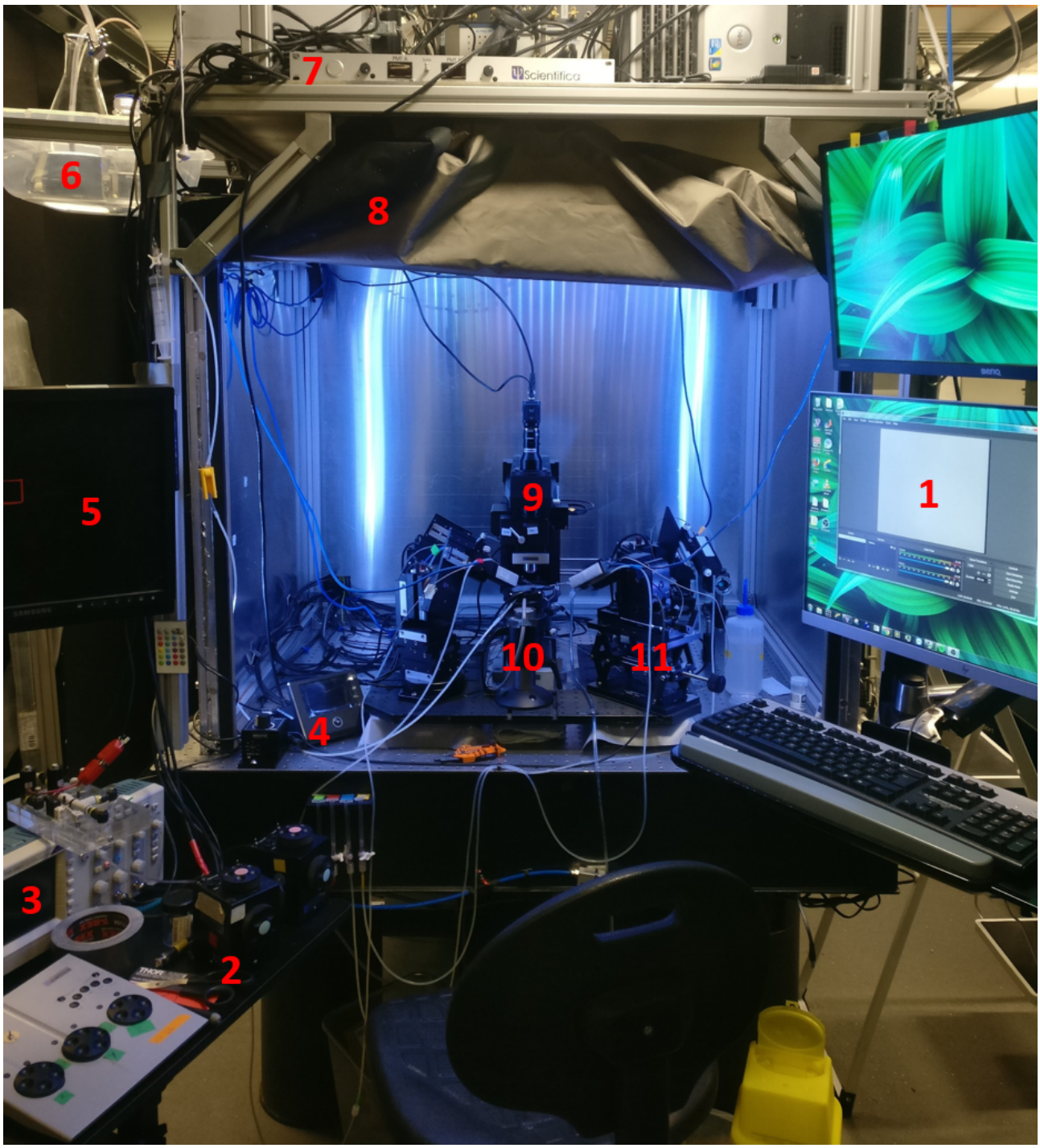


Figure 3.1: The rig setup. (1) Computer screens for the RITA software. (2) Control cubes for the Scientifica manipulators and control board for the stage. (3) Oscilloscope. (4) Sensapex control screen. (5) Screen for the IR signal. (6) Gravity perfusion system. (7) PMT controller. On this same shelf lie the DAQs, the two amplifiers, the laser shutter, the Pockels cell controller, and the control boards for the heater, Scientifica manipulators, stage and galvanometric mirrors. (8) Blackout curtain. (9) The microscope with both an IR system and two-photon imaging. (10) The sample chamber holder, which also holds the heater system. (11) Manipulators directed towards the sample chamber. The white tubes that can be observed going downwards and to the left are the connections from the electrode holder (of each manipulator) to their respective pressure system.

overload.

2. Scientifica XY moving stage with a control cube for the positioning of the sample under the FOV (Field of View) of the microscope, and a control board to communicate to the computer.

3. Scientifica PatchStar motorized micromanipulators with 3DOF (degrees of freedom) and control cube, for the micropipette insertion into the sample, with their corresponding control boards to communicate to the computer. The final placing of the four manipulators (Fig. 3.2) involved a trial and error dynamic to establish the optimal angles and positions that allow the four pipettes to be exchanged and to access the sample without physically colliding with one another or any part of the setup, including reaching the cleaning wells without collisions. They were all fitted with mechanical clamps. These clamps dampen the vibrations at the tip of the pipette that are caused by the characteristic changes in pressure during the patch-clamping process. I designed these clamps with SOLIDWORKS (Fig. 3.3), inspired by a similar design used in Jesper Sjöström's laboratory (Lalanne et al., 2016). I also designed and 3D printed the sample chamber with the detergent wells, loosely based on Kolb et al. (2016).

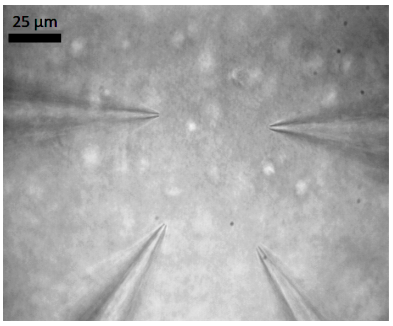


Figure 3.2: Final configuration of the four manipulators, as seen under infrared imaging. Geometrical symmetry was aimed for when possible, with the hope that the deformations that each of the pipettes introduce into the tissue would be counteracted (at least partially) by each other.

4. Sensapex micromanipulator with 4DOF. This system theoretically offers a higher spatial resolution with zero drift and it is also more compact, saving space (Sensapex, 2021). In fact, these micromanipulators were used in (Peng et al., 2019) to achieve a 10-micromanipulator setup versus the 8-micromanipulator setup achieved with the Scientifica micromanipulators. However, in our experience with the autopatcher, the Sensapex

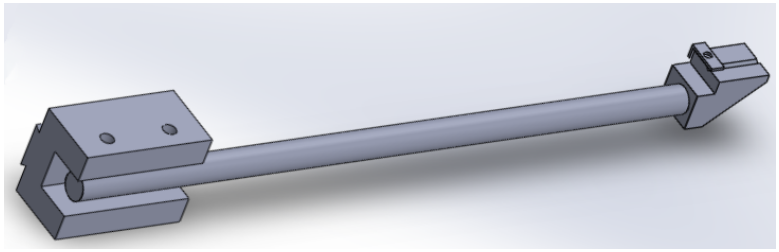


Figure 3.3: CAD drawing of the mechanical clamps. The printed version can be seen in Fig. 3.4. The electrode holder rests on the step of the piece on the right, with the capillary being clamped. The left piece allows for the rod to be held in place in the characteristic dove-tail railings of the manipulators. All three holes have screws that help clamp everything into place.

manipulator failed to display any differences in accuracy and thus translated to a yield comparable to the other three, (rather-old) Scientifica manipulators. On top of this, it is worth mentioning that: (1) Even when using a lighter, copper version of the ultra-stable rods, the weight was too much for the manipulator and it failed to work properly, so no ultra-stable rod could be used in this channel. This points to the fact that Sensapex manipulators are unable to carry anything heavier than an electrode holder; which may be an issue depending on the application. (2) The reduced height of the manipulator as compared to the Scientifica manipulators means that mismatching is not practical. The Sensapex is perfectly suited for microscopes that have an elevated XY stage, such that both manipulators and sample lie at the same height, whereas Scientifica manipulators need to lie on a XY stage that is significantly lower than the sample (Fig. 3.1). I solved this small issue by placing the Sensapex manipulator on a Pockels cell stand. Despite these disadvantages, the Sensapex has a much bigger range of motion than the Scientifica manipulators, which is a great aid when fitting four manipulators in a reduced space.

5. Amplifiers, NI DAQ board and I/O (input/output) boards for the successful transfer of small electrophysiology signals to the computer. All of this equipment, the computer and control boards were placed on a shelf on top of the rig to avoid noise on the electrophysiology signals and to create a clutter-free space.

6. Upright microscope with both bright-field microscopy (infrared LED light source, condenser and camera), for the visualization of *ex vivo* samples and two-photon microscopy: high precision galvanometer scan mirrors with two photomultiplier tubes (PMTs, with green and red filter) that allow pixel-like imaging scanning, with their corresponding NI

I/O board to communicate to the computer. ScanImage and Sciscan can both be used to control the imaging hardware but we integrated the essential parts of Sciscan into our software so that the user can control everything within RITA. For the IR imaging, some of the components were updated to improve image quality and imaging depth, and oblique imaging was implemented by adding a cut-out to the light source (which creates shadows that increase contrast in the sample).

7. Half-wave plate (to split the laser path between this rig and another), placement of mirrors (to direct the laser towards the microscope), finding the adequate filters for the desired fluorescence emission (red and green), Pockels cell (voltage-controlled wave-plate that allows the control of the laser intensity), shutter and other optical tools were set up and the Ti:Sapphire laser alignment was completed to enable imaging, including galvo alignment (to align the laser beam within the microscope towards the sample).

8. Both monitors, the keyboard and the mouse were set up in swivel arms that hang from the top shelf, so that they are accessible during experiments but will not create noise or movement that might interfere with the patch-clamping activities.

9. Grounding system to have noise-free signals. The simplest grounding system possible connects the electrodes in each of the channels to the grounding pellet. However, we wanted to be able to use RITA with any number of channels, so that if one channel is not being used, it would not be connected to the pellet (as this would create noise). Therefore, switches were added to each of the connections, so that they can be disconnected from the grounding system if needed. The grounding system has to be manually soldered, as no commercial setups are available as far as we are aware.

10. A gravity perfusion system with temperature probe and thermal sleeve to allow perfusion of the samples with fresh artificial cerebrospinal fluid (aCSF) at 33 ℃ was added. The aCSF is bubbled in a reservoir that sits at a certain height above the setup. When tubing is introduced inside the reservoir, the liquid will flow towards the sample chamber by gravity pull. This system usually includes a three-way valve with a syringe so that some suction can be applied to the tubing if the liquid is not free flowing (usually required if the tubes are dry and thus there is some resistance to the liquid flow). After some time using this system, we observed that the system created oscillations in the electrophysiology signals. These oscillations interfered with the impedance detection of the ‘blind’ mode,

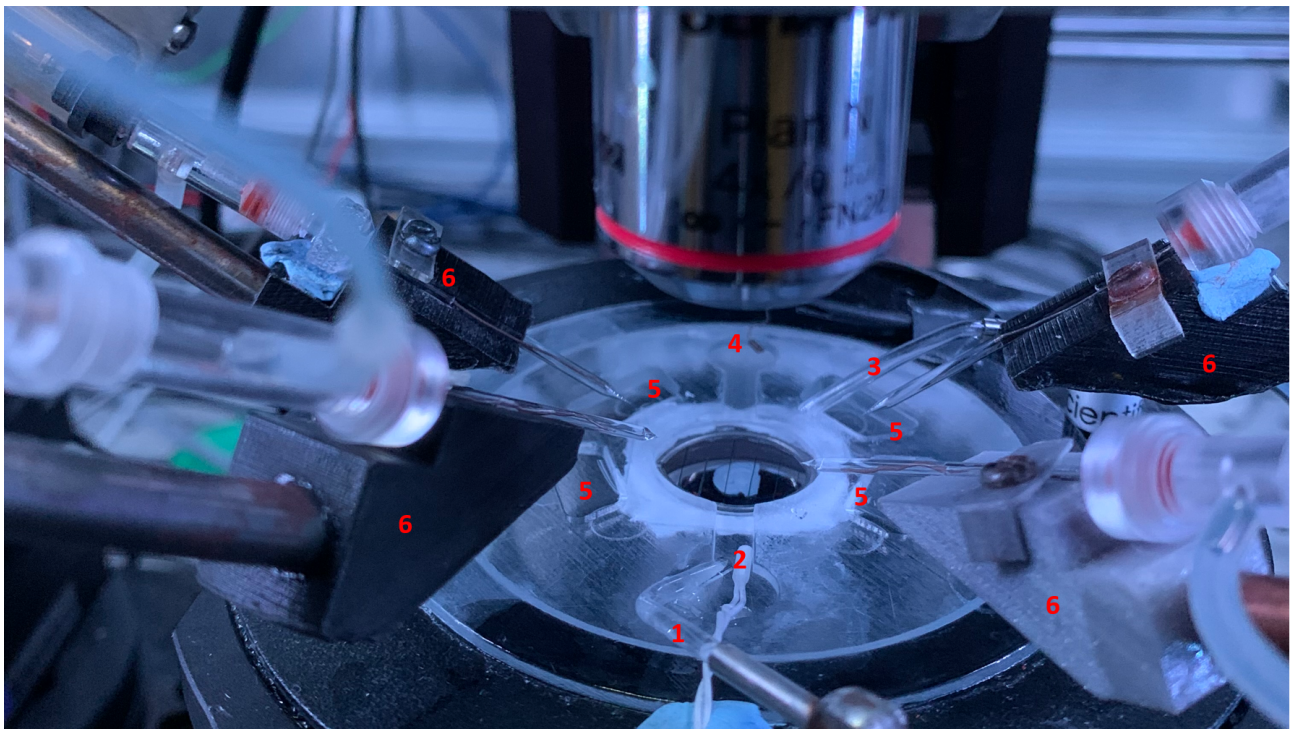


Figure 3.4: The setup from up close. A harp can be observed clamping down a brain slice into place. (1) Inlet for the perfusion system. (2) Heating probe from the heater system. It measures the temperature periodically to ensure through a PID system (closed-loop control based on proportional, integrative and derivative gains) that the inlet tube is heated sufficiently such that the temperature is the right one in the chamber. (3) Suction for the perfusion system. (4) Grounding pellet for the grounding system. (5) Detergent wells for pipette cleaning. (6) Pipettes placed in their corresponding electrode holders and held in place by mechanical stabilizer clamps. By clamping the pipettes closer to their ends as opposed to their tips, the vibrations and mechanical deviations at the tip are reduced. The tubes going to the pressure systems can be observed coming out of the electrode holders.

creating false positives. Therefore, this issue was solved by adding a small reservoir in the middle of the perfusion system that creates a break between the reservoir at the top and the chamber at the bottom, which effectively gets rid of the oscillations.

Chapter 4

The software: RITA

We must bear in mind that in the automation of any technique, it is crucial to understand in depth how researchers perform it, analyzing the parameters that lead to success and failure. This often entails for engineers themselves mastering the technique, as was my case, to best understand why it is done the exact way it is and how to best automate it. The best automation will not always lead to a step by step way of how people perform the technique (Kodandaramaiah et al., 2013). In fact, traditional multi-patching entails careful approach of each cell with the pipette, to then seal and proceed to the approach of the next cell, while routinely monitoring the sealed cell so that it is not lost. The complex set of visual cues and manual dexterity that humans have to routinely check on the patched cells while moving the pipettes would be much harder to do on an automated system. Thus, in our automated system, the four pipettes move at the same time so that all the deformation happens simultaneously and the need to check on patch cells is bypassed. Automation often needs to rely on less complex modalities and thorough software design that overcomes hardware limitations, as for example manipulators have different qualities than human hands and thus cannot perform the same actions. All of this, including how hardware and software limitations were dealt with, will be discussed in this next chapter.

4.1 Introduction to RITA's algorithm

All the hardware elements in the setup (discussed in the previous chapter) are controlled using a custom-developed LabView (National Instruments, Austin, TX) program which acquires frames directly from a two-photon microscope, and is capable of both blind and two-photon targeted quad-patching, by moving the pipettes to the target cells, analyzing the image feed, monitoring resistance and applying appropriate pressure. It was named RITA (Robotic Integrated Targeted Autopatcher) by the author of Annecchino et al. (2017), in honour or Rita Levi-Montalcini, the Italian Nobel laureate, and the name was kept for continuity.

When RITA is first run, the software checks that MultiClamp Commander (Molecular Devices), the only other software needed, is running, which interfaces with the amplifier for the electrophysiology signals. If it is not, the user is informed and the initial running of the program is aborted. Otherwise, the loading of the different modules takes place. Afterwards, the configuration and settings for all the hardware - chosen by the user in the dedicated tab of the main interface- are incorporated for use in the session. This includes COM ports for the different input/outputs, speeds for the manipulators, desired step length, sealing and break-in parameters, etc (Fig. 4.6). These parameters are saved from one session to the next, so the user only needs to set them once (as long as nothing changes). Configurations that the user might want to change depending on the experiment include setting the active channels/manipulators for the day.

There is also an initial calibration of the manipulators that needs to be done for each channel the first time running RITA. The software requires two angles: the elevation and azimuth angles, each requiring its own calibration (Fig. 4.1). These angles can be quickly acquired with a few clicks from the user, after they have positioned the dye-filled pipettes under the microscope.

Positive pressure is applied to the pipettes with the custom pressure system, to avoid blockage. In case of clogging, detected by an increase in resistance, the system can send pulses of increased pressure to try to get rid of the blockage, or send the pipette to clean in the detergent well. The positive pressure values used, 10 kPa and 5 kPa, were chosen so as to minimize the background fluorescence (that comes from the dye ejected by the pipette) and excessive brain deformation (which tends to happen when pressure is too high), while also avoiding obstructions. Angle calibrations for the manipulators aside, the micropippette tips only need to be manually ac-

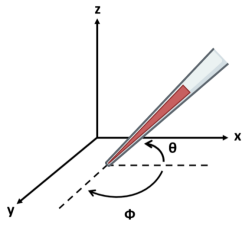


Figure 4.1: The elevation angle, θ, is the angle between the pipette and the x/y plane where the sample is. The azimuth angle, ϕ, is the angle between the pipette and the x-axis, within the x/y plane. These angles are crucial in translating the movements of the manipulators into the pipette coordinates. For more information on this translation, read Luca Annecchino's PhD thesis (Annecchino, 2016).

quired once at the beginning of each trial, and can then be manually or automatically lowered to the desired depth (surface of the brain). A 'follow' function is available to allow the user to move a single pipette and have the rest follow, both in the z and x/y coordinates. In this way, even if the user prefers a manual mode to lower the pipettes, the system works in their favour by reducing the labour by a factor of four. After each trial, the pipettes can be automatically cleaned and returned to their previous positions, allowing for their reuse. Clicking one button allows all channels to be offset, their voltage step functions to be activated and the pressure set to the required value, leaving them ready for the next trial. Because different cells and thus regions of the brain may be targeted for different trials, the 'follow' function also allows the user to manually move all pipettes to the new region in a swift manner (when the pipettes are outside the brain, as moving while inside would create excessive tissue destruction). Alternatively, pipettes can be automatically sent to a certain depth. Temperature control for the perfusion system is also possible within the software through a Peltier system (Scientifica Ltd). The experiment notes section automatically records the output of each channel in each trial, input resistance, series resistance and membrane potential of successful seals and break-ins, as well as an image of the target cells, labelled with the channel that was used for each cell. This is complemented by the recording module, which automatically documents all other valuable information such as electrophysiology and pressure signals versus time, target coordinates, pipette coordinates and state of the pipette (hunting, sealing, etc) along time. Basic injection and connectivity protocols (Fig. 4.14) are also available to run within the program, making the software a complete set for the basic needs of any experimenter, regardless of their skill set.

Target cells can be selected by scanning the brain, where the software automatically detects

candidate target cells in the field of view. Information acquired about each of these candidate cells includes boundaries, centre of mass (COM) in the x/y plane, contrast focus score (CFS), etc. The user can select the desired targets out of all the possibilities by simply clicking on the cells. The automatic approach can at this point be initiated, and each pipette will move towards its target.

In the *ex vivo* targeted mode (brain slices), a 3D stack of the target cells is acquired (250 x 250 x 20 μm). It is the centre of mass (COM) that is used as the x/y target coordinates for the pipettes, so as to patch in the centre of the cell, while the z comes from the plane at which the CFS (Contrast Focus Score) is maximal. CFS compares the outer edges of the selected cell to the background closely surrounding the cell, to determine if the cell is sharp and in focus or blurry and out of focus. If a fluorescent target is in focus (i.e. its boundaries are crisper), it will receive a higher score in that plane than in an out-of-focus plane where the boundaries are blurred, because the difference between the background surrounding the cell and the edges of the cell is larger than in the blurred case. By finding the plane in the stack with the highest CFS, the program is able to determine which is the COM of the cell in all three axes, to target precisely those coordinates. Once the COM of the targets is determined, the pipettes simultaneously align in the x/y plane to a position where they have a direct path along the approach angle to their targets. This is followed by a single step movement along said axis, which leaves them in contact. At this point, the sealing protocol is activated. Break-in can be manually activated subsequently, if desired. By avoiding numerous pipette movements, we minimize manipulator error and thus cell-pipette distance.

For 'blind' quad *ex vivo* mode, the impedance of the pipettes is closely monitored to detect the presence of a cell near the tip as they move through the brain. When a cell is detected, movement in all other pipettes stops, and the sealing protocol is activated for the tip in question. Once a seal is achieved, the other pipettes resume the hunt, and when all have achieved a seal, break-in is activated in all the channels. We followed the strategy by (Kodandaramaiah et al., 2018), which concluded that sealing the cells as they were reached was the most successful approach (even if it exposes the cells to the internal solution for longer, which is detrimental for them) because otherwise cells are lost as the brain is deformed by the other pipettes' motion.

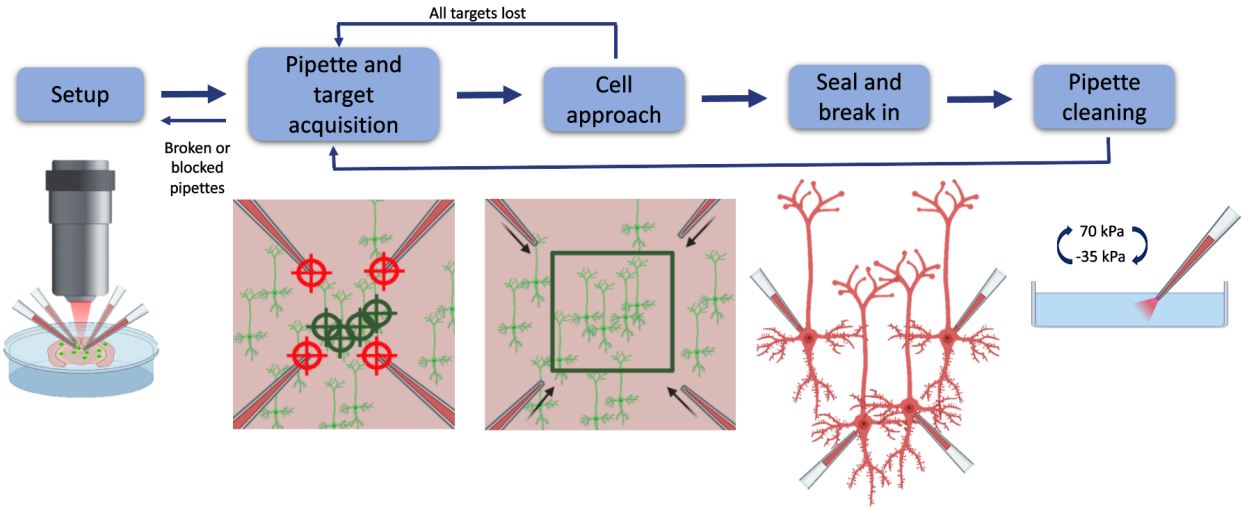


Figure 4.2: Algorithm for the targeted quad *ex vivo* mode presented in this thesis. After setup, the user first centers the Field of View (FOV) on the pipette tips and acquires their precise locations (depicted as red circle-cross overlays) which allows the algorithm to estimate the pipette positions based on micromanipulator displacements for the rest of the robot operation, without continuous visualisation of the pipettes. Pipettes are exchanged before proceeding if they are broken or clogged. Then, the user selects the targets (depicted as green circle-cross overlays) out of the cells detected by the software. Following that, the algorithm uses a 3D stack to determine the exact coordinates corresponding to the centre of the targets and takes one singular step in the xy plane and another in the axial approach towards the targets. The single-step approaches should leave the pipettes touching the cells, which is then followed by the simultaneous sealing and breaking-in. Once the WCRs have been acquired and the user has finished recording, the pipettes are sent to clean, where alternating pulses of positive and negative pressure are applied to clean the tips and prepare them for the next trial.

4.2 Preceding work: Annecchino system

This project is based on the system developed by Annecchino et al. (2017). This system was developed for single *in vivo* patch-clamp. The system here presented is for quad *ex vivo* patch-clamp, as a intermediate step towards quad *in vivo* patch-clamp.

In the targeted *in vivo* mode presented in Annecchino et al. (2017), a closed-loop algorithm was used, because breathing, heart motion and pipette movements induce target migration. The pipette approaches the target in an automatic step-by-step mode, while the microscope repeatedly acquires images around the target location and updates the coordinates whenever targets move position. This information is used to iteratively update pipette trajectory during

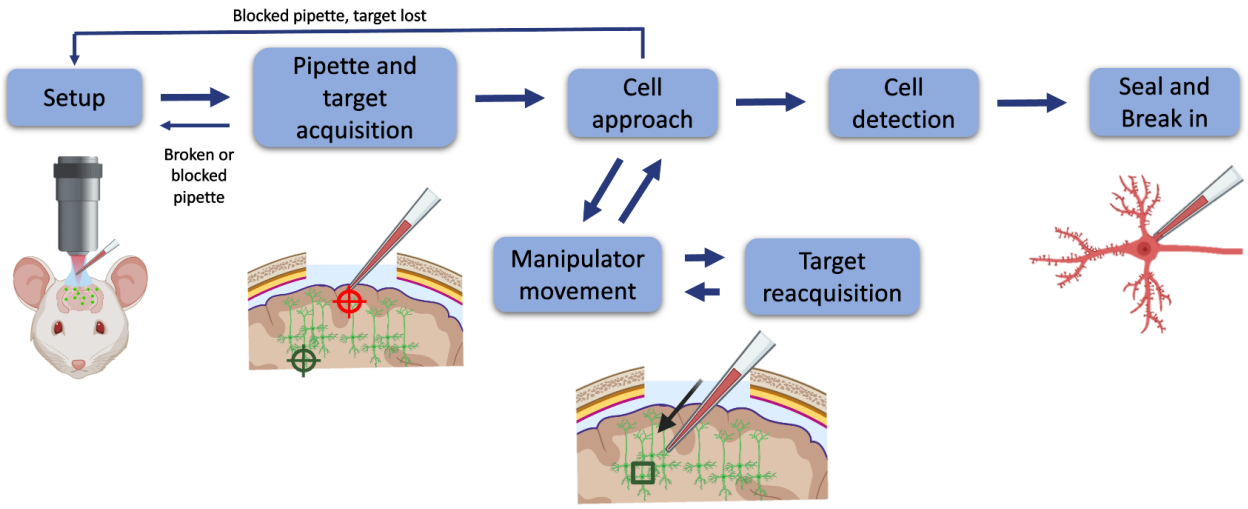


Figure 4.3: Algorithm for the targeted single *in vivo* mode presented in (Annecchino et al., 2017). After setup, the user first places the pipette tip on the center of the FOV and acquires its precise location (depicted as a red circle-cross overlay) which will allow the algorithm to estimate the pipette position based on micromanipulator displacements for the rest of the robot operation without continuous visualisation of the pipette. The pipette is exchanged before proceeding if its discovered to be broken or clogged. Then, the user selects the target (depicted as a green circle-cross overlay) from the cells detected by the software. Following that, the algorithm moves the pipette towards the target in 2 μm steps while continuously imaging the cell and making adjustments to the trajectory based on target displacements. If during the approach the target cell is lost or the pipette gets clogged, the trial is reset, and the pipette and target are reacquired. As the pipette enters the the vicinity of the cell, the algorithm checks for an impedance increase to detect the cell. An impedance increase above a set threshold will trigger sealing and subsequent break-in. Once the WCR has been acquired, the user can proceed with recording, after which, the pipette is discarded and a new one is installed for the next trial.

the approach. The algorithm can be observed in Fig. 4.3, in contrast to the one developed for quad *ex vivo* mode, that can be seen in Fig. 4.2.

The application developed by Annecchino et al. (2017) was written entirely in LabVIEW, a National Instruments graphical programming environment, and therefore the expansion to four channels was also implemented in LabView. "LabVIEW programs are called virtual instruments, or VIs, because their appearance and operation often imitate physical instruments, such as oscilloscopes and multimeters" (NationalInstruments, 2022b). The bare-bones structure of the low-level subVIs is pervasive from the previous RITA, but practically all high-level VIs are

completely original and most of the subVIs have been through heavy remodelling, not only to adapt to the multiplicity but also to simplify and optimize the algorithms when possible, so as to reduce CPU usage. Some of the VIs that remain from the 2017 version are the calibrations VIs, hunting VI and image processing VI. The principal thing to bear in mind is that, aside from the extension of the platform to four channels, the algorithm was greatly optimized, to the point that the main pitfall of the previous system; the final manual positioning, is now unnecessary, making the approach fully automated. It now also includes cleaning, for the automatic reuse of pipettes, in such a way that the user is only needed at the beginning of each trial to acquire pipettes and targets and press the relevant button to start the automated process.

Furthermore, there are a vast number of new functionalities added, as explored in the next section.

4.3 Implemented changes, expansions and added functionalities.

4.3.1 New Interface

LabView uses graphical blocks to code, and a front panel GUI (Graphical User Interface) that allows the user to interact with the code. The previous GUI (Fig. 4.4) lacked the space for expansion without the use of scroll bars or endless tabs. Therefore, the interface was completely redesigned to support the four channels within the available space. Unnecessary and/or unused variables were removed. Parameters that are assigned a value only once were relocated to the configuration tabs. The new graphical user interface (Fig. 4.5) has been designed to be as user-friendly as possible: to help the experimenter keep track of the different functionalities, they are organized in different modules: imaging, pressure-control, manipulator(s) control, electrophysiology control, cleaning, etc. To help keep track of the four different channels/pipettes, they are colour-coded, matching the colour that each channel would have in a classical oscilloscope (where traditionally, electrophysiology signals are observed). Stickers of the same colour were added to each of the physical manipulators and pressure systems, to help make the experience more seamless (an idea borrowed from Jesper Sjöström's lab). Furthermore, explanations were added where necessary, for user-guidance, on how to navigate the program. In modules that

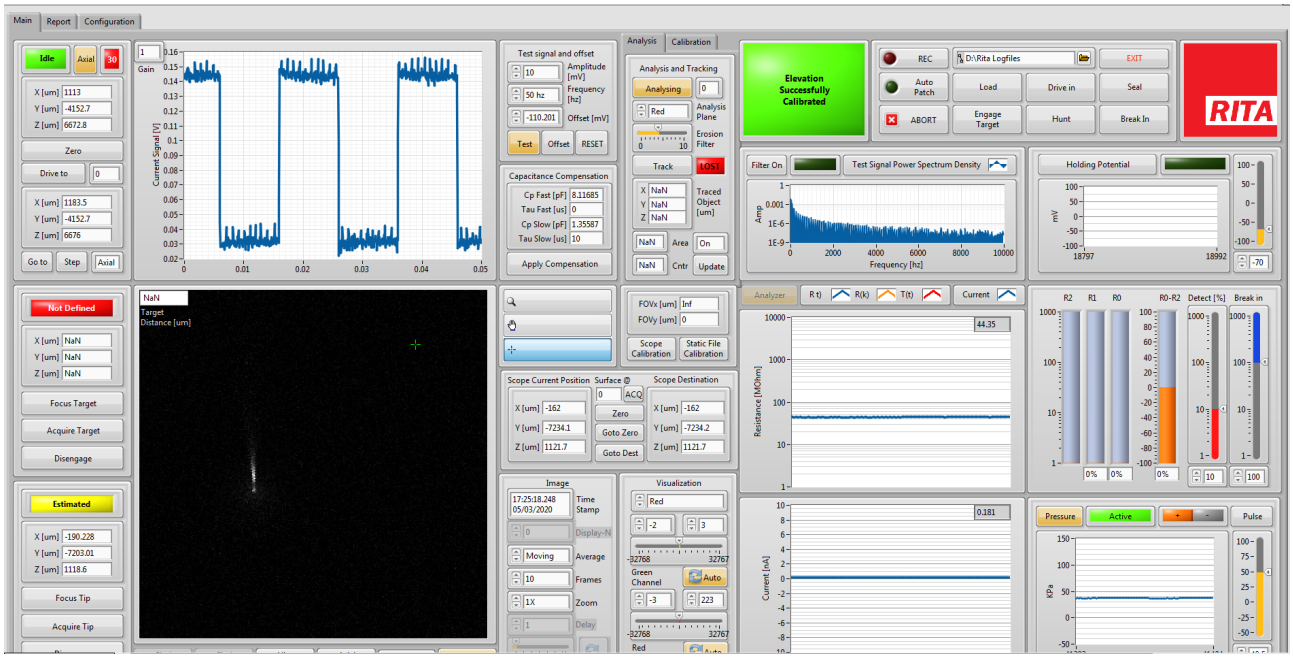


Figure 4.4: GUI of the software developed by Annecchino et al. (2017) for single-channel automated patching. A clogged tip can be observed in the image feed. The lack of the characteristic diffusion pattern of the fluorescent internal as it exits the tip denotes that it is clogged, as well as its measured impedance (44 Ω).

mainly contain commands to be sent, the user can toggle between the four channels (e.g. manipulator or electrophysiology command tab). However, in the modules where variables are being acquired real-time (e.g. pressure), all four are displayed at the same time.

On the top left, the controls relating to the manipulators can be observed. Most of the controls are specific for each channel, so they are contained within the color-coded tabs. The two top controls outside the tabs show the channels that are active for the session and the speed at which the manipulators are moving. The active channels can be chosen on the configuration tab and helps RITA be more efficient in the case that one of the channels is not working on a particular day or if the setup has less than four manipulators. RITA is prepared to work with any number of channels/manipulators between 1 and 4. The speed control is also essential. The actual values for the high and low speed can be selected in the configuration tab but we recommend maintaining the default values, as they have been proven to be effective. RITA overrides the speed at which manipulators can move to a low speed during the hunting ('blind') or targeting steps of the algorithm to avoid sudden and large movements. A high speed, however, is needed at the beginning of the session to manually introduce the pipettes into the field of view, as well as automatically move the pipettes to and from the cleaning

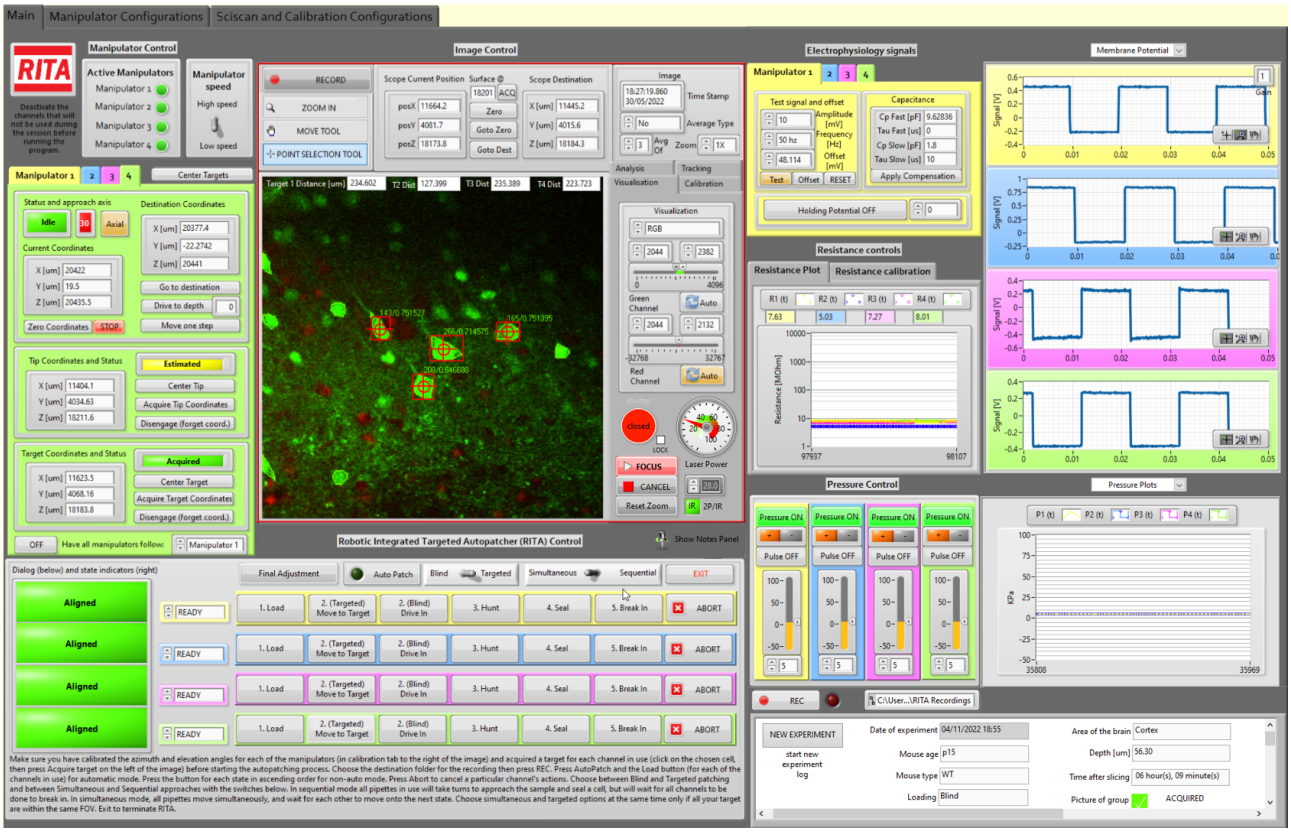


Figure 4.5: New interface of the RITA software, which was designed to be as user-friendly as possible, with functional modules and color-coded channels. Main tab. Four fluorescent cells have been selected by the user and they are being tracked by the software. This tracking is obvious by the red enclosing rectangles around the selected cells together with the target symbol within. The states of all four channels is READY meaning there are no errors and the user can now choose to initiate the trial. On the right, the step current signals for all four channels can be observed. The resistances of the pipettes are within 4 and 7 MΩ, denoting no clogged pipettes. The pressure values set at +5 KPa for each channel, and the measured values are in accordance. The filled in notes of the experiment can be observed in the bottom right module.

wells during cleaning. The module on the right of the manipulators is the imaging module. It contains the two-photon (2P) or infrared (IR) images (depending on the selected mode), controls for the stages and objective, laser power output, image analysis controls, etc. This is the module that has changed the least from Luca Annecchino's version, as it was expanded to track several targets but the image analysis remains similar. The button to change from IR imaging to 2P imaging can also be observed at the bottom of this module. The module at the bottom of both the imaging and manipulator modules is the autopatching module. Each row corresponds to a specific channel, with its corresponding characteristic colours. On the leftmost part of this module are message dialog screens to inform the user of progress in each of

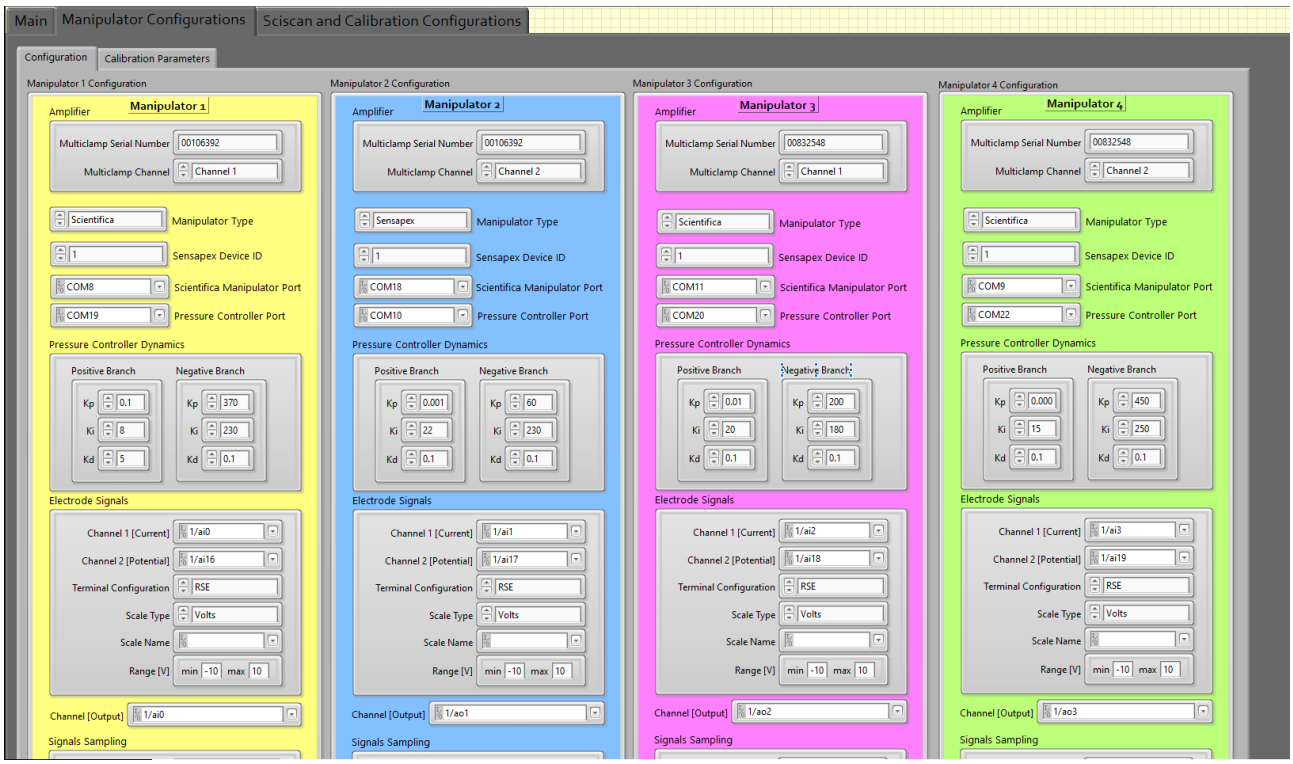


Figure 4.6: New GUI of the software. Configuration tab. This tab contains settings and parameters for the four channels that the user configures before running the software. These primarily include manipulator, amplifier, and pressure system hardware settings, signal acquisition parameters, pressure system PID settings (Proportional, Integrative and Derivative gains for the closed-loop control), and sealing and break-in parameters.

the channels. Right next to it are the states of the channels: READY, HUNTING, SEALING, BREAK-IN, ... corresponding to the button that has been (automatically or manually) pressed from the same row. On the top right, next to the imaging module, is the electrophysiology module. It contains the commands to activate the seal test, offset the signal, activate the holding potential, get rid of the capacitive components, etc. It communicates the commands to MultiClamp Commander, which in turns sends them to the amplifiers. On the right of this module there are the plots for the voltage/current of each of the channels (depending on which mode they are in: current or voltage clamp, respectively). The resistance calculated out of these signals is plotted on the left. This resistance is used to detect cells in the hunting ('blind') mode. Below the electrophysiology module one can observe the pressure module, with controls to dictate the individual target values for each channel, buttons to turn them ON/OFF and measured values to corroborate their correct functioning. The plotting of the pressures can be momentarily changed to show instead the cleaning controls or the heating controls, as both of these modules are not used at the same time. Finally, on the bottom left one can find

the experiment notes. In this section we also find the REC(ording) button, which stores the pressure, electrophysiology and impedance signals, the position of the targets and tips and the states that each channel when through along time recorded. Next to the REC button the user can choose the folder in which the notes and the recording will be stored.

4.3.2 Paralellization: Re-entrant VIs.

LabView's programs (VIs) can be run in parallel, thanks to its inbuilt multitask ability. This is crucial for the correct functioning of a software such as RITA, where there are four channels that need to be doing the same task or a different one, depending on the modality (sequential versus simultaneous). Quad-channels aside, it is obviously also necessary for the single channel version of RITA, for example, to be able to image and keep track of the target (e.g. imaging VI) while another VI (e.g. Manipulator control VI) moves the manipulator towards the target. When expanding RITA for quad patch, there were two common types of VIs: (1) VIs that needed to take all four manipulators/channels into consideration (e.g. the imaging VI that needs to track all four targets) and that were expanded from within and (2) VIs that were specific to a single channel (e.g. Manipulator control VI) and that, theoretically, could just be copied over three more times. This, however, is not possible without renaming them (Manipulators control 1, Manipulator control 2, etc) and placing the four copies on the main VI and corresponding folder, each with their own inputs and outputs. The main reason why this is necessary is because without the different names, LabView will identify them as the same VI and will not run them simultaneously and potentially mix the input and outputs. Any change to the code would need to be reproduced in all the copies. Copying the VI four times over is obviously a very non-efficient and disorderly way of building code. Another reason not to proceed like this is that, for each of the subVIs present in the Manipulator control VI, copies would need to be made as well, making the expansion increasingly chaotic, as there can be up to 8 layers of VIs within VIs in RITA. The reason why copies would be needed is that if instead of copies, a single set of subVIs was left to be used between the four VIs, they would need to wait for one to finish running for the next one to run (which is not necessarily a problem if taken into consideration) but most importantly, cross-talk is likely to happen if proper care is not taken. Instead of this, a neater and simpler way was chosen: re-entrant VIs. With re-entrant VIs, one can allocate non-shareable, unrelated clones of the same VI that can run in parallel

with no cross-talk. They are memory intensive so they were only used when strictly necessary, mainly pressure and manipulator control, auto-patching and cell targeting. While there is still some bottle-necking of certain subVIs, it does not seem to impact the overall performance, and there is no chance of cross-talk. Furthermore, only active channels will lead to a clone being created for them, reducing unnecessary computational load. Figure 4.7 shows an example of a re-entrant VI in RITA.

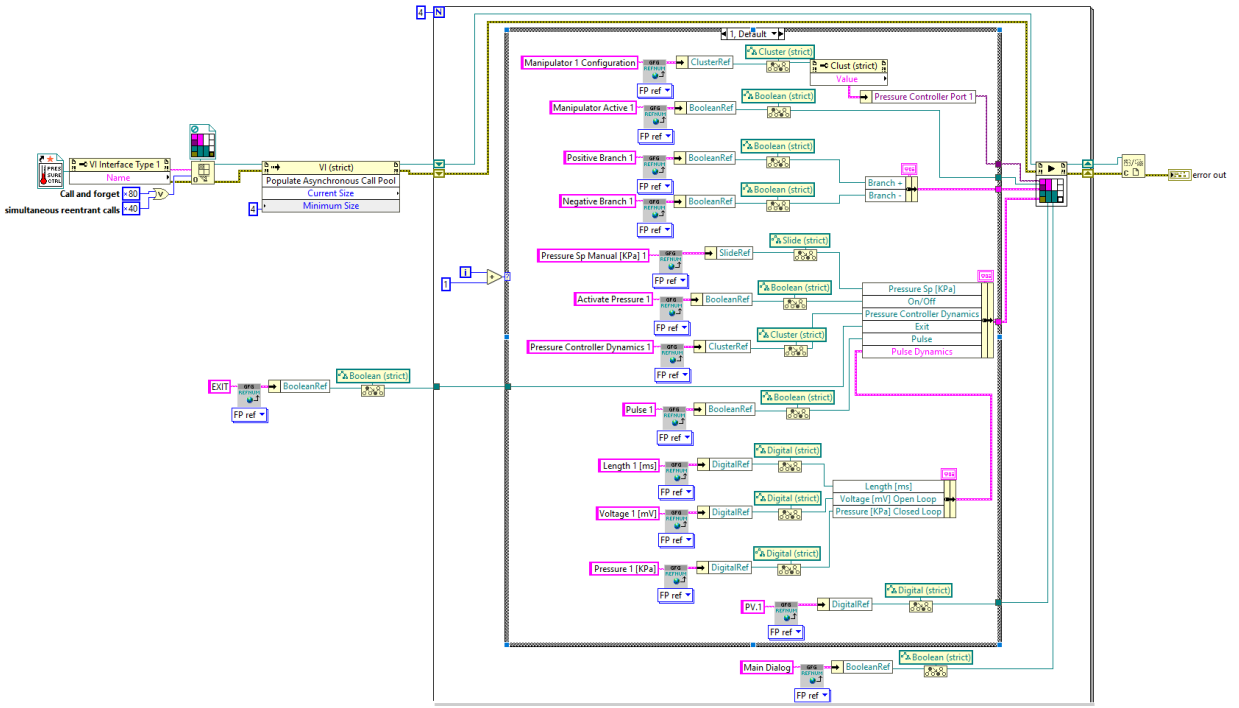


Figure 4.7: VI containing the re-entrant pressure control VI. The outer structure determines the number of clones (4) to be created of the VI on the left (Pressure control VI). Within that structure there is a case structure that feeds the corresponding inputs to the corresponding clone (only channel 1 is shown). This VI will generate four independent copies of the Pressure control VI, each with channel-specific controls that can run in parallel, eliminating the need for individual VIs to be created. Within the each of the Pressure control VI clones, the specific pressures are being set and measured, in the corresponding channel.

4.3.3 Sensapex manipulator compatibility

Given that target cells used during testing (pyramidal cells of layer 5 in the cortex) are usually 10 μm in width, and that for optimal sealing, the pipette should be in the centre of the cell, the margin of error in terms of targeting is extremely small, below 5 μm. Therefore, precision

and most importantly accuracy are crucial for the correct functioning of RITA. This is given by several factors: the accuracy and precision of the user when acquiring the pipette tips (i.e. selecting the tip within the FOV with a click), proper calibration of manipulator angles, the inherent drift and/or accumulative error in the manipulator movements, the target COM calculation by the algorithm, the calculation of the movements the manipulator needs to make – floating point number, etc.

We had the opportunity of determining the effect of each of these factors later in the project. However, it was the theory of the author of Annecchino et al. (2017) that the manipulator movement precision was the determining factor for correct targeting. Therefore, despite the increased price of Sensapex manipulators as compared to others in the market, one was acquired as part of the quad-setup. These manipulators have increasingly become more popular thanks to: (1) their small size, which makes them suitable for *in vivo* patch-clamp (Suk et al., 2019) and also multi-patching setups (Peng et al., 2019), and (2) their claimed 'highest accuracy' (Sensapex (2022)).

Including a Sensapex manipulator required the whole program to be adapted to this new type of manipulator, as it previously had only been used with a Scientifica PatchStar, which requires different commands and a different type of communication.

Scientifica manipulators have a 'manipulator query' VI through which the recognized commands can be sent to the manipulator directly, making use of VISA. "NI-VISA is an Application Programming Interface that provides a programming interface to control Ethernet/LXI, GPIB, serial, USB, PXI, and VXI instruments in NI application development environments" (NationalInstruments, 2022c).

The list of Scientifica commands is vast and includes commands to obtain the coordinates of one or all axes, set them to a different value, command the manipulator to go to certain coordinates or to take a step in a particular axis, stop movement, the speed and acceleration at which it moves, etc. An example can be seen in Figure 4.8, where the STEP command is being sent so that the manipulator will take a step of a predefined length in the axial direction.

These subVIs were already present in the Annecchino version of RITA. However, as previously mentioned, Sensapex manipulators require different subVIs. After inquiry, the Sensapex developers provided a LabView SDK, which was used to create the subVIs used in RITA. SDK

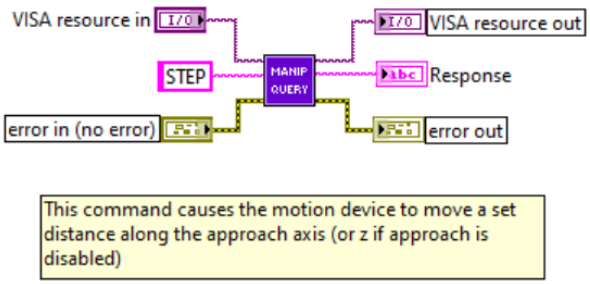


Figure 4.8: Step VI. The command STEP, which is recognized by the Scientifica Manipulators, is sent to them via the Manipulator Query VI, which can be observed in Fig. 4.9.

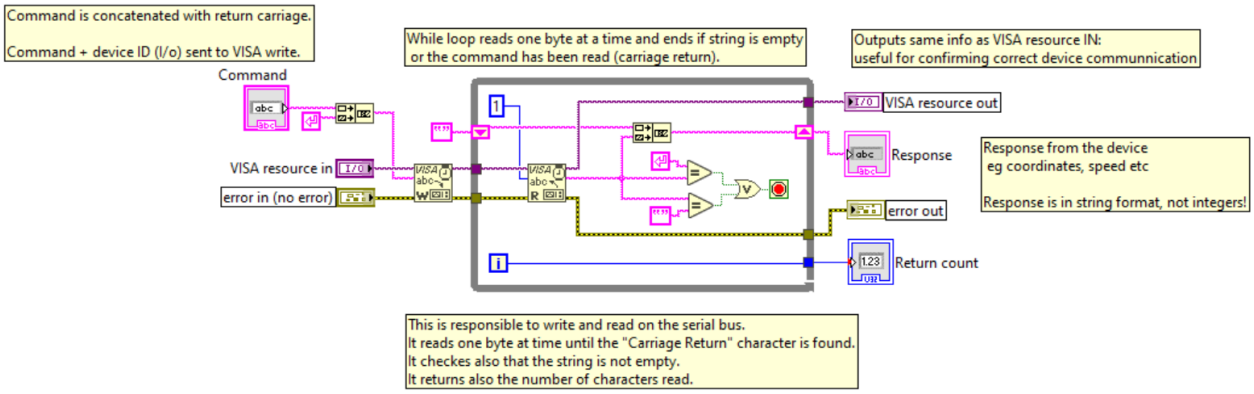


Figure 4.9: Structure of manipulator query VI, which is in charge of sending all commands to Scientifica manipulators through VISA. The query is sent one bit at a time in a series, and the response is read in the same way. Baud rate and other serial protocol parameters are set for the serial port ID to which the manipulator is connected.

stands for Software Development Kit. This is a complete kit of software development tools for a specific platform. It can include documentation, libraries, application programming interface (API), etc. In Figure 4.10 an example of the Sensapex subVI which is analogous to the Scientifica subVI in Figure 4.8 can be found.

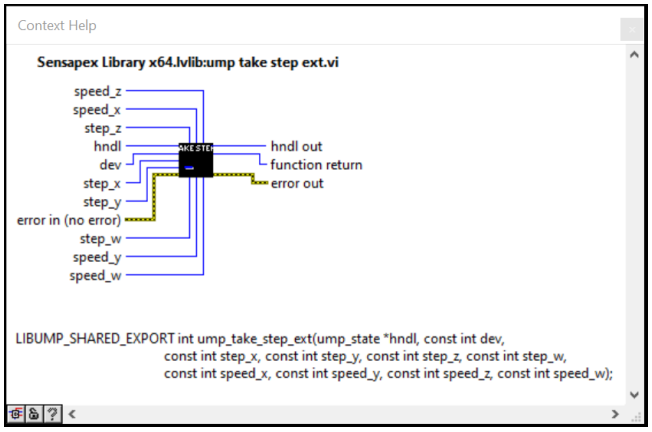


Figure 4.10: Send step VI for Sensapex manipulator. The VI accepts the step length for the specific axis to take a step in, speed settings, and an identifier handle for the current communication session with the manipulator.

Because RITA was coded to work with only 3 coordinates, we had to make some adjustments to add the 4^{th} axis for Sensapex manipulators, which comes from the axial approach axis. The axial approach does exists in Scientifica manipulators, but does not have its own set of coordinates unless this option is selected in LinLab (their in-house software), as it is a 'virtual approach' axis. Even if this option is selected, the coordinates are not available outside of Linlab, as far as we know, so they cannot be used by RITA or any other external software. The fact that this 4th axis is physically independent of the others in Sensapex manipulators grants them a larger range of motion, as compared to the Scientifica ones, which is specially useful in multi-patching rigs. Furthermore, the minimum velocity for the Sensapex manipulators is lower than the Scientifica manipulators, which is also useful to reduce tissue deformation. Scientifica manipulators have a lower velocity called 'creeper mode' but in old models like ours, it is only available in the z-direction.

The Sensapex manipulator did not demonstrate a higher accuracy or precision in targeting (cell to pipette distance after approach) than the other three, which were (old) PatchStar manipulators. This could be due to the fact that the difference in precision between them (15 nm) is too low to have an actual impact on the task.

4.3.4 Dual MultiClamp 700B interfacing

In computer science, a class is a defined structure to create objects, with a set of rules on how they can be used. Hence, an object is a specific class instance, which can be any mixture of functions, variables and data structures.

Handles are abstract references to resources (such as objects or blocks of memory) that belong to a different operating system, database, or application than the one being used.

DLL stands for Dynamic Link Library, a type of library that holds data and code which can be simultaneously used by multiple programs.

Molecular Devices, the company that manufactures the widely used MultiClamp 700B amplifiers, provided upon request a DLL for controlling the amplifiers through their software, MultiClamp Commander. Each amplifier has two independent channels, namely Channel 1 and Channel 2, for recording and stimulation in two different electrodes, with each having voltage clamp and current clamp modes. As can be seen in Figure 4.11, the commands for both channels cannot be observed nor changed at the same time. In a quad system like ours, there will be two amplifiers and thus two open MultiClamp Commander instances, each with two channels.

A MultiClamp DLL object is generated when the VI in charge is initiated, with two handles to refer to each amplifier in the next function call (Devices 2016). While the handles for each amplifier are specific, the handles created for each channel within the amplifiers are not. They will in practice send the commands/read the values for the active channel (the channel that is being displayed) regardless of the handle used. Consequently, a solution had to be found to be able to command the different channels automatically. This had previously not been a problem because only the active channel was used in the single manipulator version of the program.

The answer came in the form of an unconventional yet effective override. By using DLL functions from the Windows User Application Programming Interface (Win32 apps), the program "clicks" on the desired channel before reading or writing values from/in it. This is thanks to the in-built keyboard shortcuts from the MultiClamp Commander software, that allow for four different shortcuts to refer to each specific channel. Our program first finds the Multiclamp Commander windows, then sends the corresponding shortcut (Figure 4.12), and then finally

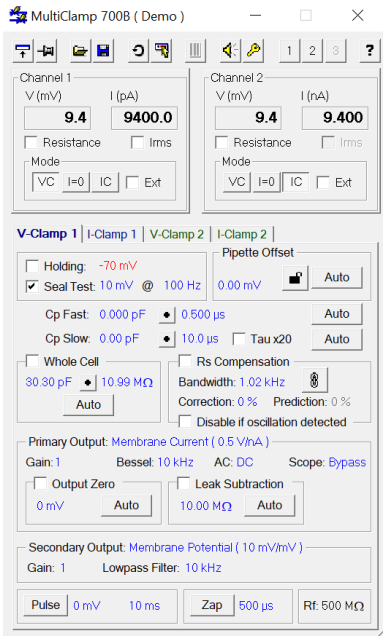


Figure 4.11: Multiclamp Commander 700B. This software serves as the control platform for all MultiClamp 700B functions, from basic parameter settings to other automated features enabled by the software interface. Many of these features can be accessed in third-party software such as LabView through the use of a custom dynamic link library. It has a voltage-clamp and current-clamp tab for each of the two channels/electrodes.

sends the desired commands.

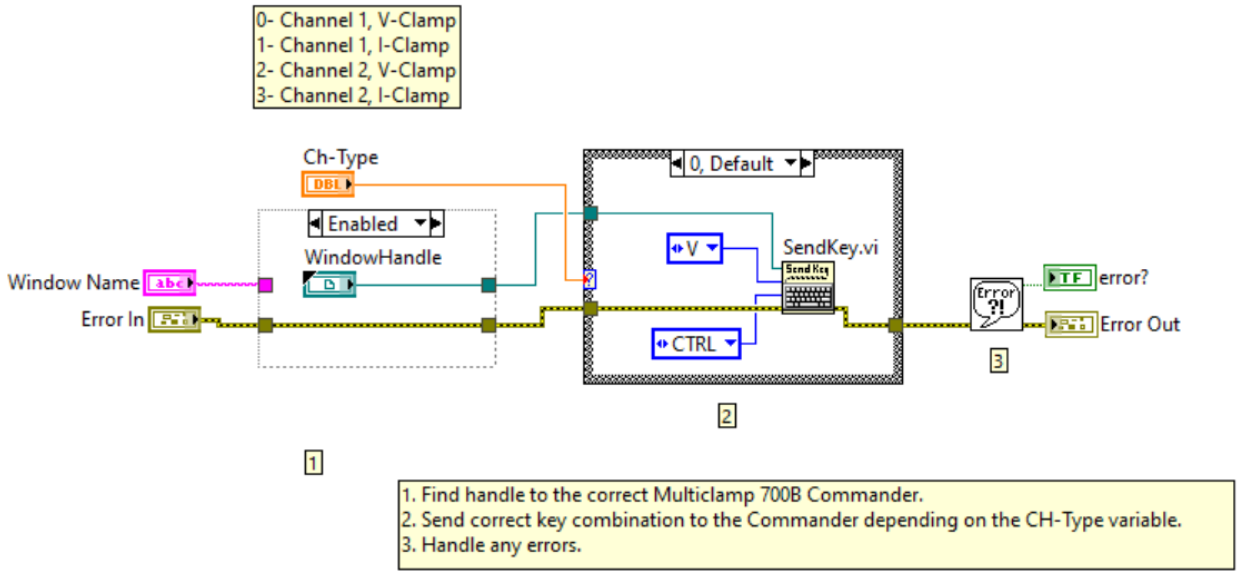


Figure 4.12: One of the VIs that allow proper communication between RITA and MultiClamp Commander 700B. This VI will send the shortcut needed to select the desired tab, which will then allow for commands to be sent and values read from Multiclamp Commander.

4.3.5 Temperature control

It is standard procedure to have warm aCSF perfused during electrophysiology experiments, both *ex vivo* and *in vivo*. Homeostatic temperature is crucial for the proper functioning of the brain. Temperature loss can affect the processing of information in the exposed areas and potentially in connected areas of the brain as well. Kalmbach and Waters (2012) proved that the exposed neocortex temperature in a craniotomy declines to 28°C, having adverse effects on cell and network functions. The same paper proved that perfusing the brain with heated aCSF proved effective in the maintenance of brain temperature. Therefore, an in-line Peltier heating device (Scientifica) was integrated onto the rig and software. The technology to communicate between LabView and the heating device is the same as the manipulators from the same company, so the integration was relatively straightforward. The device allows the user to choose a target temperature and the in-built sensor provides feedback for the PID control system, which regulates the heating component in a closed-loop manner through proportional, integrative and derivative gains.

4.3.6 Central Processing Unit (CPU) Usage

Shortly after the expansion to quad-capabilities started, it became obvious that the program was becoming too CPU-intensive to properly function. It would frequently hang the computer and randomly freeze some VIs and not others -that should be running in parallel- leading to errors that otherwise would not be present.

As a first step, the computer was upgraded to a new, more modern one, but this only solved the problem temporarily, because as more functions were added, the program became heavier. As a second step, a labor-intensive job of disposing of all the unused variables and VIs was carried out. Unfortunately, there is no way of checking definitively if a variable is used in a VI or not, so, often, this cleaning labor meant following wires to check their destination. As the original program was developed by a single person (Luca Annecchino) over his PhD, there were many unused variables and VIs that had become outdated when a different solution was tried during development and proved successful, which is to be expected, given the impressive amount of work achieved by Luca in such a short period of time. Afterwards, certain functions that were useful but less used were also removed. For example, originally, information on how

rapidly the pressure had changed would be calculated and plotted together with the current value of the pressure, but it was decided that this was actually not crucial.

The lack of an integrated imaging system in the program meant that Scientifica's Sciscan had to be run in parallel to our program, which understandably was taking up a lot of CPU usage. Therefore, a simplified version of this imaging system (with less capabilities) was incorporated into the program. This was performed by Phatsimo Kgwarae.

We also contacted NI to obtain their advice on how to best reduce CPU usage. They suggested using as few property nodes as possible, reducing the number of charts being plotted live and having a single VI updating the GUI instead of several. Property notes read and/or write properties of references, which means that every time a variable needs to be read or its value changed, a property node is required. Besides the previous cleaning of unused variables, we could not dispose of anything else, so nothing was implemented from this recommendation. We had also previously reduced the number of charts by plotting the values that could be plotted together in one chart (e.g., the pressure values of all four channels in one single plot). We could also see no way in which we could have the GUI VI updated by a single VI that did not involve a complete and very complicated reprogramming, so this was not implemented either.

Another solution recommended online was to control the autoresizing of clusters (NationalInstruments, 2018), which is not done by default. Clusters are containers capable of grouping data of different types together; and used often throughout the program. To avoid unnecessary empty space in clusters and avoid overlapping controls over the resizing, autoresizing to arrange them either horizontally or vertically should be chosen. This keeps them compact, and it is more CPU-efficient.

Some also suggested parallelization of loops using an in-built tool. This executes the iterations of a 'For Loop' concurrently in multiple threads, yielding greater CPU utilization and reduced processing time on multicore machines.

These two solutions had a reduced effect. The change that yielded the biggest CPU reduction was 'Dynamically calling and loading VIs' (NationalInstruments, 2022a). This meant a complete remodeling of the VI controlling the GUI (the main program) to call and load the different subVIs on command. This work was done by Phatsimo Kgwarae. Previously, all VIs residing in the main program would continuously run and wait for event triggers to execute certain parts

of the code (event/case structures in while loops). This is known as statically linked VIs and it is the default. With this system, all VIs run at start-up, loading up the CPU. Furthermore, different references of the same variable are fed/wired onto different VIs, as many variables are used in several VIs at the same time. After the remodeling, all the variables and controls on the main VI became available globally and could now be accessed anywhere. A single VI waits for events and calls the requested VIs programmatically, which are loaded then, and can be released once used. The called VI will then access the control references that it needs without any wiring.

This means that VIs that perform functions that are only needed at certain points, will only run when required. Examples of this are VIs in charge of recording, the 'follow manipulator' function, pipette cleaning, heating, saving coordinates etc. In addition to lowering CPU overhead, this structure permits new functionality to be added effortlessly (owing to variable accessibility), without the need for wires. This can be observed for example in Fig. 4.20.

Additionally, some elements of the GUI are now only shown when required, reducing the number of variables requiring updating and plotting. This includes standalone VIs that are called onto subpanels on the main GUI – e.g. A window that displays pressure plot at one time, cleaning commands at another (see figure 4.18).

4.3.7 Experiment notes

This implementation was carried out by Phatsimo Kgwarae, following a structure designed by me, the person with experience in patch-clamp experiments, and thus who knew which parameters and signals are commonly written down and/or stored by experimenters for the posterior characterization and analysis of the cells.

This implementation basically expands the recording capability present in RITA (2017) by including experiment summaries that are saved as text files. The summaries include experimenter notes, a labelled image of the target cells to discern which channel patched which cell, the membrane potential of the recorded cells, their input resistance, time elapsed since slicing, age of the animal, etc, as can be seen in Fig. 4.13. The outcome of each trial for all four channels is automatically recorded (successful/failed seal/break-in), as well as the membrane voltage, input and series resistance (after a period of 2 minutes, to assume stability), saving ex-

perimenter's time. Given that most variables and parameters are available globally (see section on CPU implementation), this VI simply stores these values onto a text file. It also interacts with the Multiclamp Commander VI to fetch from this software the remaining values.

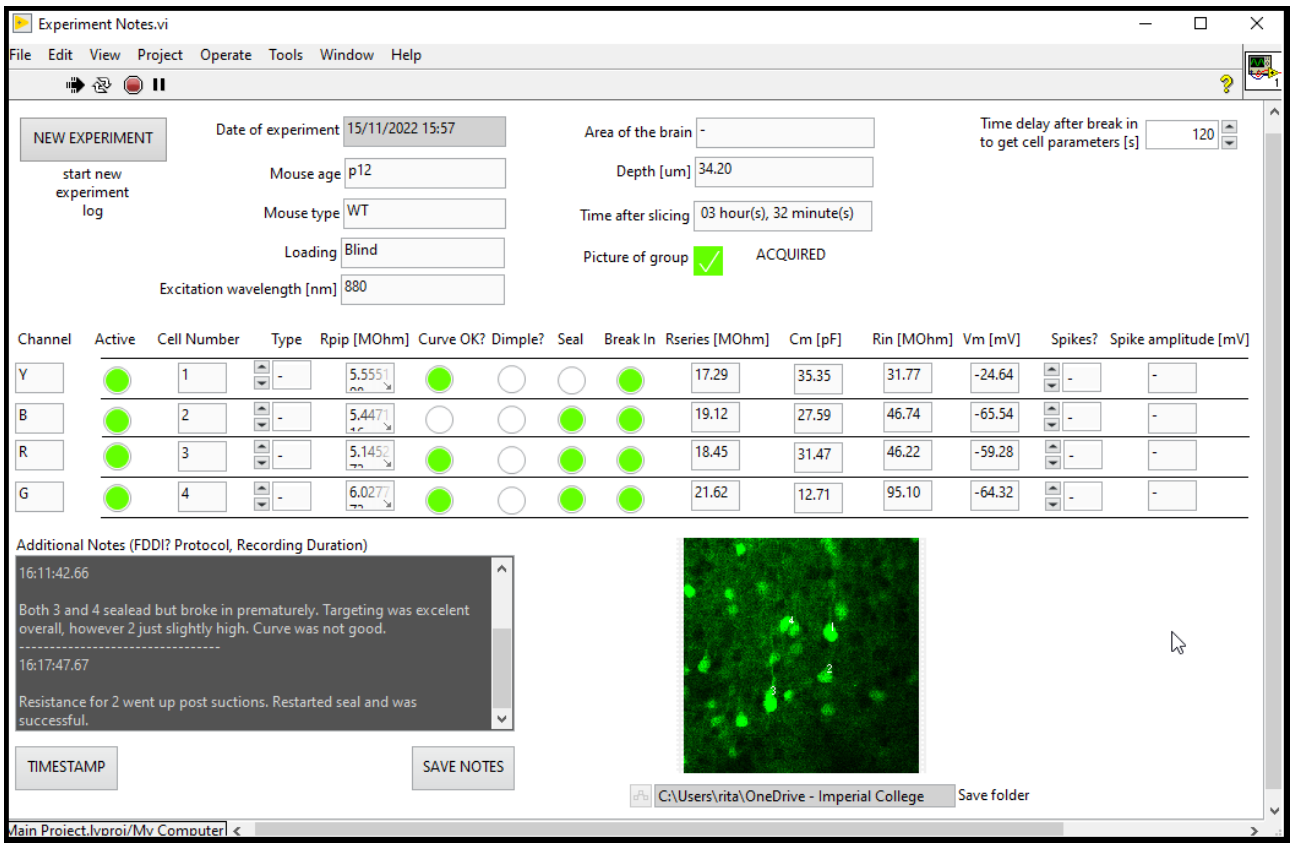


Figure 4.13: Experiment notes. This VI records experiment summaries that are saved as text files. The summaries include custom notes written by the user, a labelled image of the target cells (to determine which channel patched which cell), pipette resistances, time elapsed since slicing, animal age and type, type of experiment, excitation wavelength used, depth of the patching, and cell parameters automatically populated after break-in: membrane potential, input and series resistance, membrane capacitance, etc.

4.3.8 Current injection protocols

This implementation was carried out exclusively by Phatsimo Kgwarae, following a structure designed by me, the person with experience in patch-clamp experiments. I also helped debug it, as it was not a straightforward implementation that took us several months to implement correctly.

This implementation allows the experimenter to run basic current injection protocols in current-

clamp mode within RITA. There are two main ones. For basic characterization of the patched cells, there is a current injection protocol. In default mode, it injects 20 current steps of increasing value, starting at -100 pA and increasing in 20 pA step, and measures the voltage response of the cells (Fig, 4.14). To check for connectivity between cells, the default program consists of a minimum of 10 trains of 5 pulses each (of 1.3 nA at 50 Hz). Then an average is calculated to see any possible Excitatory Post-Synaptic Potentials (EPSPs). Injection currents for the different cells are interleaved, such that if for example cell 2 has an excitatory response to spiking in cell 3, the response is recorded (as seen in Fig. 1.3). However, all the parameters can be tuned by the user: number of pulses, pulse amplitude, pulse duration, spacing between pulses and trains of pulses, number of trains, incremental value, etc. Thus, any current-clamp protocol based on current injections should be theoretically programmable within RITA.

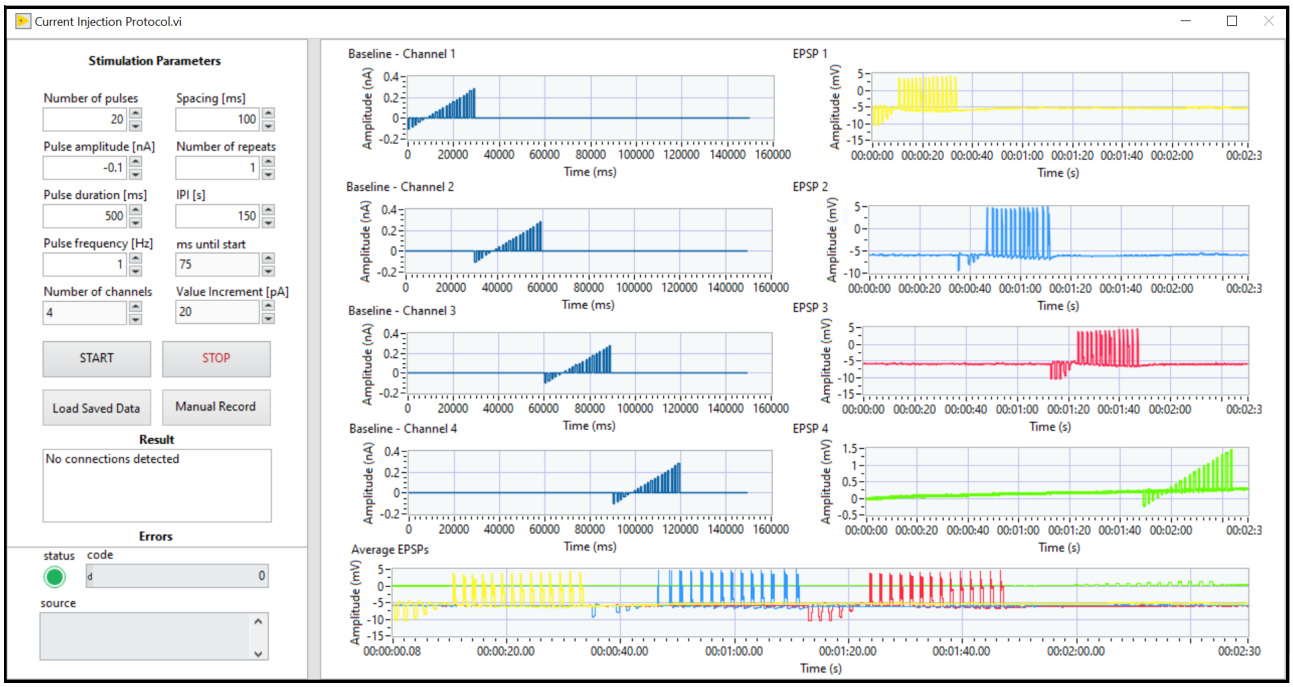


Figure 4.14: Current injections protocol panel within RITA. The left panel shows the different parameters that can be adjusted, as well as a 'Load' button to open past experiments. The plots on the right are the voltage of the cells in response to the current injection protocol seen in the middle plots. At the bottom, the voltage of all four cells can be seen at the same time. There were cells on channels 1, 2 and 3 but not in 4, as denoted by the lack of spiking even at high currents and the resting membrane potential.

Initially, this implementation was coded using the tools we had used in the rest of RITA: because pulses can be triggered via Multiclamp commander, the VI in charge of these patterns would 'click' on Multiclamp Commander and send the command to that software, which will

in turn send it to the amplifier (as explained in section 4.3.4). However, the execution of the VI, consisting of a Call Library Function Node (calls a DLL or shared library function directly), took longer than 20 ms and so 50 Hz could not be achieved for the connectivity protocol. Additionally, the time between pulses was variable from iteration to iteration, making it impossible to sum up and average signals. Thus, the final solution consisted of generating the pulse patterns within LabView, converting them to waveform signals which are then sent directly to the analog outputs of the channels (and into the COMMAND signal input of the amplifier). Even with this solution, small variations can happen from iteration to iteration, so recorded signals are aligned by first calculating their correlation to a common signal and shifting the signals in the time axis by the amount of lag needed for maximum correlation.

4.3.9 Optimization of the targeting algorithm

At the beginning of this project, efforts were made to expand the platform developed by Annecchino et al. (2017) to make it capable of quad-patching.

The software was first analyzed and thoroughly commented, to aid the labour of understanding the very complex code and, at the same time, make it more amenable to future users, who might need to fine-tune the code for slightly different conditions. Afterwards, changes were made, as described in previous sections of this chapter, to expand the software. Once testing started, there was a reasonable period of error-parsing, after which it became evident that manual adjustment to put the pipette in contact with the cell was needed for almost every approach. This posed a much bigger problem for quad patching than in the previous single version. Waiting to apply pressure to seal once the pipette is in contact with the cell decreases seal yield rates. Therefore, the user would need to manually position the first pipette, press seal, wait for it to finish (so as not to disturb the sealing), move the next pipette, press seal, etc. Thus, if a manual adjustment is required for all four manipulators, that would require a lot of time, resulting in a semi-automated procedure, which would not be favourable and not as helpful. Hence, we decided that manual adjustment was unacceptable for the quad version.

We initially tried an algorithm where the pipettes would hunt for the cell in the surroundings of its assumed position once the approach was completed. Once they reached the target coordinates, the pipettes would first go down in the z direction while measuring impedance. If the

cell was not found, it would move +5 μm in the positive x direction and repeat the hunt down in z. It would then repeat the search in a position -5 μm in x direction, and both +5 μm and -5 μm in the y direction. Anything further than 5 μm would have not been advisable, as the pipettes could collide with each other due to target proximity. Unfortunately, this algorithm did not work, as the movement of the pipettes around the cell caused damage and in most cases, resulted in low success rates. Therefore, it became clear that targeting optimization was our top priority.

As previously mentioned, there are several factors that can impact the accuracy and precision of the targeting portion of the algorithm, namely: (1) the incorrect calculation of the centre-of-mass coordinates of the target by the imaging algorithm, (2) inaccuracy by the user when acquiring the pipette tips, (3) improper calibration of the angles of the manipulator, (4) the inherent drift and/or accumulative error in the manipulator movements, (5) the improper calculation of the movements the manipulator needs to make, possibly due to a floating-point digital number limit that is bigger than anticipated.

(1) Incorrect calculation of the centre-of-mass coordinates of the target by the imaging algorithm.

The algorithm developed by Annecchino et al. (2017) requires the user to initially select the target, which provides the program with the starting coordinates in all three axes; z coordinates come directly from the objective position, while x/y coordinates come from the imaging algorithm that analyzes the FOV, finds the COM of the selected object and adds/subtracts the distance from the centre of the FOV (i.e. the objective's position) to find the universal x/y coordinates of the target. Subsequently, as the pipette is inserted in the brain in a step-wise manner, the target might migrate downwards, due to the deformation of the brain. While the x/y coordinates of the target are continuously updated, the z coordinates of the target, however, will not change unless the target ceases to be in the FOV, at which point a step downwards in z with the objective is taken. If the target is found, the algorithm continues with the approach of the pipette, while if the target is still not visible, a 3D stack of 30 μm in depth around the target will be acquired to re-locate the target position. This approach carries two problems: (1) the z coordinates of the target are inadequate most of the time, which means that it is extremely likely that the pipette will make its final approach targeted towards the very top surface of the cell, rather than its centre, decreasing the likelihood of success. (2) The 3D stack,

taken when the pipette is under the objective and close to the cell, is a perilous manoeuvre, as it will most likely push on the pipette, which will in turn push on the brain, possibly altering the final position of the pipette tip and cell. Therefore, to decrease the likelihood of the objective pushing on (any of) the pipettes, the stack was reduced to 20 μm in depth and made mandatory before the final approach movements, in the hope that the position of the target would be more precise. While the reduction in the depth of the stack helped, it also created a new problem, where the characteristic bell shape of the CFS values was now incomplete and thus, the Gaussian filter applied was failing to find the actual peaks. Therefore, instead of a Gaussian filter, the algorithm was adapted to instead find peaks through the native 'Find Peak' VI, on the preprocessed data (spline fit applied to the raw data). Once this was implemented, it was successfully checked that the cells were indeed in the coordinates determined by the algorithm. However, the targeting was still failing, requiring manual positioning, and hence other sources of error had to be considered.

(2) Inaccuracy by the user when acquiring the pipette tips.

As will be explained in the next section, the concentration of Alexa 594 Hydrazyde in the internal solution was significantly reduced, which makes it harder to acquire (select within the FOV) the pipette tips, because the characteristic diffusion shape as the dye leaves the tip (seen in Fig. 4.15) has a fainter fluorescent signal. The solution taken to tackle this problem was to significantly increase laser power during pipette acquisition. Usually, power is limited by the possibility of photobleaching the cells or generating too much heat (which is detrimental for the cells), but this is not a problem when only the pipettes are in the FOV. The heat generated could potentially degrade the contents of the internal solution, but usually the process of acquiring the tips only takes a few seconds. Furthermore, we observed no seal success decrease after we implemented this, so we do not think this is a concern. Furthermore, experience greatly improves accuracy, as the user becomes more used to recognizing the shape of the pipette tip when it is in perfect focus (Fig. 4.15).

(3) Improper calibration of angles of the manipulator and (4) The inherent drift and/or accumulative error in the manipulator(s) movements.

It was observed in the first trials that the amount of diffused (red) Alexa 594 Hydrazyde through all four pipette tips and the decreased signal coming from the (green) FURA 2-AM bath-loaded sample (as compared to transgenic GFP samples), deemed a fluorescent footprint

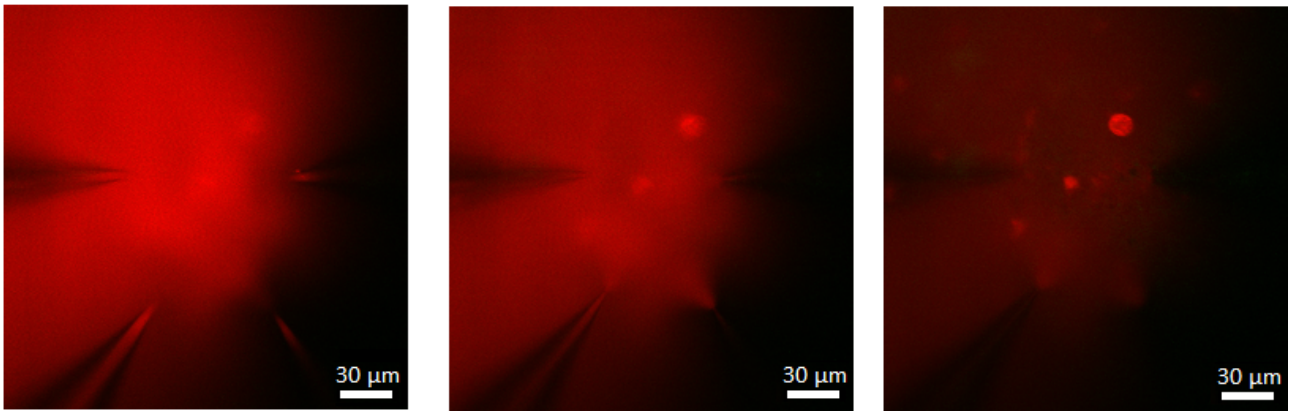


Figure 4.15: View of the four pipettes under two-photon microscopy at different focus planes. (Left) View of the four pipettes under two-photon microscopy with the objective slightly too high on the z direction, so that the shaft rather than the tip of the pipettes are in focus. (Middle) Pipette tips in perfect focus. (Right) Pipette tips not in focus again but with the objective being too low in the z direction in this case.

.

mainly saturated by the red channel. Thus, it was decided that it would be optimal to decrease the percentage of Alexa in the internal solution, from the common 10 mM (0.4 μL of dye to 200 μL of internal), to 1mM (0.1 μL to 500 μL), which was the minimum concentration possible given the internal solution aliquots and available pipettes in the laboratory. This solved this problem but accentuated a different one: while it was always very hard to distinguish the end of the pipette tip once it was in the brain, it was now practically impossible.

This translates to not being able to determine the position where the pipette tip ended up with respect to the target cell. Therefore, to solve this problem, the infrared (IR) imaging was fed to RITA as a different channel, to be able to acquire the coordinates of both the pipette tips and target cells. However, to be able to discard the possibility of the target cells moving from their 3D-stack acquired positions due to pipette movement, we needed to be able to compare the IR coordinates to the ones determined by the algorithm. For this, I translated the IR coordinates into the 2P/objective/universal coordinates used throughout RITA. The 2P coordinates have their origin at the centre of the FOV, while the IR has its origin at the top left corner of its FOV, which does not match the FOV in 2P. Therefore, an ad-hoc coordinate translation was required. Once this was done, the final position of the cells with respect to their 3D-stack coordinates could be calculated, as well as the distance between them and the pipette tips.

If (3) was the only issue, a clear trend should be visible in the targeting approaches. An

overestimation on the elevation angle would give slightly high approaches on the z with the x and y being on the path to the cell but not yet there. An overestimation or underestimation on the azimuth angle would not affect z but affect x and y in a consistent manner (e.g. Manipulator 1 would always have an excess in the x coordinates, manipulator 2 a deficit on y coordinates, etc). Since this was not directly observed (Fig. 4.16), it was assumed that the issue must lie in (4) or elsewhere.

The question was posed, however, that if the issue at hand was manipulator precision in itself like was theorized by the author of Annecchino et al. (2017), it should be expected that the Sensapex manipulator would perform better, as per their claimed increased precision, but this was not the case (Fig. 4.16).

Testing was done, therefore, to assess the severity of the drift in the manipulators. It was found, however, that this was not an issue, as the drift in all manipulators was 5 μm in 2 hours. Given that most approaches are minutes in length, and that (in the final version of the algorithm) pipettes are acquired before approaches, it does not seem like this would be an important contributor to the inadequate targeting.

Finally, I theorized that the problem must lie in error accumulation along the many movements that the manipulators were doing, as they were approaching the cells in a step-wise fashion to avoid excessive tissue deformation (and losing track of the cells). To test this theory, a very simple algorithm was designed, by which RITA would take a 20μm-in-depth 3D stack to obtain target coordinates and then would command the manipulators to approach the cells in two single yet measured movements: one movement to align the manipulators to their axial approach axes and another along said axes towards the cell. The comparison of the previous iterative method and this one can be seen in Fig. 4.16, where it is obvious that targeting was greatly optimized with this change. It was observed, however, that the remaining distance between the pipette tips and target cells followed a very clear trend, indicating slight maladjustment in the manipulator angle calibrations (as can be seen in Figure 4.17). The trials in Fig. 4.17 were performed in an agarose gel of similar consistency to the brain and 10 μm fluorescent red beads as mock cells. From these trials it was also concluded that the Sensapex manipulator often failed to move at all when commanded. In such cases, the distance between the target and tip was too large to plot in the same graph as the other data points, and hence they were omitted from the plot. We realised that the Sensapex manipulator would fail more often when more than a day had

elapsed since its calibration. Hence, from that point in time forward, the Sensapex manipulator was calibrated at the beginning of each experiment day, which improved its performance.

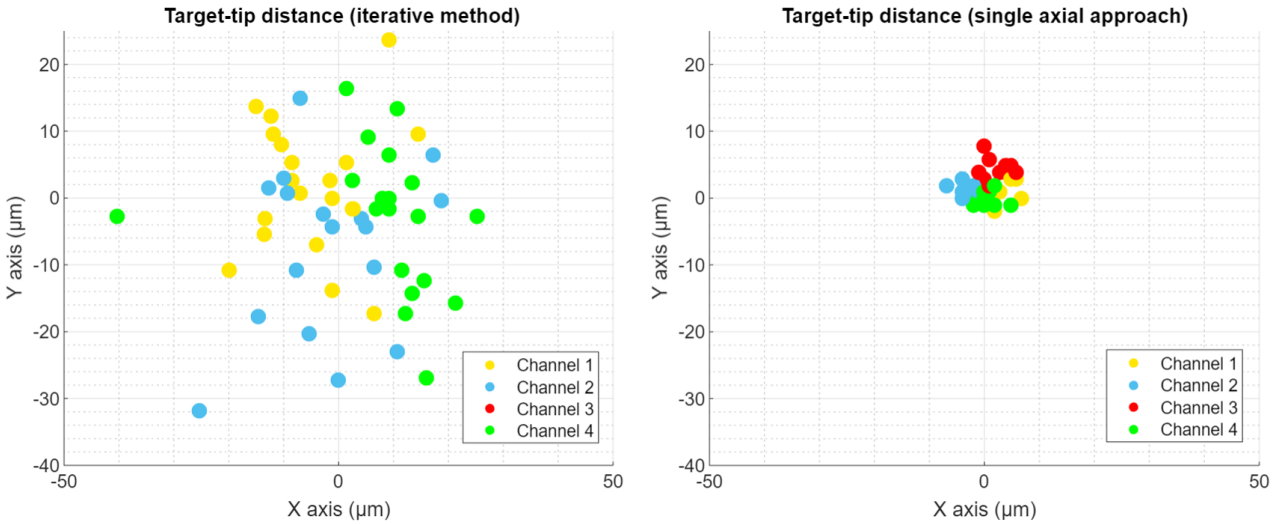


Figure 4.16: Iterative vs. single axial approach target to tip distance (targeting optimization results). (Left) Plot in 2D of the distances between the target and the tip for three of the four channels, showing averages in slightly darker colours, for approaches made with the iterative method used in Annecchino et al. (2017) but adapted to four channels. (Right) Plot in 2D of the distances between the target and the tip for each of the four channels, showing averages in slightly darker colours, for approaches made with the final algorithm: one movement to align the manipulator to the axial axis, and another to move it to the target cell. The differences in accuracy are obvious. The z coordinates don't show such as stark difference but also point to better targeting with the non-iterating method, with data points being contained within [15,-20] of the z axis for the iterative method and mostly within [-11 10] for the non-iterative method. Red channel was not presented on the iterative method because it had extremely high y coordinates, which likely arose from an error in acquisition.

.

Once the slight maladjustment in the manipulator angle calibrations were fixed, the manipulators started consistently driving the pipette tips to their target cells.

Therefore, it was concluded that if (5) had an effect whatsoever, it was negligible.

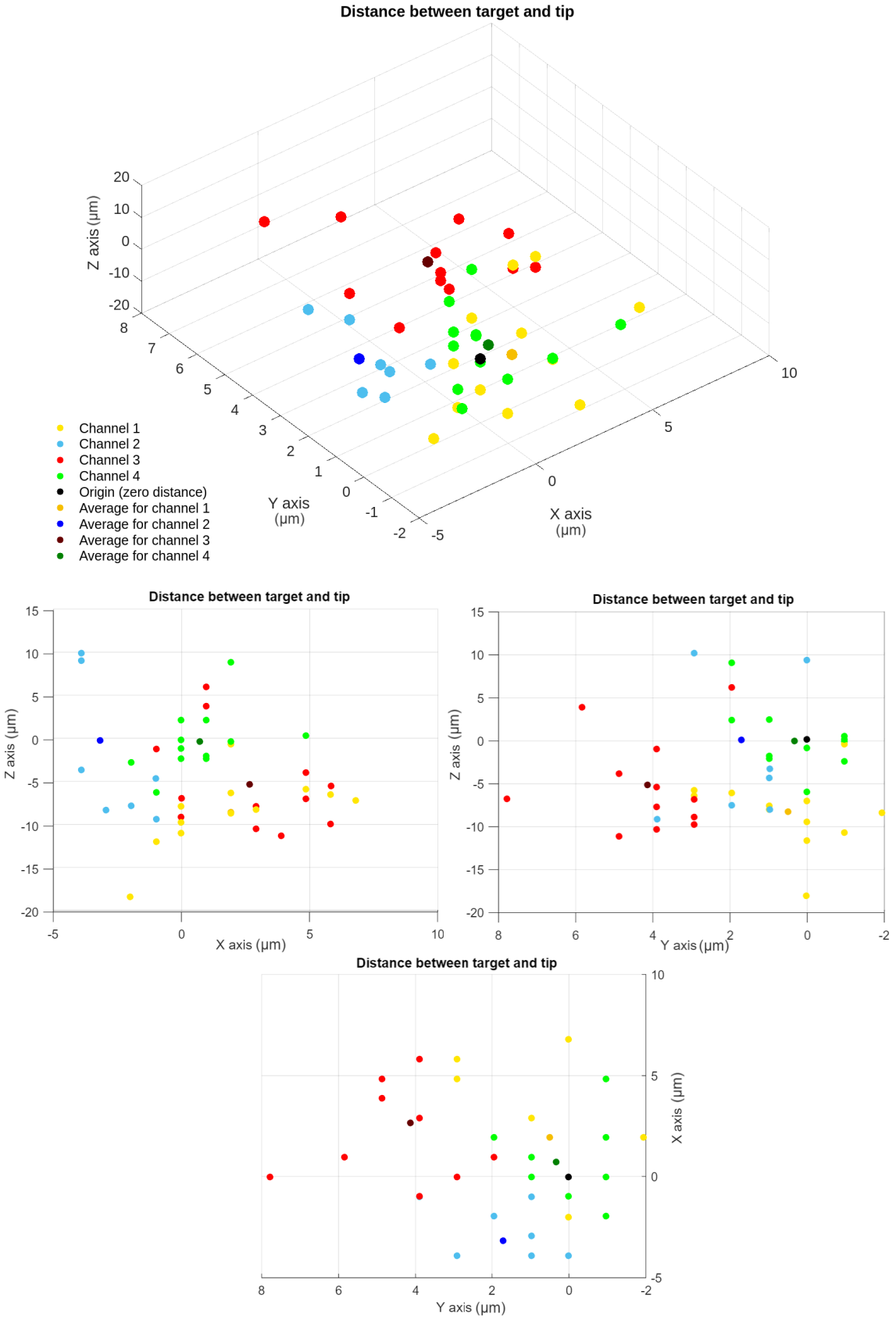


Figure 4.17: Single axial approach algorithm results (distance between target and tip) before final calibration, during targeting optimization. (Top) Plot in 3D of the distances between the target and the tip for each of the four channels, showing averages in slightly darker colors and the origin (zero distance) in black. (Middle) Same plot in 2D for x and z axis (left) and z and y axis (right). (Bottom) Same plot in 2D for x and y.

.

4.3.10 Follow manipulator function

Thanks to RITA, there are few actions required from the experimenter, mainly selecting pipette tips and targets. However, the first attempt requires the experimenter to place the pipettes inside the field of view and to lower them to the brain surface, whereas later attempts only require moving the pipettes to the new field of view where the new targets are. This is due to the fact that it is recommended to change regions after each attempt, as the brain in the region where the old attempt took place has already been altered by the penetration of the four pipettes. In either case, there are options to do it automatically, but the experimenter might prefer to do it manually, especially lateral movements that might lead to pipettes colliding into each other and possibly breaking them. If so, the follow function allows the experimenter to activate this option and move a single pipette. RITA will calculate the differential position change made and apply the same movement to the other pipettes.

4.3.11 Pipette self-cleaning for reuse

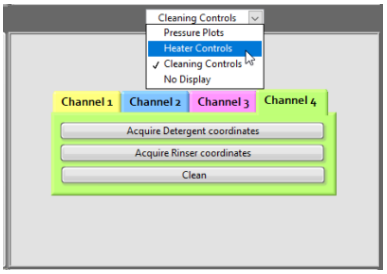


Figure 4.18: Cleaning commands. Only three buttons are needed per channel: two to store the coordinates of the detergent and rinsing solutions and one to activate the VI. This is one of the tabs that can nest different modules together (in such a way that only one can run at a time) to save CPU usage as described in section 4.3.6. Rinsing the pipettes after detergent cleaning is not needed according to literature (Peng et al., 2019) and we in fact do not have wells in the chamber for a rinsing solution, but the command is left in the module for those who wish to have it.

Pipette cleaning was first developed by Kolb et al. (2016). It allows patch-clamp experimenters to avoid filling and replacing pipettes after each attempt, a tedious but necessary task. Instead, pipettes are introduced in a bath filled with a detergent and, through pressure pulses, the detergent is flushed in and out of the tip of the pipette, until no cell or protein remains can be found. Afterwards, the detergent is flushed out and the pipette is ready to be reused. This

automation is possible thanks to pressure systems such as the ones described in section 1.3.5 and it can increase the throughput of patch-clamp experiments, whether they are done manually or in an automated fashion. Alconox was used in Kolb et al. (2016) but later substituted by Tergazyme (Alconox Inc) in Peng et al. (2019) and Landry et al. (2021), as the first had a 10 re-use limit that the latter did not. The key resides in the fact that Tergazyme has an extra enzyme, a protease called Subtilisin Carlsberg, that helps in the removal of proteins stuck to the pipette tip, that Alconox lacked. Tergazyme cleaning was proven to have no effect on patch-clamp success over 31 attempts (Landry et al., 2021). It is recommended to prepare the Tergazyme solution fresh everyday, as we noticed a decrease in yield when the same solution was used for long.

The detergent to clean the pipettes needs to be within the manipulators' movement range, which implies the necessity of a bath chamber that is close enough to the sample chamber (for the manipulators to reach) but far enough so that both solutions do not mix. Given the already difficult geometries of inserting four manipulators onto the sample chamber, this was not a straightforward task but after a few design iterations, I settled to the one depicted in figure 4.19. It was printed in semi translucent resin from a SOLIDWORKS design.

For complete automation, saved xy coordinates of the cleaning bath positions is not enough, as evaporation of the cleaning liquid must be taken into consideration. Luckily, the sudden change in the current signal that happens when a pipette comes in contact with liquid can be used to detect the correct z coordinates (once the pipette is at the xy coordinates of the well), to then start the cleaning pressure pulses (Kolb et al., 2016).

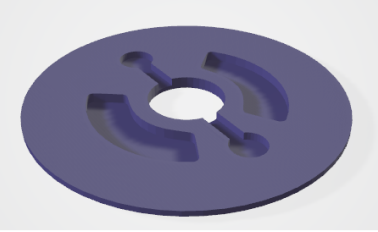


Figure 4.19: CAD design for the sample chamber, which contains a cleaning well on each side. The center hole corresponds to the sample chamber where the brain slice lies, with grooves for the inlet and outlet of the perfusion system. Each Tergazyme well is used by the two manipulators on the corresponding side.

4.3.12 Manufacturing of the pressure system

Given that only one pressure system was used in Annecchino et al. (2017), at least three more were needed. A technical drawing of the pneumatic part of the pressure system was provided, but it was proven not to be completely accurate. Hence, I made a SOLIDWORKS model of the pressure system, which was then used by the Mechanical Engineering Workshop technician to reproduce it several times. The electric part of the pressure system was refined and translated onto a Printed Circuit Board that could be industrially manufactured. This was done by Phatsimo Kgwarae. Besides the four systems, another standalone pressure system was manufactured to send to Prof. Jesper Sjöström's laboratory for them to test and provide feedback. I created a MATLAB program to control the pressure system, as this is more commonly used than LabView. Further descriptions of this standalone pressure system can be found on Appendix A.

4.4 RITA's internal architecture

Figure 4.20 shows the structure of the main VI in RITA. It contains the 11 VIs that are in charge of all the modules in the GUI (depicted in Figure 4.5). On the top left is the Sciscan VI (in purple), on the right of it (after the time delay) is the Subpanel control VI (10). Within the elongated structure, the remaining 9 VIs can be observed: (1) Autopatcher, (2) Signal Acquisition, (3) Manipulator Daemon, (4) Autotargeting/Multiautoengage, (5) Amplifier control, (6) Pressure control, (7) Scope daemon, (8) Targeting Unit and (9) Visual Analyzer. A Daemon is a type of program that executes on the back end without user control.

1. Autopatcher VI (1) deals with the autopatching module of the GUI (bottom left module in Fig. 4.5). It therefore contains each of the subVIs that are activated when each of the buttons in that section are clicked on, with the exception of the visually guided VIs. These VIs are:

    1.1. Load: simple VI to set the right pressure while the capillaries are inserted in the electrode holders.

    1.2. Localization: the VI that gets the channel ready for either hunting ('blind' patch) or targeting (targeted patch). It offsets the electrophysiology signals, sets the holding

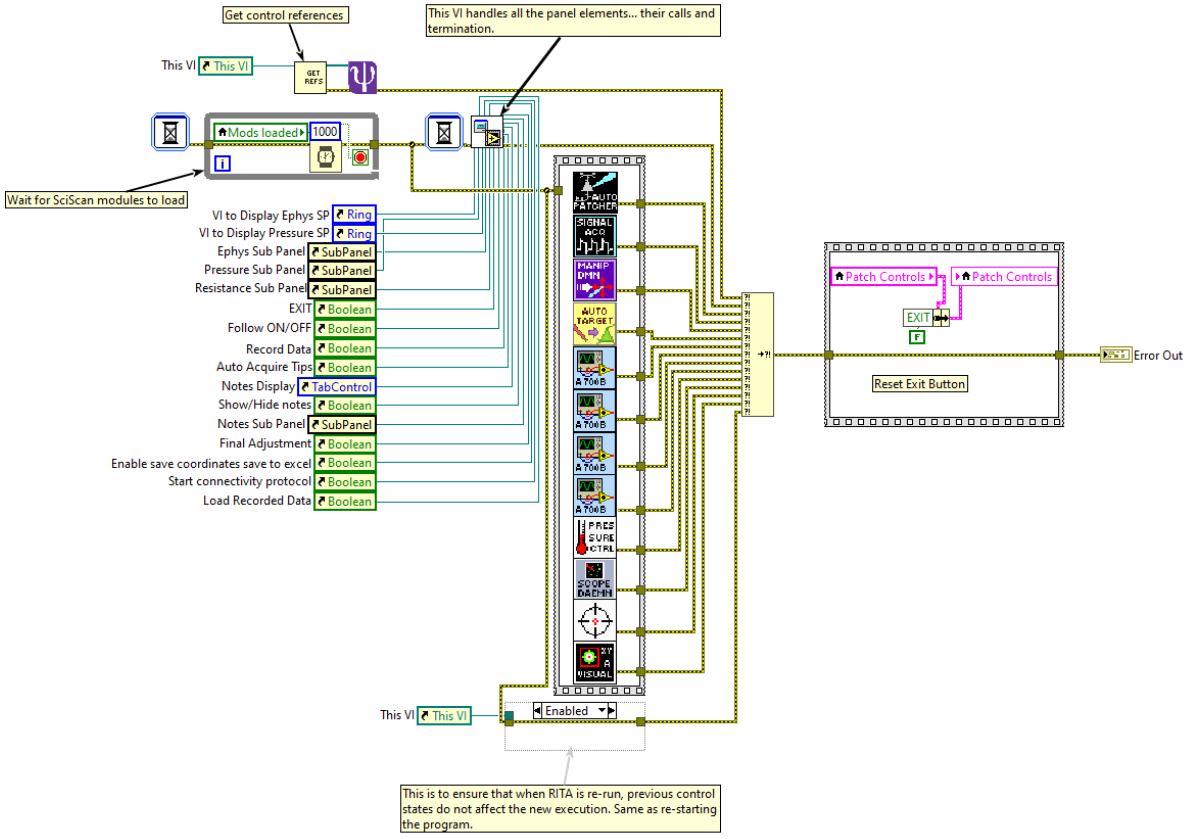


Figure 4.20: Structure of the main VI showing the dynamic calling and loading of VIs. It calls the 11 VIs in charge of all the modules in the GUI, as well as a VI for SciScan integration and another for controlling the GUI's subpanels. All variables are contained within a structure not shown in the picture but accessible to any VI or subVI.

potential to 0mV, activates the step signal used to calculate impedance and sets the pressure to +5kPa.

1.3. Hunt: the VI in charge of 'blind' patching. It detects changes in impedance that go above a certain threshold. Each channel can have its own threshold, albeit most of them are set to the same level. This is mainly because the pressure system and tubing length (dependant among their position on the setup) and thus PID values, are specific to each channel, and therefore the applied pressure is never exactly the same for all, which in turn means that the impedance levels are not equal for all. Once a cell is detected, the state of the channel is changed to 'Seal', while the rest of the manipulators that haven't found a cell are paused until the seal is either successful or a failure. This VI is the only one that remains almost the same from Luca Annecchino's (LA's) system in Autopatcher. The rest of them have been programmed from anew, with the exception of Break-in, that has been expanded

from LA's version. LA's version was modified to pause the rest of the channels when a cell in detected.

1.4. Seal: The VI in charge of sealing. It first releases the positive pressure and then applies trains of individual pulses of negative pressure, with each train having an increased pressure when compared to the previous. When the resistance rises above the gigaohm threshold, suction stops and the state is changed to maintain seal. For more information on the suction algorithm, see Appendix A. It was redesigned from LA's program to resemble the suction pattern applied by experienced patch-clamp researchers.

1.5. Maintain seal: The VI that monitors the impedance of a sealed cell to make sure it does not fall below the gigaohm threshold. If it does, it analyses the signal to ascertain if it is because the cell was broken into spontaneously or because the seal was lost or is being lost. In the latter case, it applies suction to try to recover the seal. If it fails, the user is alerted.

1.6. Break-in: The VI in charge of breaking in. It applies suction pulses of increasing strength, until the cell is broken into or the maximum negative pressure is applied, at which point it is considered a failure. A sudden decrease can both mean that the cell has been broken into from the seal configuration or that the seal has been lost, but the difference is obvious by looking at the current signal. Hence, we implemented a quick check on the signal to determine which of the two cases has happened. We also implemented some electrical zapping to the cell in the last round of suction, as a last resort to make the cell break-in if suction alone has not worked.

Autopatcher has a rather active role in the functioning of these VIs, in the sense that if automatic mode is on, it is in charge of (1) checking that all channels (that are active and not aborted) are set to hunt before any of them actually starts, (2) monitoring the entrance of a channel into the seal state (due to an increase in the impedance) at which point the other channels are paused, (3) detecting when all channels have had a seal attempt (as they will all be in either maintain seal or failed), (4) when this happens, changing the states of the channels that are in maintain seal state into break-in mode. If the automatic mode is not on, the VI is passive and just waits for the user to press the buttons instead of automatically initiating the next step. This VI has the barebones of

the program that Luca Annecchino (LA) designed, but is much more advanced to perform all of the roles previously mentioned.

2. Signal acquisition VI (2), as the name indicates, takes care of acquiring the electrophysiology signals (voltage and current) from the DAQs and plots them, calculating the impedance values and plotting them. The sampling frequency is 20kHz for the signals and all values are plotted but the plotting of the impedance is calculated every 100 values, with a frequency of 10Hz. This VI has been expanded from LA's version.

3. Manipulator daemon (3) takes care of all the commands relating to the movement of the manipulators. This includes changing between axial and z approaches, stopping all movement, taking a step in either axial of z direction, driving to a certain z, moving to certain coordinates, changing the speed, and closing the VI when Exit button is pressed (as can be seen in Fig. 4.21, where a loop constantly checks if one of those buttons have been pressed to carry out the action). It has a case structure that determines if the channel/clone (see section 4.3.2) corresponds to a Scientifica or Sensapex manipulator, to use the respective subVIs (see section 4.3.3). Furthermore, the lower loop in the Fig. 4.21 shows how the position of the manipulator, its state (idle or moving), the approach it is using (axial or z) and its angle are queried and updated on the manipulator module display in the GUI.

4. Multiautoengage VI (4) is currently disabled because it is computationally expensive and not in use. It is the algorithm that was developed by Luca Annecchino for the *in vivo*, targeted, single, automated patching, but updated to work with four channels. After target and tip acquisition, the pipettes move in small steps towards the target while the targets are closely monitored and their coordinates constantly reacquired to account for breathing, cardiac and tissue deformation movements. This algorithm required a manual adjustment at the end of the approach, to put in contact the tip and the target, that were in close proximity but not in contact. While this algorithm worked for a single channel, a manual adjustment in four channels made it impractical, as explained in section 4.3.9. It has not been erased, however, because parts of it may prove useful for the *in vivo* quad automation of the platform.

5. Multiclamp 700 (5) is the VI in charge of communicating with the Multiclamp 700B commander, and can perform all of the functions of MultiClamp 700B commander. See

section 4.3.4 for more information.

6. Pressure control VI (6), as the name indicates, takes care of controlling the pressure systems. It turns the pressure on and off, sets the desired pressure target, sends pressure pulses and changes the pressure controller dynamics, all by sending the commands on a string format serially to arduino through a VISA (see section 4.3.3).

7. Scope Analyzer (7) is in charge of scope movements: moving to specific user-determined coordinates, zero the coordinates, checking the size of the FOV for coordinate translation, centering the tips or targets in the field of view, changing between IR and 2P imaging, and so on.

8. Targeting Unit VI (8) contains the VIs that are related to imaging but not the actual image analysis. It receives its name because it is in charge of making sure that the coordinates of the targets within the FOV are updated (it contains a loop that runs every time the image frame is updated, where the visual center of mass coordinates of the cell are used to update the coordinates that are used as the target for the tip movement). It also contains the VIs in charge of the manipulator calibrations, the VIs activated when the tip and target are acquired, as well as the centering of the tips and targets in the FOV.

9. Visual analyzer VI (9) is in charge of analysing the images from the microscope to detect particles above a certain size and of a certain shape, among which the user can choose the targets. It also handles the switching between IR and 2P image feeds. The CFS of all particles is obtained and the targets tracked frame-to-frame within this VI.

10. Subpanel control VI (10) contains the event detection for the newest additions to RITA, like follow manip, experimental notes, record, connectivity protocol,etc. It also contains Acquire final target coordinates VI, which is the algorithm used for the targeted approach. It takes a 3D stack of the cells to determine the plane where they are most in focus by using the CFS. The center of mass coordinates of each cell in their most-in-focus plane are used as target, where the pipettes move in two movements, the first one an aligning movement to the axial approach axis, and the second along this axis towards the cell. Then the sealing status is activated and the seal VI takes over.

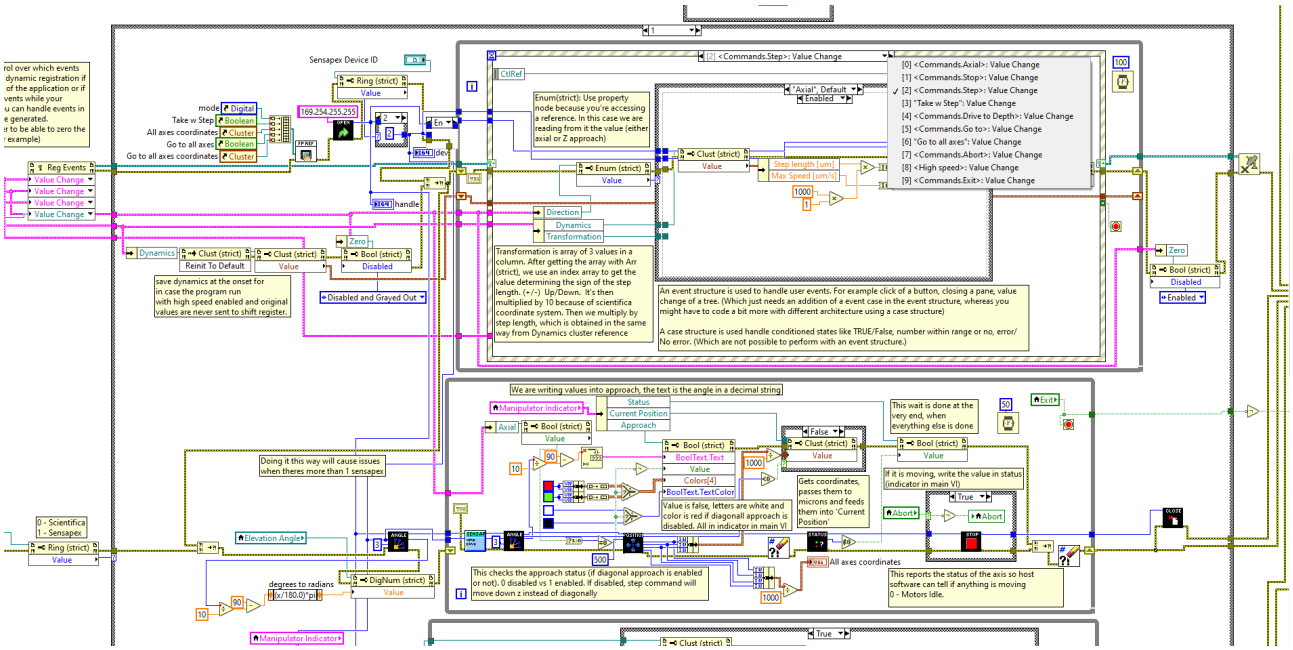


Figure 4.21: Structure of the Manipulator Daemon VI. The VI initiates communication with the manipulator, then runs a while loop that listens for and executes various commands, such as 'take step', 'change speed' and 'go to coordinates'. Another while loop, which runs in parallel, queries the current manipulator coordinates to keep them constantly updated.

Chapter 5

Ex vivo results and validation for 'blind' multi-patching

The technology developed in this thesis allows automated quad-channel patch-clamp for *ex vivo* brain slice electrophysiology, capable of both 'blind' and two-photon targeted robotically automated patching. This chapter covers the results for the 'blind' mode of the platform, starting with examples of dual, triple and quadruple successful 'blind' recordings, and finishing with the general statistics of all the trials.

The robot scales up the patch clamp single cell recording technique to four simultaneous channels, with seal success rates for 'blind' mode of 68%. This success rate was calculated as (successful seals in all pipettes)/(total number of trials in all pipettes). Most 'blind' trials yielded triple or quadruple recordings.

This robot, a milestone on the path to a true *in vivo* robotic multi-patching technology platform that allows both 'blind' and targeted patching, will allow numerous studies into the function and connectivity patterns of both primary and secondary cell types. Particularly, the 'blind' mode will probably not allow connectivity studies (as explained in the introduction), but can nevertheless help relieve the experimental load of the experimenter and improve throughput.

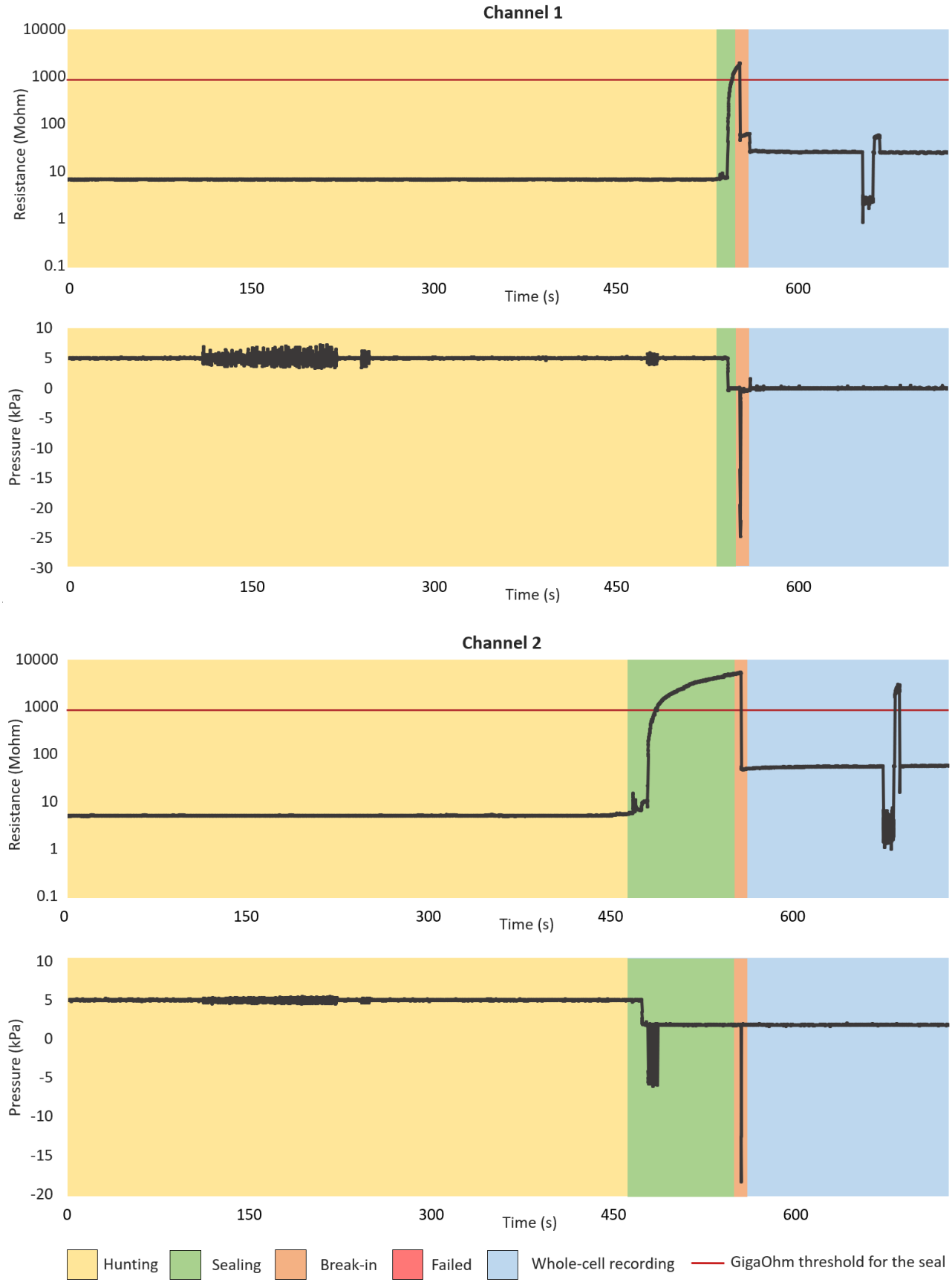
5.1 Example of a pair of successfully patched cells

Example traces of the resistance and pressure signals (along time) for all four channels can be seen in Fig. 5.1. Channels 1, 2 and 3 managed to seal and break in successfully but not Channel 4. The input resistances for channels 1, 2 and 3 respectively were 27.25, 60.40, and 99.0 MΩ, the series resistances were 8.25, 45.13 and 29.85 MΩ while the resting membrane potentials were -50.13, -60.87 and -44.71 mV.

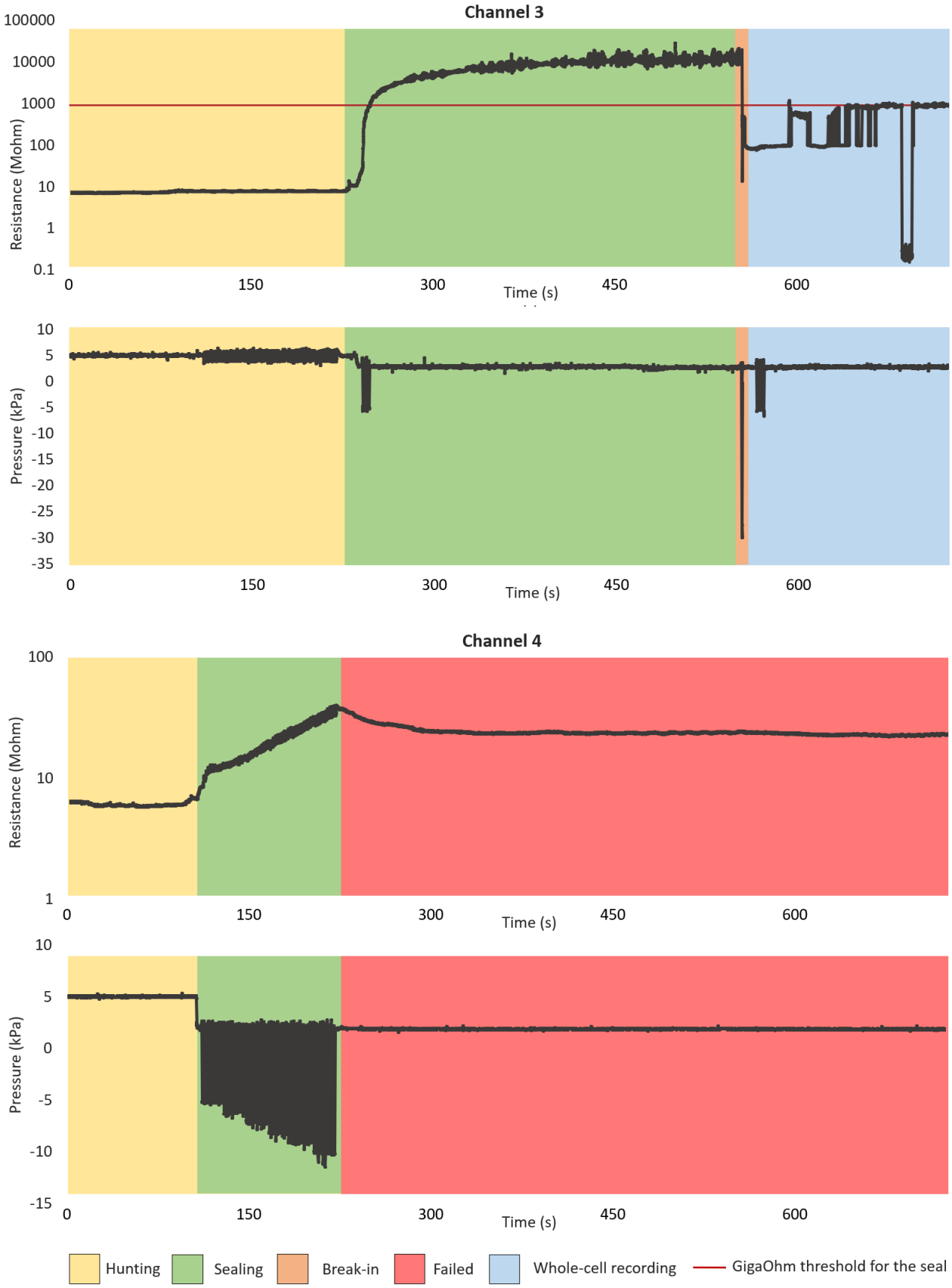
Contrary to targeted slices, the sealing in the four channels is not coordinated in 'blind' approaches, and each channel seals whenever a cell is encountered, while break-in is coordinated for all the channels that have not failed. The cell in Channel 3 was unfortunately lost before injections could be run, likely due to the fact that the sealed cell had to wait longer for break-in, to coordinate with the other channels (that took longer to find a cell).

All channels start hunting for a cell (yellow stage). The positive pressure (+5 KPa) is released and sealing (green stage) started whenever a channel detects a cell. Negative pressure is applied if necessary during the sealing process. More negative suction pulses are applied during the synchronized break-in (orange stage) in all the active channels (channel 4, which failed to seal, becomes inactive, red stage). Once break-in is achieved, this is detected by RITA, which switches to WCR mode (blue stage). In the hunting stage (yellow) of Channels 1,2 and 3, some ripples can be seen in the pressure signal, around the 150 second mark. These are caused by the strong suction pulses applied in Channel 4. They arose from unintended coupling of the pressure systems of the four channels, because they share the same high pressure inlet. This has been partially fixed since this recording was taken, and we are actively working on completely decoupling them.

The 'square' dips in resistance seen in the Whole-cell recording (WCR) stage in all channels arise from the acquisition of the resting membrane potential, because it is measured in the 'I=0' mode of Multiclamp (neither current nor voltage clamp, simply measuring the voltage with no current injection), which stops the voltage step of the voltage clamp mode used during the sealing and break-in process to measure resistance. At the point in time that these recordings were obtained, the acquisition of these parameters was not automatic, but rather manual, so every time the experimenter checked on the health of the cell (i.e. membrane potential), a square dip will be seen. Furthermore, unhealthy cells that spike very frequently can give rise



(a) Stages of the automated process and corresponding pipette resistance and pressure changes for channels 1 and 2.



(b) Stages of the automated process and corresponding pipette resistance and pressure changes for channels 3 and 4.

Figure 5.1: Stages of the automated multi patch-clamp process (color legend at the bottom) and corresponding pipette resistance and pressure changes in a 'blind' trial along time.

to unusually high resistance values, as seen on the cell of channel 3.

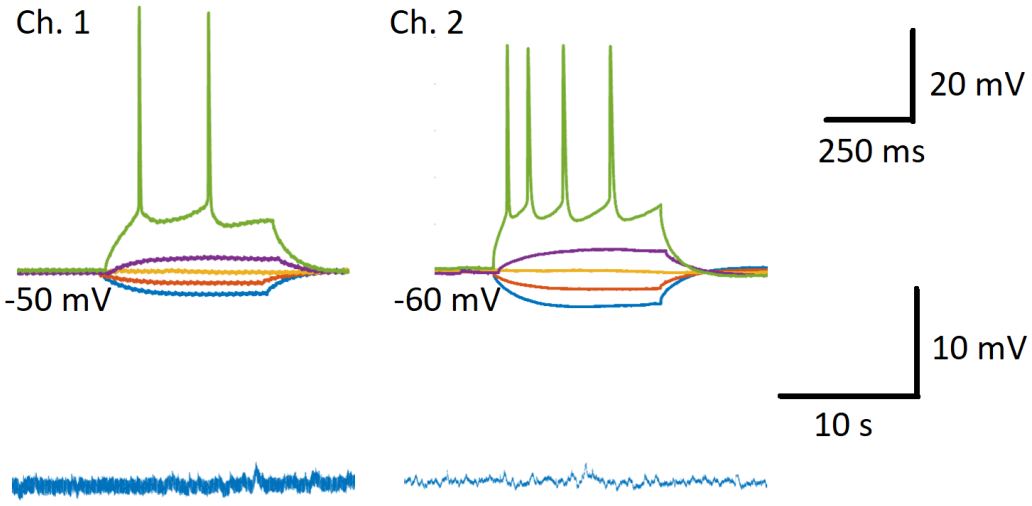


Figure 5.2: Characterization of two cells patched in 'blind' mode. (Top) Example of the responses of two cells patched in 'blind' mode to the current pulses applied through our injection protocol module. Voltage responses to injections of -40, -20, 0, 20 and 100 pA are presented, but the protocol injects current steps from -100 to 280 pA in increasing steps of 20 pA. All current steps are 500ms in length. (Bottom) Recordings of the same cells with no injections.

Fig. 5.2 presents the current injections that the program ran on the two remaining cells. No connections were found between these cells (unsurprisingly, as during blind hunting, pipettes rarely end up close to one another). Channel 1 has a high-frequency noise that we had not noticed before the analysis of this data, that is also present in other recordings presented in this chapter. Looking towards *in vivo* mode, we will work to erase any possible source of noise in the rig (or grounding problems) to avoid this noise from coming up again in any other recording, as it could affect the detection of subthreshold phenomena in connectivity studies.

5.2 Example of three successfully patched cells

Fig. 5.3 presents the characterising current injections that the program ran on three cells that were patched in the 'blind' mode.

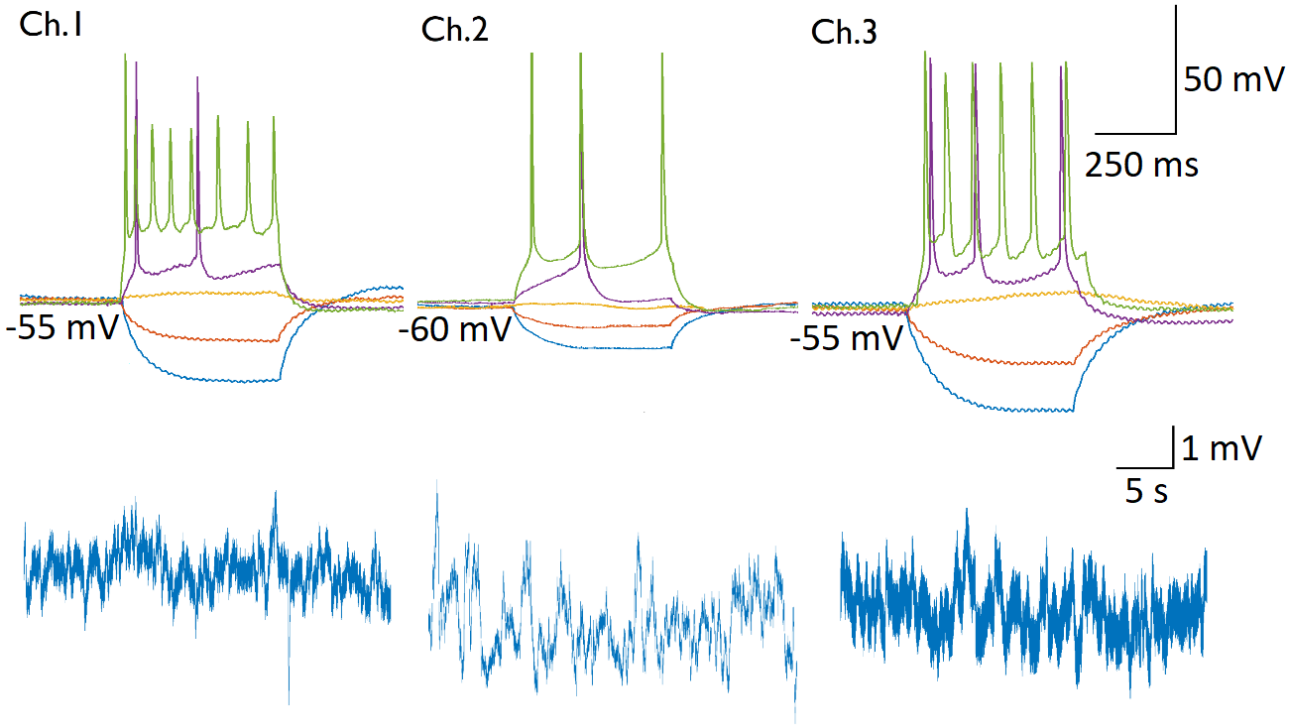


Figure 5.3: Characterization of three cells patched in 'blind' mode. (Top) Example of the responses of three cells patched in 'blind' mode to the current pulses applied through our injection protocol module. Voltage responses to injections of -40, -20, 0, 20 and 60 pA are presented. (Bottom) Recordings of the same cells with no injections.

5.3 Example of four successfully patched cells

Fig. 5.4 presents the characterising current injections that the program ran on four cells that were patched in the 'blind' mode.

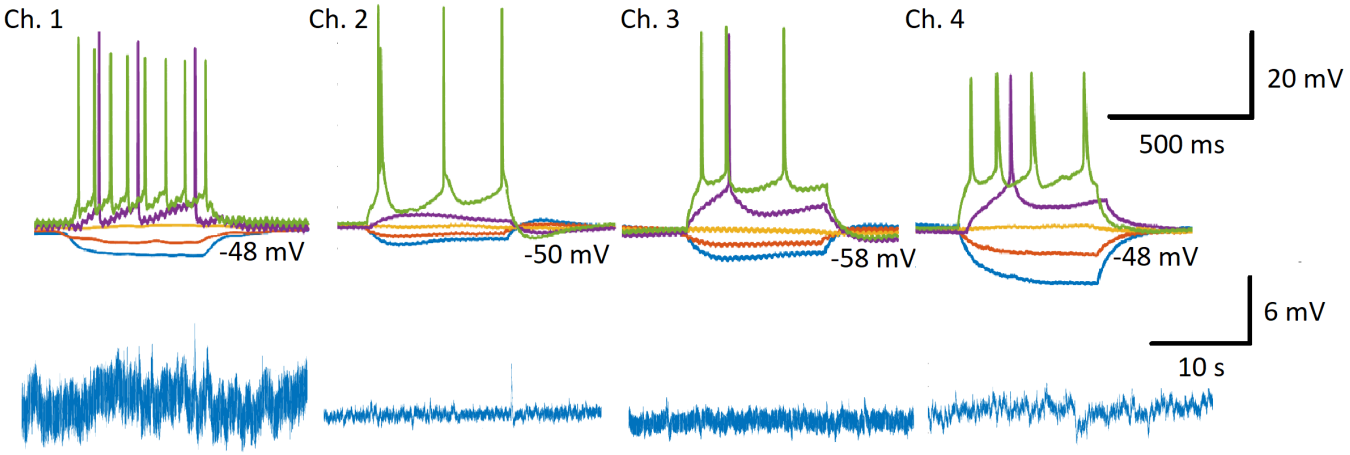


Figure 5.4: Characterization of four cells patched in 'blind' mode. (Top) Example of the responses of four cells patched in 'blind' mode to the current pulses applied through our injection protocol module. Voltage responses to injections of -40, -20, 0, 20 and 60 pA are presented. (Bottom) Recordings of the same cells with no injections.

The input resistances for channels 1, 2, 3 and 4 respectively were 69.06, 36.27, 51.43, and 99.71 MΩ, the series resistances were 7.52, 20.33, 24.72 and 20.67 MΩ while the resting membrane potentials were -48.04, -49.82, -57.85 and -48.34 mV.

5.4 Statistics

For 'blind' mode patching in brain slices, we achieved a 68.3 % seal success rate (Fig. 5.5) and a 62.2% break-in success rate, from a total number of pipettes of n=82, arising from 14 quad trials, 8 triple trials and 1 double trial (initially a triple trial where a channel had to be aborted due to malfunction of the Sensapex manipulator). All these trials came from n=7 mice. Interestingly, depending on the day (and thus the slice quality), we saw exceedingly different success rates. For example, one day the success rate was as low as 53% (n=17, 5 triple trials, 1 double trial) but on anoher, as high as 82% (n=19, 4 quadruple trials, 1 triple trial). This tells us that RITA is capable of exceedingly good success rates if provided with high quality brain

slices. This hypothesis is also in agreement with the work by Perin and Markram (2013), which presents a bimodal model for their results, claiming that user experience and slice preparation can shift success rate from anywhere between 30 and 90% (Perin and Markram, 2013).

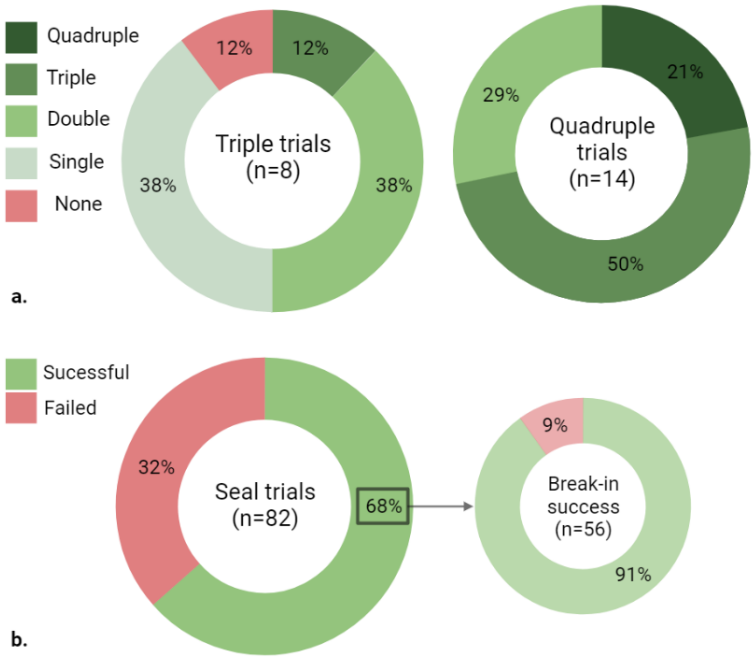


Figure 5.5: 'Blind' patch success rate in brain slices. (a) Proportion of single, double, triple and quadruple simultaneous patches obtained in trials with three pipettes (left) and four (right). (b) Proportion of successful seals in the 14 quadruple and 8 triple trials (total of 82 pipettes). Break-in success percentage.

It is also interesting to note from Fig. 5.5 that the percentage of successful seals per number of channels does not necessarily scale. While the mean number of seals for 4 channels is 2.93, the mean for 3 channels is 1.5, nearly half. It is possible that this is due to the fact that when 4 channels are used, the deformation that they each create individually is slightly counteracted by the others, due to the symmetric geometry in which the four channels enter into the tissue (Fig. 3.2). In the future, this theory could be tested by doing individual, dual, triple and quadruple trials and comparing their targeting yield (target to tip distance). It would also be interesting to test dual trials in different configurations (perfectly symmetric versus both coming from the same side) to see the effect on the targeting yield.

Fig. 5.6 presents the resting membrane potential, input and series resistance of the cells patched with RITA in 'blind' mode. Some input resistance data points had to be excluded from the plot and statistics due to their exceedingly high values, which arose as an artefact from RITA measuring the resistance during a spiking event of the cell. To circumvent this problem we

have now implemented in RITA the automatic recording and storage of the electrophysiology signals during the first few minutes of WCR, to make sure that if the resistance is not properly measured by RITA, the experimenter has a signal to analyze and extract the real value from. The experimenter also has the option to do the same at the end of the recording, to check that the series resistance has not increased.

Pipette resistances and input resistances are calculated by dividing the voltage signal sent to stimulate the cell by the measured current signal, whereas series resistance is obtained from the corresponding section of MultiClamp commander. The resistance used to assess if a gigaseal is achieved is the input resistance. A break-in was considered successful by the low input and series resistance (below 100 MΩ, but with three outliers between 100 and 200 MΩ), as well as the distinctive shape on the signal. The signal of a cell that has been broken into has a capacitive/exponential shape, as compared to a lost seal, which would look like a square signal (see Fig. 1.2 for further information). There are four outliers in the resting membrane potential that are above -40 mV, which would not be considered successful in manual patching (like the rest would). These were likely due to unhealthy cells which, during the two minutes that RITA waits to automatically measure the cell characteristics, declined in health with increasingly higher resting membrane potential. In general we looked at cells when they had just broken into, and if they were healthy cells at that point (fulfilling the parameters described above), it was considered a successful seal, regardless of their later state.

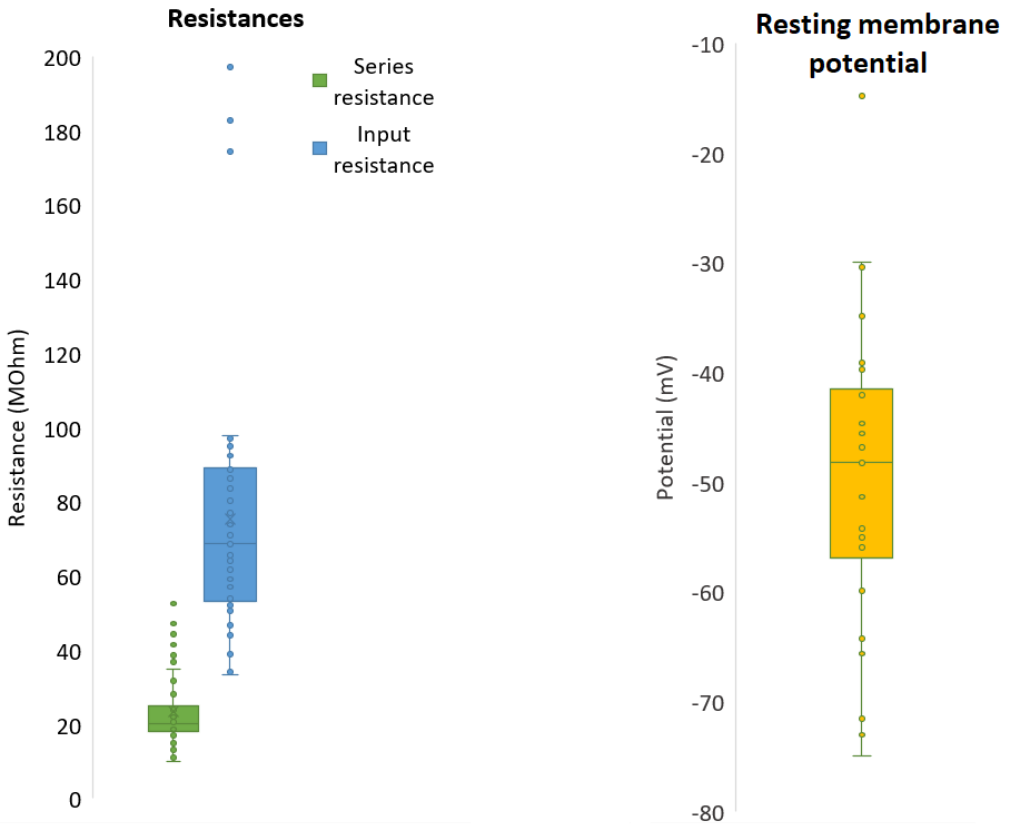


Figure 5.6: Resting membrane potential, input and series resistance distribution of the cells patched by RITA in 'blind' mode. All data points are represented by circles. The lower and upper limits of the box plot are the first and third quartiles, respectively, while the central line is the median of the data. Outliers are presented outside of the box. (Left) Input and series resistance distribution of the cells patched by RITA in 'blind' mode. (Right) Resting membrane potential distribution of the cells patched by RITA.

5.5 Conclusion

Owing to the promising statistics, our robot will make quad patch-clamping accessible to laboratories all over the world that do not have access to an experienced instructor and/or the time and money to train someone. Additionally, it could help experienced patch-clamp researchers in their studies, either by using the pressure module to avoid mouth suction where there may be health safety concerns, or by saving their time in numerous ways: automatically recording data, synchronised movement of pipettes, automated cleaning of pipettes for reuse, etc. It will thus make thousands of new neuroscience studies possible and more efficient.

Chapter 6

Ex vivo results and validation for two-photon targeted multi-patching

The technology developed in this thesis allows automated quad-channel patch-clamp for *ex vivo* brain slice electrophysiology, capable of both 'blind' and two-photon targeted robotically automated patching. This chapter covers the results for the two-photon targeted mode of the platform, starting with examples of dual, triple and quadruple successful recordings, and finishing with the general statistics of all the trials.

The robot developed during this PhD scales up the patch clamp single cell recording technique to four simultaneous channels, with seal success rates for two-photon targeted mode of 54%. This seal success rate was calculated as (successful seals in all pipettes)/(total number of trials in all pipettes). In 50% of targeted trials (where specific cells were required), at least 2 simultaneous recordings were obtained. This robot, a milestone on the path to a true *in vivo* robotic multi-patching technology platform, will allow numerous studies into the function and connectivity patterns of both primary and secondary cell types.

6.1 FURA 2-AM loaded slices

6.1.1 Example of a pair of successfully patched cells

Example traces of the resistance and pressure signals (along time) of the successful dual patch seen in Fig. 6.1 are shown in Fig. 6.2.

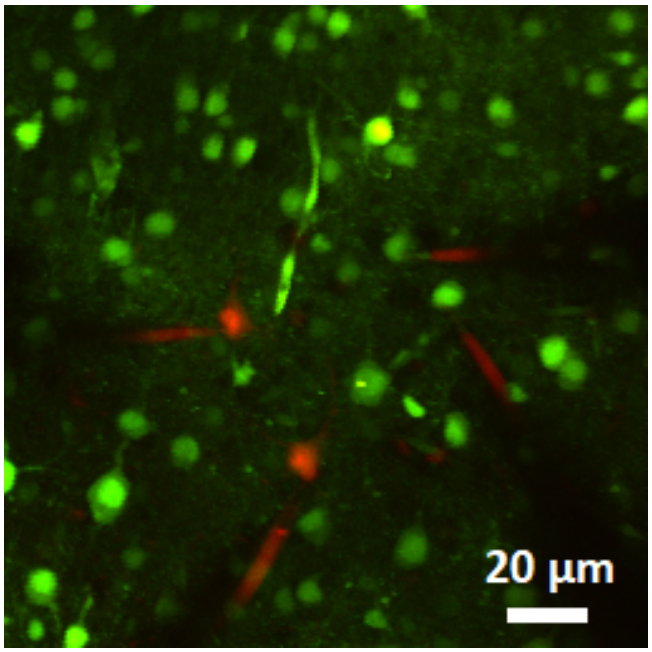


Figure 6.1: A two-photon image of two patched neurons. Cells were bath loaded with FURA 2-AM, a negative calcium dye that becomes trapped inside the cell membrane of living cells, turning them fluorescent (green). Alexa 594 Hydrazyde dye (red) from the pipette internal solution diffuses into the cells as direct contact with their intracellular spaces is established during break-in, making the two patched cells yellow-red (the two cells on the left, from channels 3 and 4), whereas the cells that were not successfully broken into appear as green, and all four pipettes appear exclusively red.

Since the FURA 2-AM data was acquired before the injection and connectivity protocol were developed, no injection data can be presented in this section.

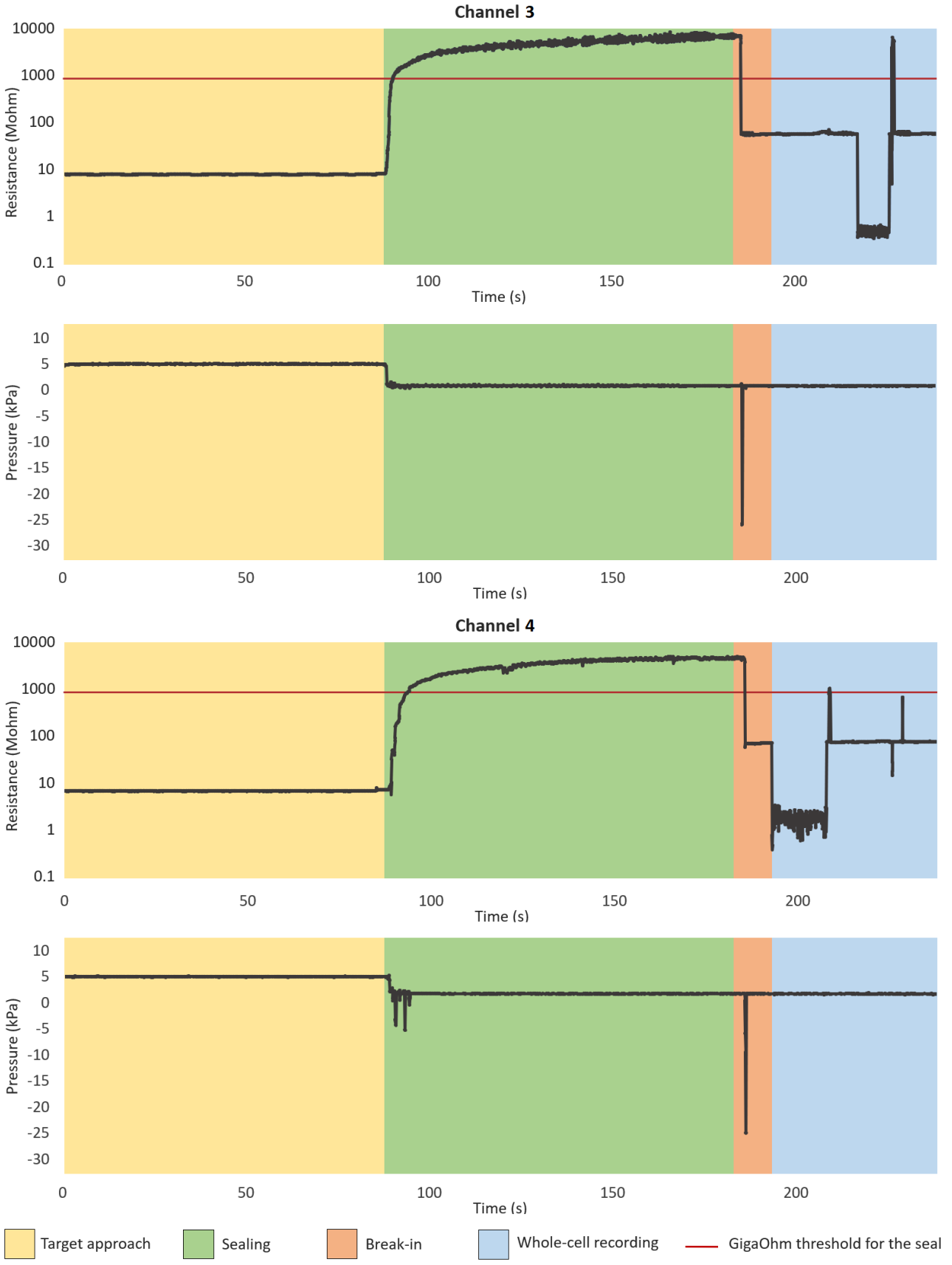


Figure 6.2: Stages of the automated process and corresponding pipette resistance and pressure changes in FURA 2-AM loaded slices for channels 3 and 4. Once the target cell is approached, sealing automatically begins, which releases positive pressure and applies increasing suctions until a gigaseal is formed. Similar, but stronger, suction pulses are applied for break-in.

6.1.2 Example of three successfully patched cells

Example traces of the resistance and pressure signals (along time) of the successful triple patch seen in Fig. 6.3 are shown in Fig. 6.4.

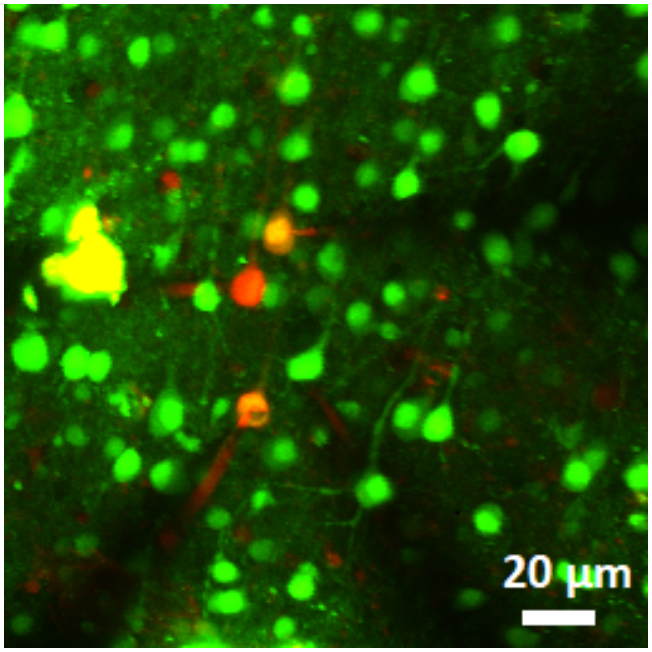
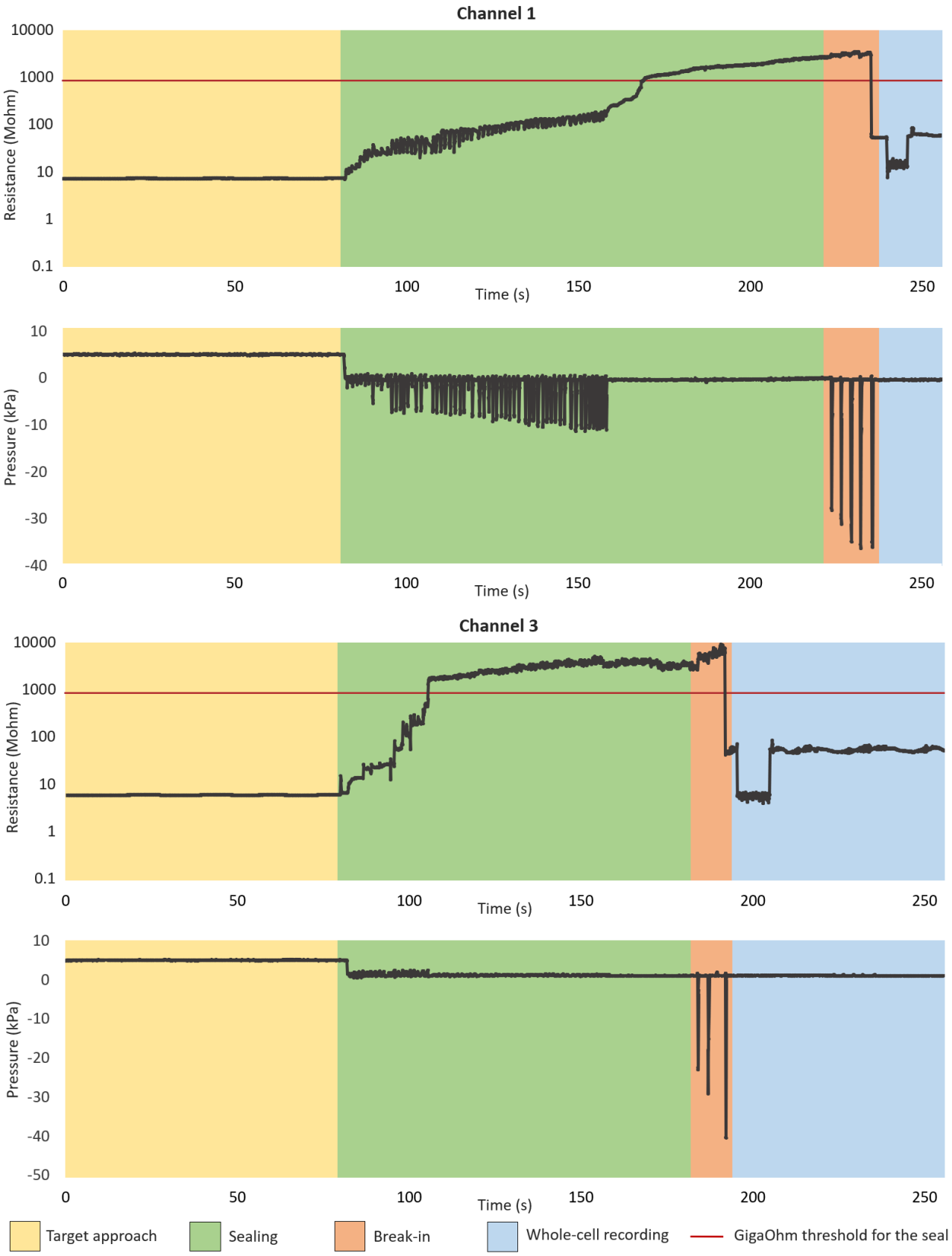
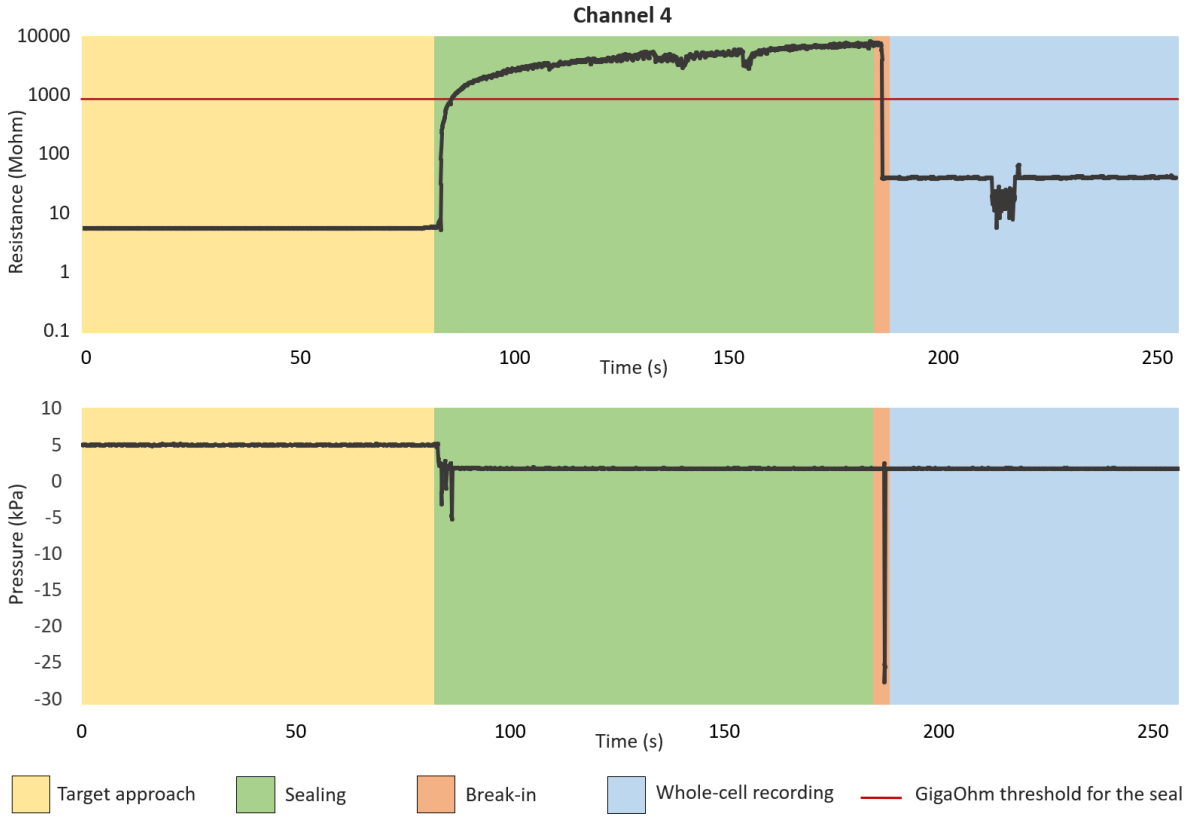


Figure 6.3: A two-photon image of three patched neurons. Cells were bath loaded with FURA 2-AM, a negative calcium dye that becomes trapped inside living cells, turning them fluorescent (green). Alexa 594 Hydrazyde dye (red) from the pipette internal solution diffuses into the cells as direct contact with their intracellular spaces is established during break-in, making the three patched cells yellow-red (the three cells on the left, from channels 1, 3 and 4), whereas the cell that was not successfully broken into appear as green, and all four pipettes appear exclusively red, albeit only the tips can be seen.



(a) Stages of the automated process and corresponding pipette resistance and pressure changes for channels 1 and 3.



(b) Stages of the automated process and corresponding pipette resistance and pressure changes for channel 4.

Figure 6.4: Stages of the automated process and corresponding pipette resistance and pressure changes in FURA 2-AM loaded slices. Once the target cell is approached, sealing automatically begins, which releases positive pressure and applies increasing suctions until a gigaseal is formed. Similar, but stronger, suction pulses are applied for break-in.

6.1.3 Example of four successfully patched cells

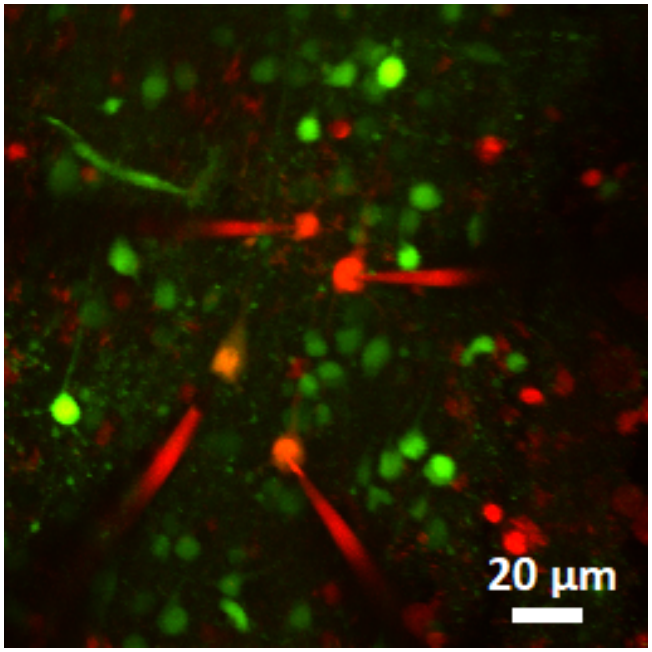
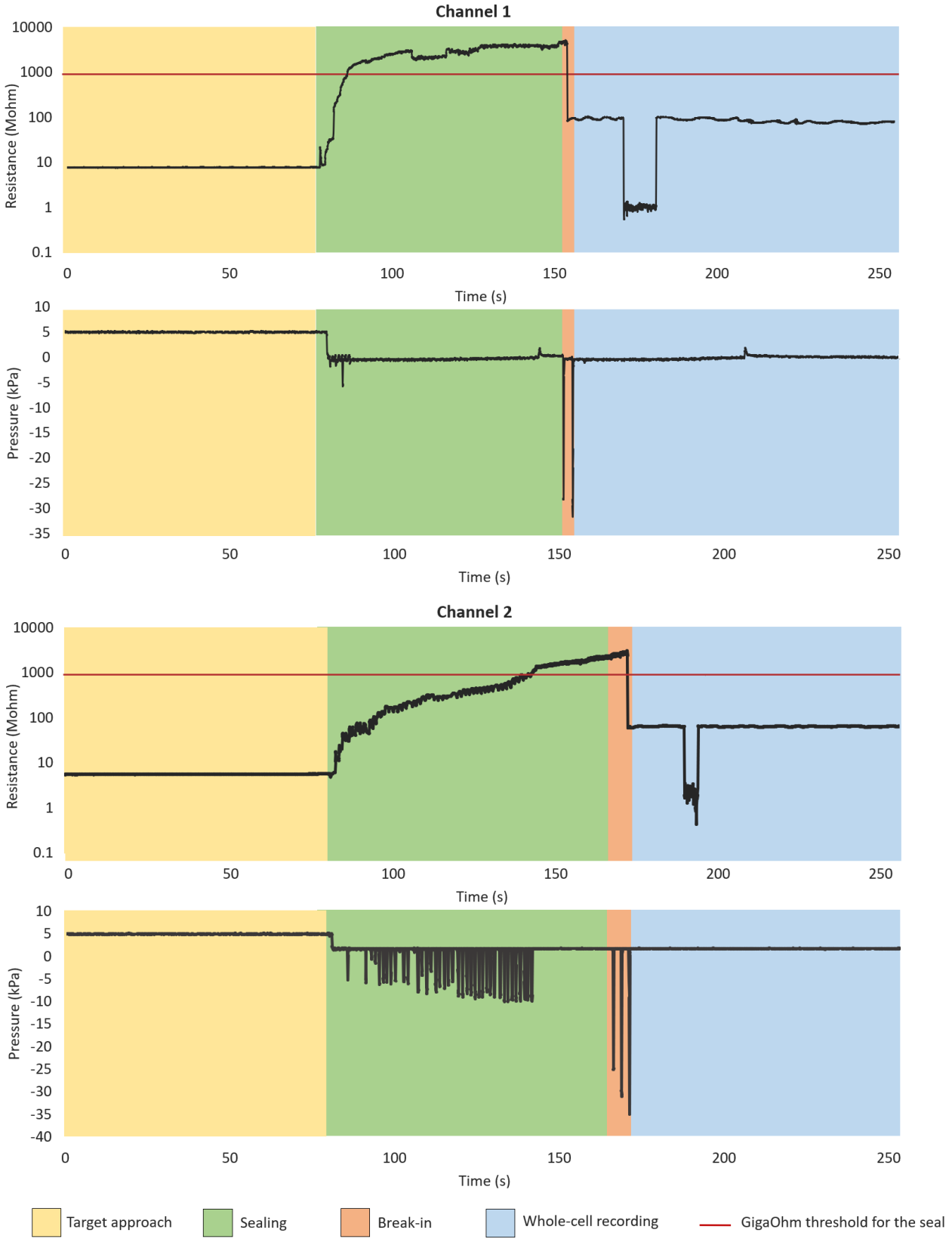
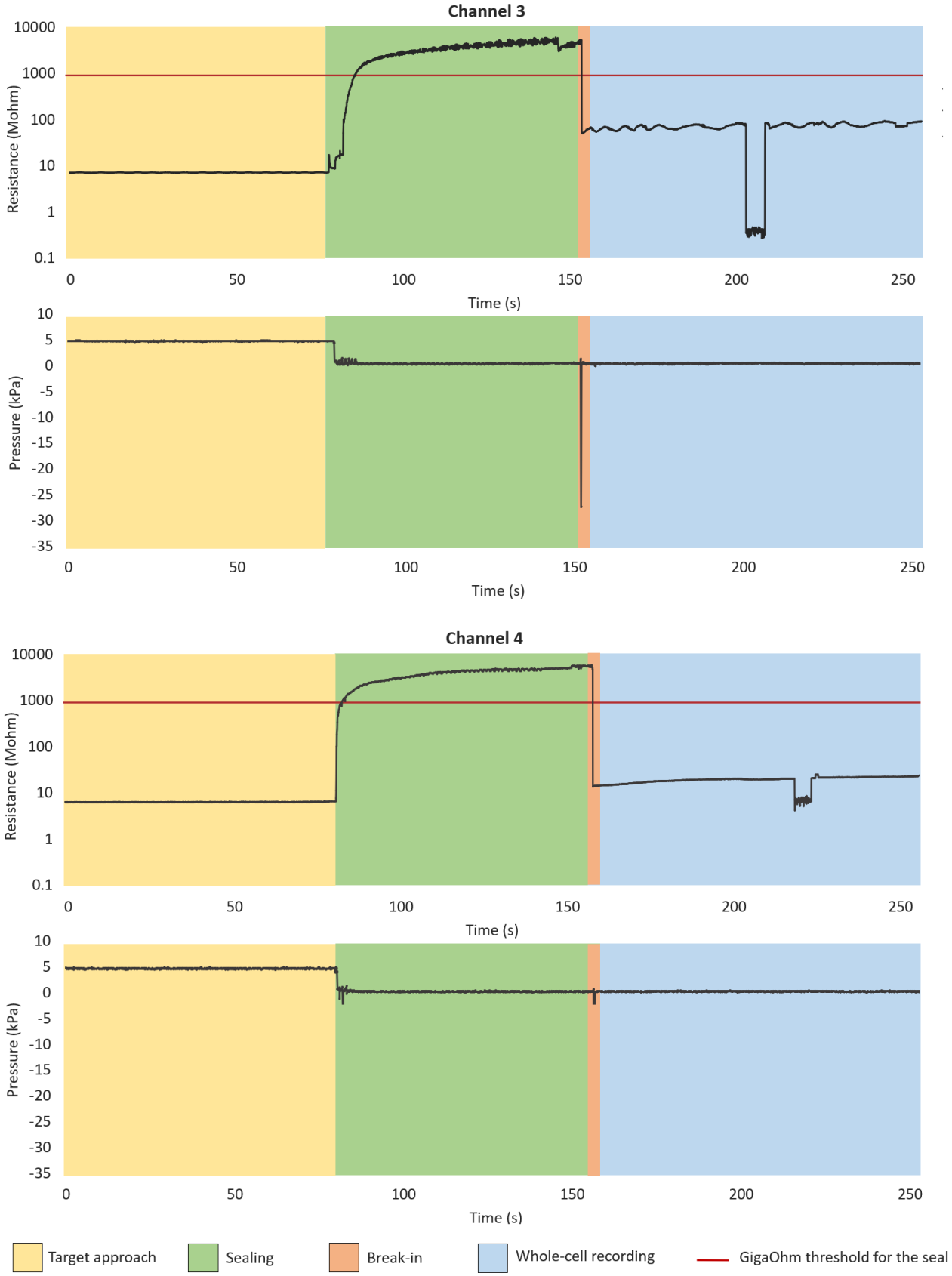


Figure 6.5: A two-photon image of four patched neurons. Cells were bath loaded with FURA 2-AM, a negative calcium dye that becomes trapped inside living cells, turning them fluorescent (green). Alexa 594 Hydrazyde dye (red) from the pipette internal solution diffuses into the cells as direct contact with their intracellular spaces is established during break-in, making the patched cells yellow-red, while the pipettes appear in red. The resistance and pressure plots of these cells can be observed in Fig. 6.6.

Example traces of the resistance and pressure signals of the successful quadruple patch in Fig. 6.5 are shown in Fig. 6.6. All channels start suction to obtain seals at the same time but not all are achieved as fast/easily: while channels 1,3 and 4 practically seal on their own once positive pressure is released (a sign of extremely optimal targeting and healthy cells), channel 2 required persistent suction pulses to achieve the gigaseal, and thus took longer.



(a) Stages of the automated process and corresponding pipette resistance and pressure changes for channels 1 and 2.



(b) Stages of the automated process and corresponding pipette resistance and pressure changes for channels 3 and 4.

Figure 6.6: Stages of the automated process and corresponding pipette resistance and pressure changes in FURA 2-AM loaded slices. Once the target cell is reached, sealing automatically begins, positive pressure is released and increasing suction is applied until a gigaseal is formed. Similar, but stronger, suction pulses are applied for break-in.

6.1.4 Statistics

As a first step towards an *in vivo* two-photon targeted multipatching robot, we developed an *ex vivo* mode, making use of mouse brain slices. We achieved seal success rates of 54.2% (n=48) for targeted (Fig. 6.7). This is in line with the success rates for manual patching but with a much superior speed and thus throughput. An average of less than 4 minutes was needed for all four channels to attempt seal and break-in in targeted mode, with input resistance averaging at around 65.4 ± 4.75 MΩ and series resistance at 24.89 ± 2.41 MΩ. In 50% of trials (Fig. 6.7), we obtained two or more simultaneous patches which could be used for connectivity tests.

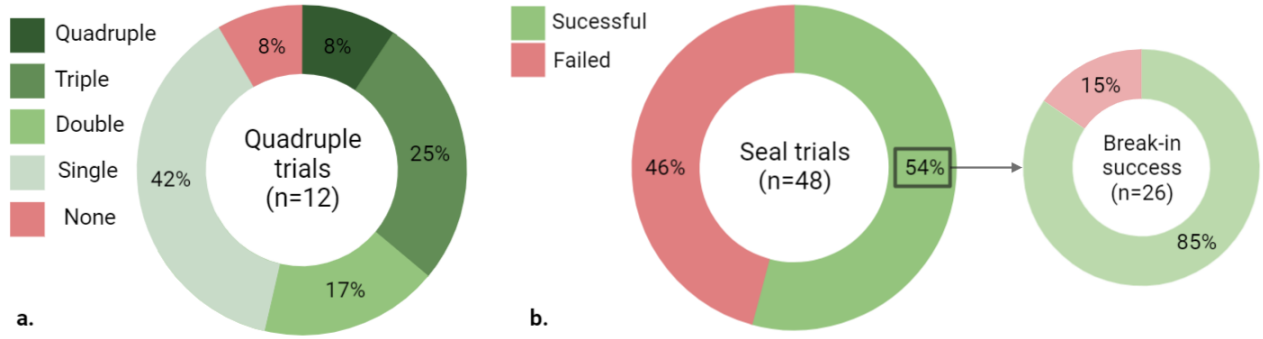


Figure 6.7: Success rates for *ex vivo* trials using dye-loaded (FURA 2-AM) brain slices. (a) Proportion of single, double, triple and quadruple simultaneous patches obtained. (b) Proportion of successful seals in the 12 quadruple trials (total of 48 pipettes). Break-in success percentage for the cells that did seal.

Fig. 6.8 presents the resting membrane potential, input and series resistance of the cells patched with RITA in two-photon targeted mode, as well as the time taken to do so. Pipette resistances and input resistances are calculated by dividing the voltage signal sent to stimulate the cell by the measured current signal, whereas series resistance is obtained from the corresponding section of MultiClamp commander. The resistance used to assess if a gigaseal is achieved is the input resistance. As can be seen, a break-in was considered successful by the low input and series resistance (below 100 MΩ), as well as the distinctive shape on the signal. The signal of a cell that has been broken into has a capacitive/exponential shape, as compared to a lost seal, which would look like a square signal (see Fig. 1.2 for further information). As can be seen in Fig. 6.8, there are four outliers in the resting membrane potential that are above -40 mV, which would not be considered successful in manual patching (like the rest would). These were likely due to unhealthy cells which, during the two minutes that RITA waits to automatically measure the cell characteristics, declined in health with increasingly higher resting membrane

potential. Regarding the time to break-in, RITA is quite regular, usually taking less than 3 minutes to break into all the cells, significantly lower than any manual patch-clamp user. This time is measured from the initiation of the automated process by the user (which is done with the click of a button, after pipette and target have been selected) to the detection by the software of a successful break-in. Most of this time is actually the acquisition of the 3D stack; the time that the pipettes take to penetrate the brain and seal is usually around a minute.

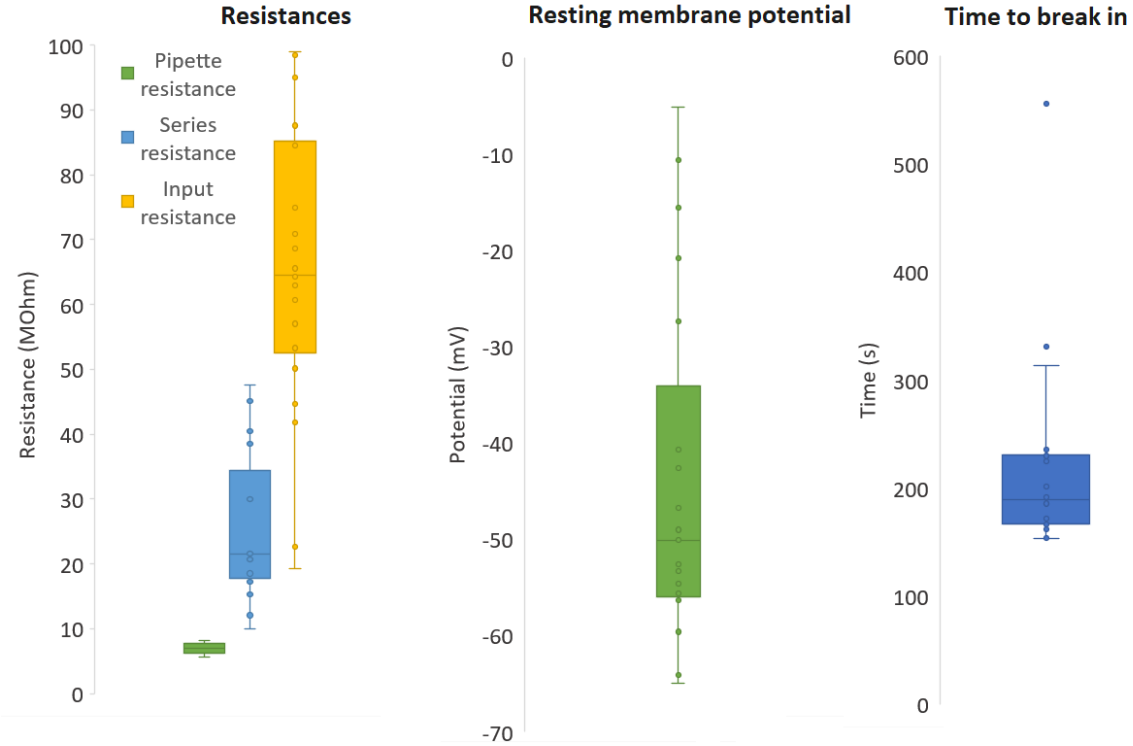


Figure 6.8: Time to break-in, resting membrane potential, input and series resistance distribution of the cells patched by RITA in two-photon targeted mode (FURA 2-AM). All data points are represented by circles. The lower and upper limits of the box plot are the first and third quartiles, respectively, while the central line is the median of the data. Outliers are presented outside of the box. (Left) Pipette, input and series resistance distribution of the cells patched by RITA. (Middle) Resting membrane potential distribution of the cells patched by RITA. (Right) Time taken by RITA to break into the cells.

Our success rates are unfortunately not directly comparable to manual *ex vivo* patching or previous systems, as it is the first of its kind (multi-patch-clamping with a two-photon image guided system). As previously mentioned, IR imaging is the traditional method used in manual patch-clamp because it allows users to see cells dimpling, which is key to obtaining successful seals. On the contrary, dimpling is not seen in two-photon microscopy. Therefore, it would be

expected of IR guided systems and manual users to achieve a higher success rate than a two-photon guided one like ours. It should be noted, however, that our system still performed on par with previous *ex vivo* systems, like the work of Kolb et al. (2019) (43% WCR for subcortical cells and 51% for cortical cells) or Koos et al. (2021)(63.6% WCR for rat, 37% for human), despite these systems being IR-guided and using only one manipulator. They are also slightly superior to the results presented by Wu et al. (2016) (43.2%). Moreover, these systems cannot be expanded to be used *in vivo*, as ours can, due to the limited nature of IR imaging. Our results are also within the success rate range of manual users on IR systems, whose success is highly dependent on experience, falling anywhere between 30 and 80% (Kolb et al., 2019).

6.2 Slices expressing GFP

As previously mentioned in the Methods Chapter (Subsection 2.1.5), during most of the project, I had no access to any animals expressing fluorescent proteins, despite efforts being made. In the last few months, p0 IV injections became a method that we could employ and thus we started testing on slices that were expressing GFP through the CamKII promoter (mainly neurons) in a sparse way. These slices presented better expression than the FURA 2-AM bath loaded slices, as they had a homogeneous expression, not superficial like the FURA slices, and thus did not depend on slice topology (as seen in Fig. 2.3). As expected, the CFS curves (explained in section 4.1) were generally better than with FURA loading, as can be seen in Figure 6.9. This new method allowed us to target deeper cells, which was desirable for two reasons: (1) more superficial cells are likely affected by the slicing process so are generally less healthy, whereas deeper cells are generally healthier and have unaffected axons and dendrites, which is relevant for connectivity studies. (2) It takes us a step closer to a paradigm more similar to *in vivo*. Going deeper, however, has its drawbacks, as the deformation of the tissue is proportional to the depth (Kolb et al., 2019) and thus optimal targeting becomes more complicated.

The algorithm, as developed for FURA loaded slices, seemed indeed to always leave the pipettes more superficial than the plane where the cells were located in GFP slices. This was solved by adding an extra step where the impedance is monitored during insertion and if no cell is detected, the pipette takes up to two steps down (of 8μm) until the cell is detected, at which point suction starts.

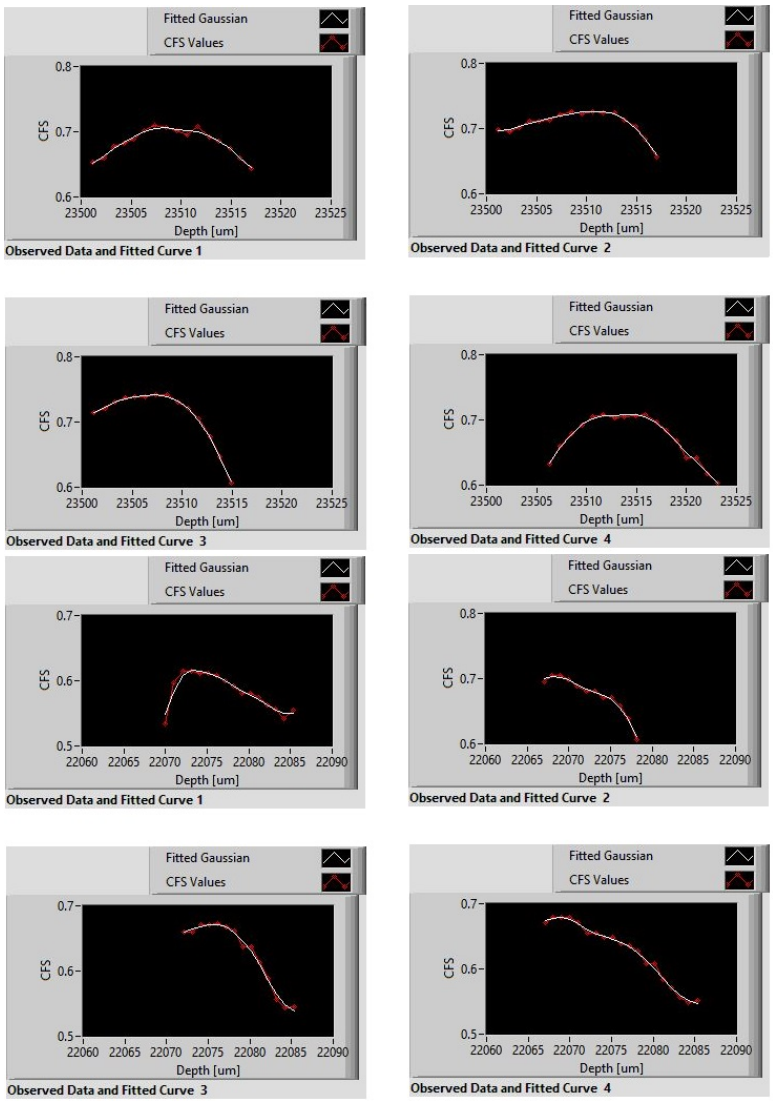


Figure 6.9: CFS curves comparison for FURA 2-AM bath loaded slices and CamKII-GFP p0 injections. (Top left) Example curve for Channel 1 for a trial with four pipettes in slices expressing GFP in cells with the CamKII promoter. (Top right) Same for Channel 2. (Second row) Same for Channels 3 and 4. (Bottom four) Example curves for a trial with four channels in FURA 2-AM bath-loaded slices, for Channels 1,2,3 and 4 from left to right and top to bottom. Contrary to the top four, these curves (maybe with the exception of channel 1) show poor definition for the centre of the cell (semicircular shape), as well as having lower CFS scores in general.

6.2.1 Example of a pair of successfully patched cells

An example of two cells patched with the newest iteration of the algorithm can be seen in Fig. 6.12, together with their pressure and resistance plots. Channels 1 and 3 are not presented because they failed to establish a seal with the targeted cell.

Current injections made into the cells whose sealing and break-in process were presented in Fig. 6.12 can be seen in Figure 6.10. No connections were found between these cells. Pipettes between 5.75 and 6.84 MΩ were used for this approach. The input resistances for channels 2 and 4 respectively were 64.76 and 45.56 MΩ, the series resistances were 13.74 and 20.98 MΩ while the resting membrane potentials were -65 and -72 mV.

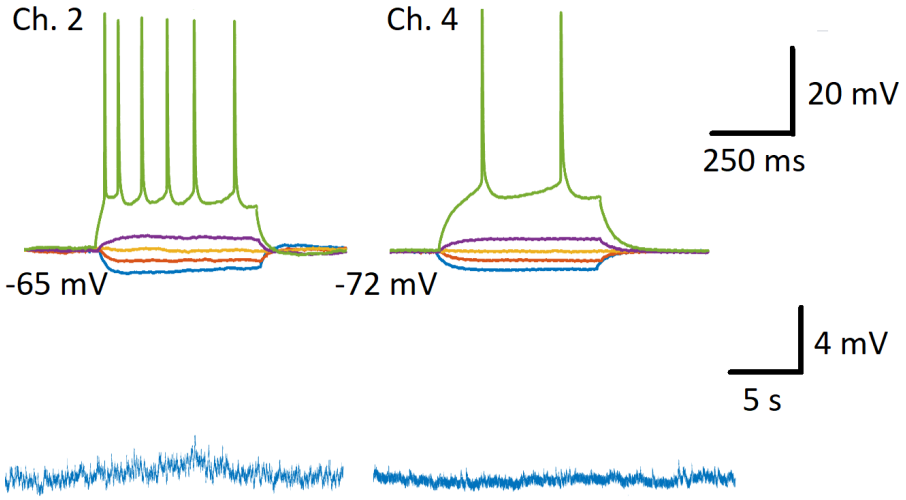


Figure 6.10: Current injections for two two-photon targeted patched cells (expressing GFP owing to CamkII-GFP (AAV9) p0 injections). (Top) Example of the responses of two two-photon targeted patched cells in response to the current pulses applied through our injection protocol module. Voltage responses for the injections of value -40, -20, 0, 20 and 100 pA are presented. (Bottom) Recordings of the same cells with no injections.

Fig. 6.13 shows the potential from two patched cells in layer 5 of the primary visual cortex that did show connectivity between them.

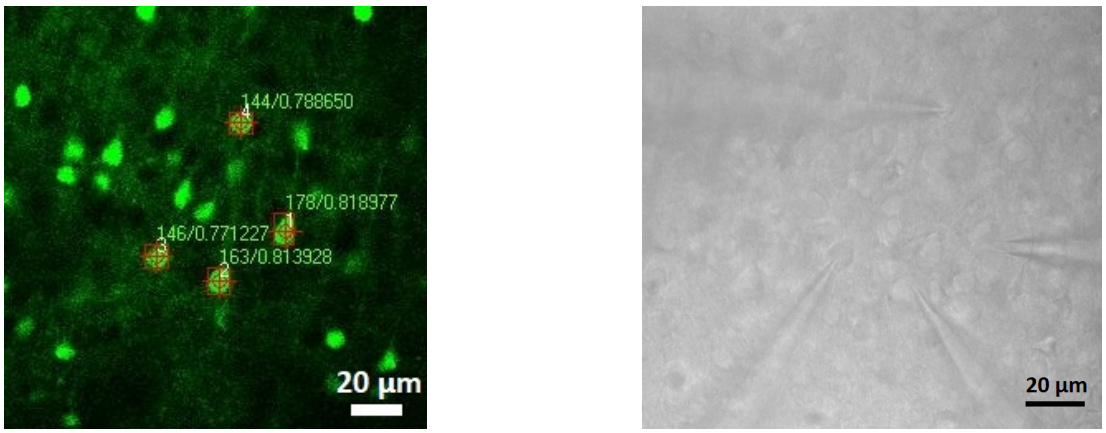


Figure 6.11: The four targeted cells whose resistance and pressure plots can be seen in Fig. 6.12 (for the two successful channels, 2 and 4) and whose injections can be seen in Fig. 6.10 (for the two successful channels, 2 and 4). (Left) The four cells from the trial as seen under two-photon imaging, expressing GFP owing to CamkII-GFP (AAV9) p0 injections. Red circle-cross overlays can be seen due to the tracking that RITA performs on the cells. (Right) The four cells from the trial as seen under IR imaging, during the sealing process.

6.2.2 Example of three successfully patched cells

An example of three cells patched with the newest iteration of the algorithm can be seen in Fig. 6.14, together with their pressure and resistance plots. Channel 1 is not presented because it failed to establish a seal with the targeted cell. Channel 4 is a special, not very common case, where the algorithm broke into the cell before the gigaseal was reached. It was considered a successful WCR despite the gigaseal not being achieved because the resistance did rise significantly, the WCR obtained showed a healthy Vm, input/series resistances were below 100 MΩ and the signal depicted the distinctive break-in shape.

Injections made into these same cells can be seen in Figure 6.15. No connections were found between these cells. Pipettes between 5.14 and 6.03 MΩ were used for this approach. The input resistances for channels 2, 3 and 4 respectively were 46.74, 46.22 and 95.10 MΩ, the series resistances were 19.12, 18.45 and 21.62 MΩ while the resting membrane potentials were -65.54, -59.28 and -64.32 mV.

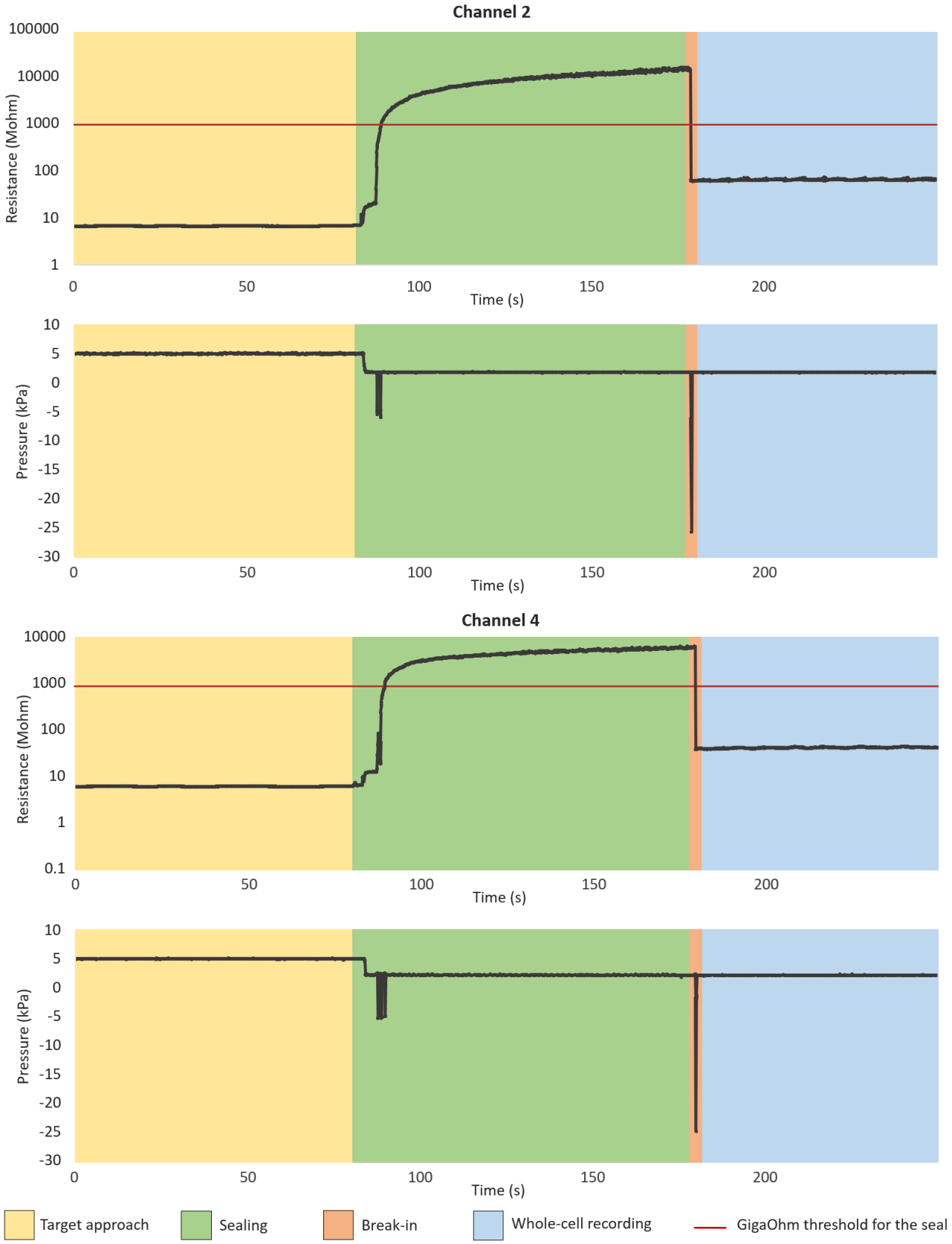


Figure 6.12: Stages of the automated process and corresponding pipette resistance and pressure changes for channels 2 and 4.

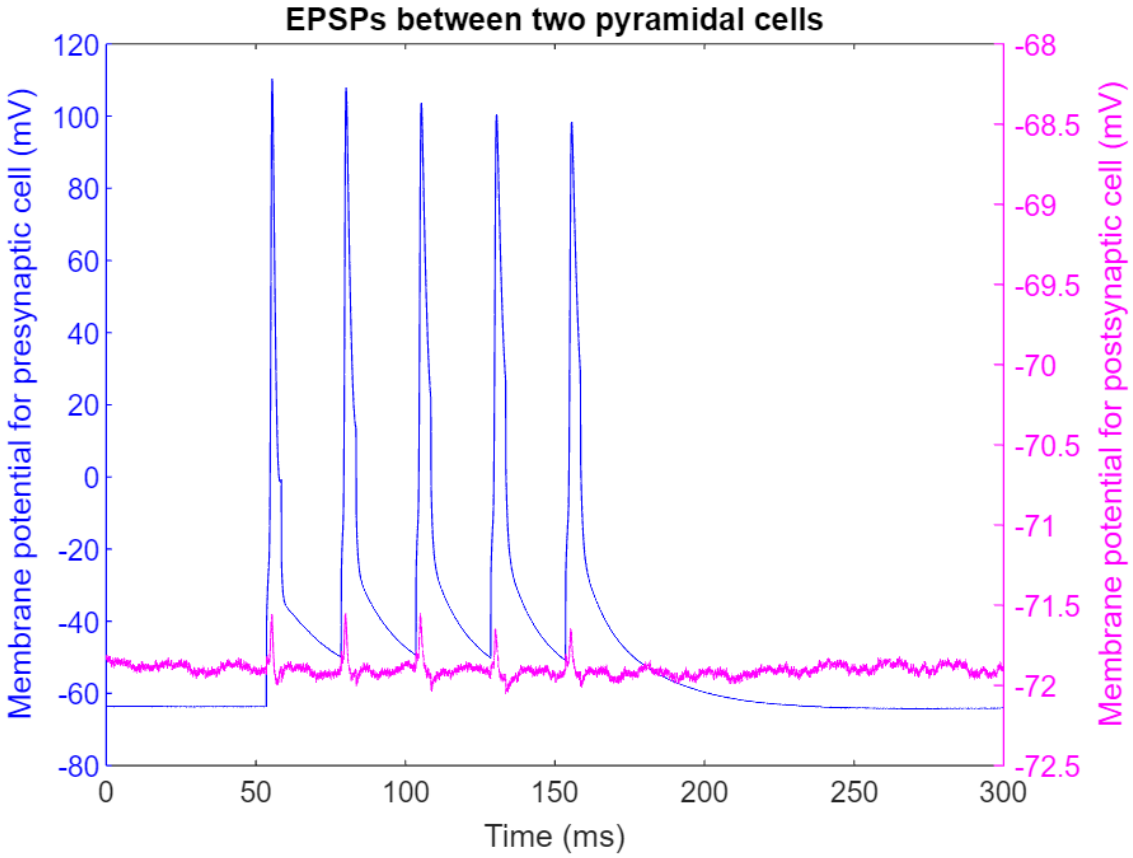
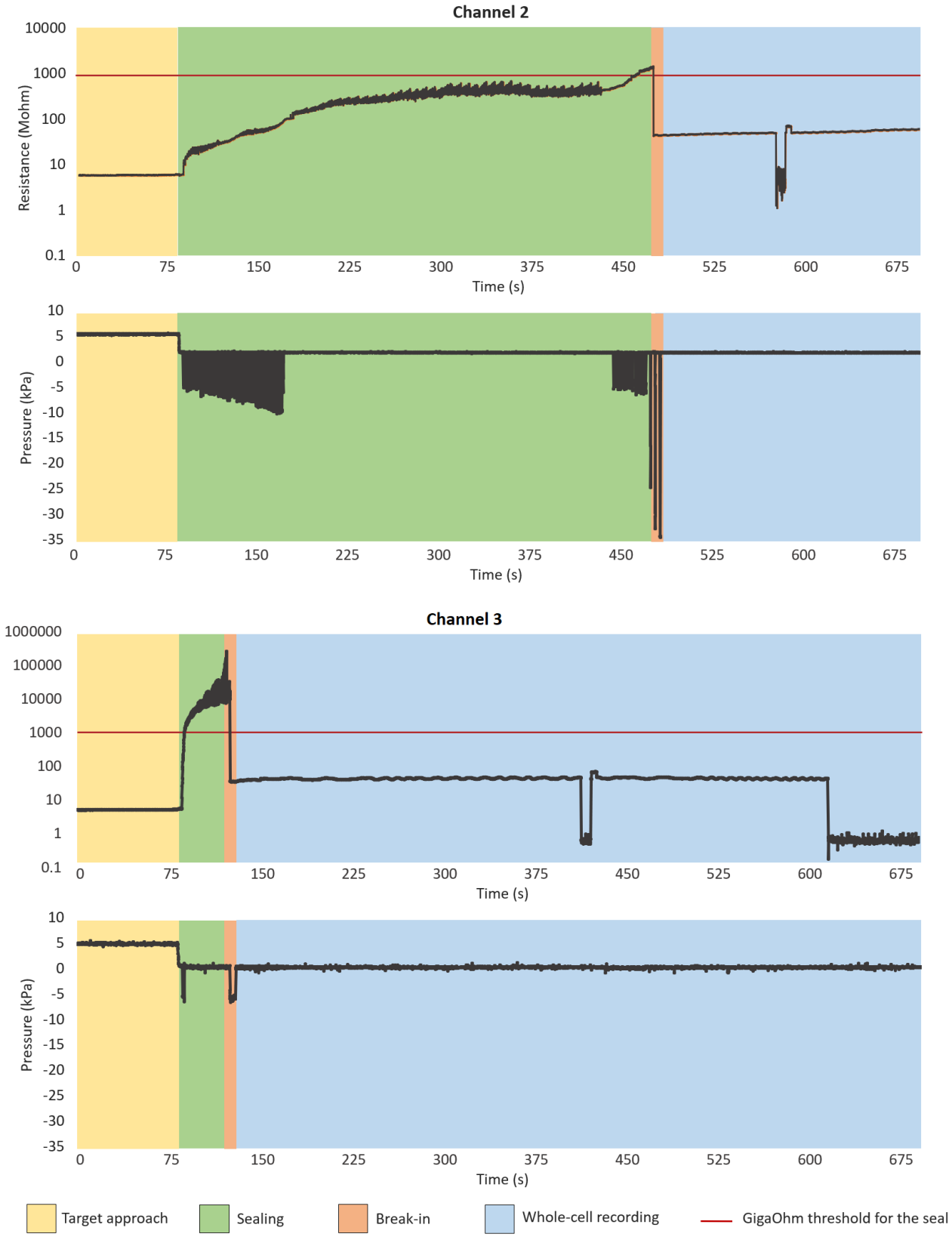
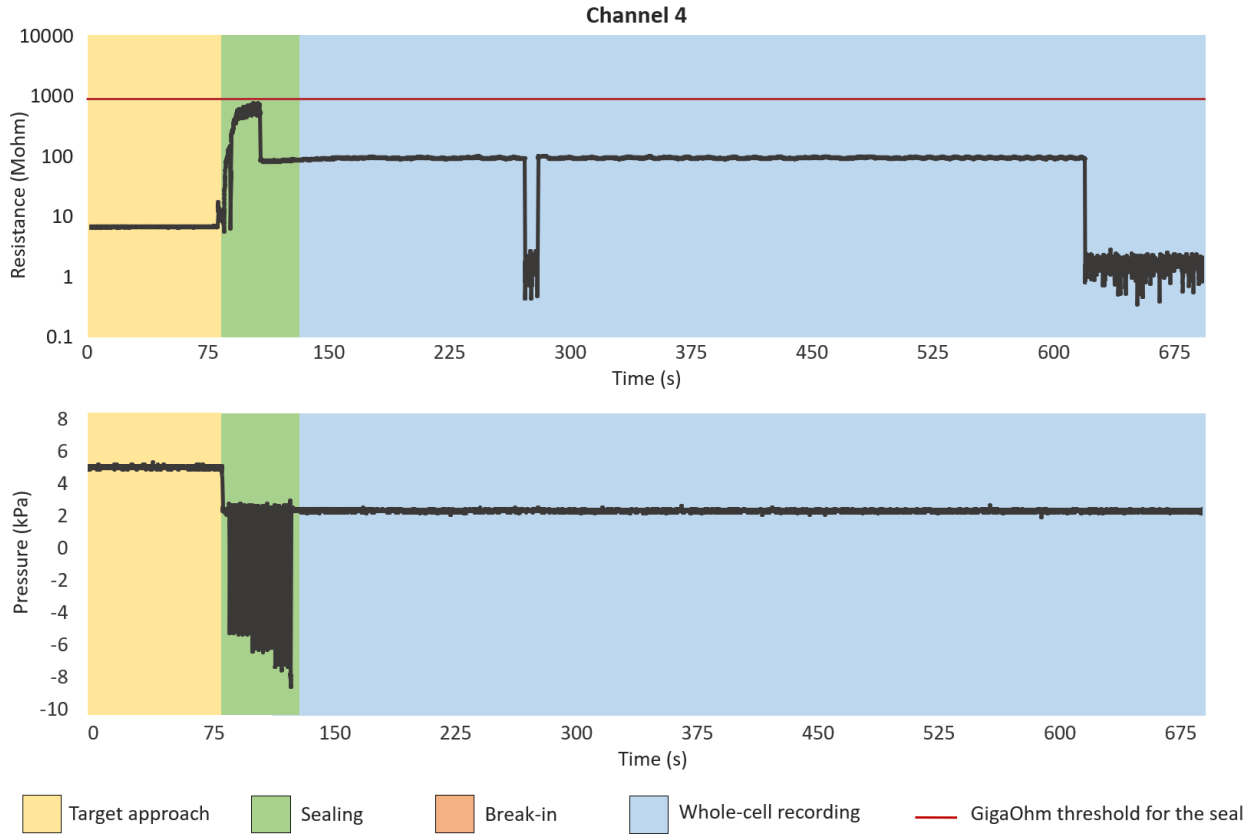


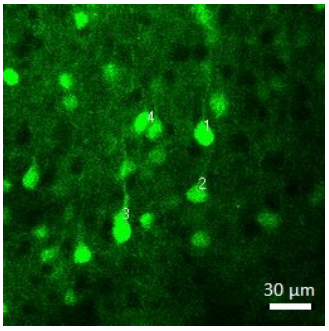
Figure 6.13: Voltage versus time plot from a pair of coupled cells (blue - presynaptic, magenta - postsynaptic). Excitatory Post-Synaptic Potentials (EPSPs) can be observed on the Post cell in response to a 50 Hz, 5-pulse excitatory train on the Pre cell, denoting a facilitating synapse from Pre to Post. Traces are the averages of 30 iterations.


Channel 2
Resistance (Mohm)
10000
1000
100
10
1
0.1
0
75
150
225
300
375
450
525
600
675
Time (s)
Pressure (kPa)
10
5
0
-5
-10
-15
-20
-25
-30
-35
Time (s)
Channel 3
1000000
100000
10000
1000
100
10
1
0.1
Time (s)
Pressure (kPa)
Time (s)
Target approach
Sealing
Break-in
Whole-cell recording
GigaOhm threshold for the seal

(a)



(b)



(c)

Figure 6.14: Example of three successfully patched GFP-expressing cells. (a,b) Stages of the automated process and corresponding pipette resistance and pressure changes for channels 2, 3 and 4. Once the target cell is detected through an impedance increase, sealing automatically begins, which releases positive pressure and applies increasing suction until a gigaseal is formed. Similar, but stronger, suction pulses are applied for break-in. (c) The four cells from the trial as seen under two-photon imaging, expressing GFP owing to CamkII-GFP (AAV9) p0 injections.

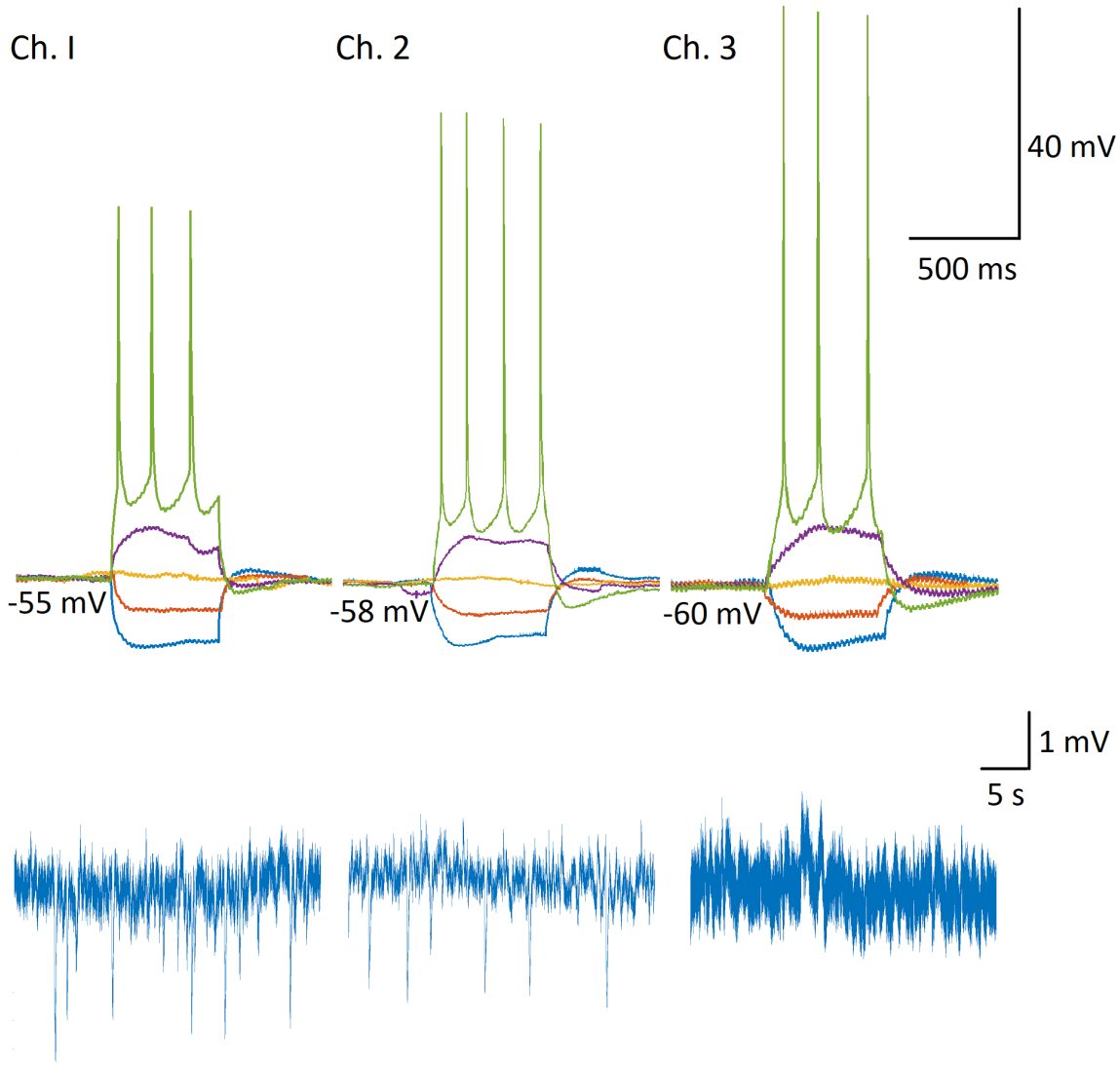


Figure 6.15: Current injections for three two-photon targeted patched cells (CamkII-GFP p0 injections). (Top) Example of the responses of three two-photon targeted patched cells in response to the current pulses applied through our injection protocol module. Voltage responses for the injections of value -40, -20, 0, 20 and 60 pA are presented. (Bottom) Recordings of the same cells with no injections.

6.2.3 Statistics

We do not yet have enough trials to present any statistics as the ones in other sections.

6.3 Conclusion

Robotic automation helps mitigate low success rates in patch-clamp by allowing more trials to be carried out in one experimental day and offers several benefits, including faster skill assimilation for operators new to the technique and improved throughput. It also enables the scaling up of the technique to simultaneous patch-clamp recording of multiple cells *ex vivo* and *in vivo*, enabling assays of synaptic coupling and many new research lines in basic and translational neuroscience. With further increase of the level of automation to include other aspects of experimental workflow, such as craniotomies (Ghanbari et al., 2019), there is the potential for further reduction in human-derived experimental variability.

Our targeted quad patch-clamp system allows scalable and reproducible electrophysiology studies to be conducted across a variety of laboratory settings, offering for the first time, robotically automated recording of subthreshold signals from multiple genetically and optically targeted cells in tandem. As we have made use of an imaging technique that can be translated *in vivo*, we envisage a straightforward extension of the platform from *ex vivo* to *in vivo* application.

Chapter 7

Final discussion and future work

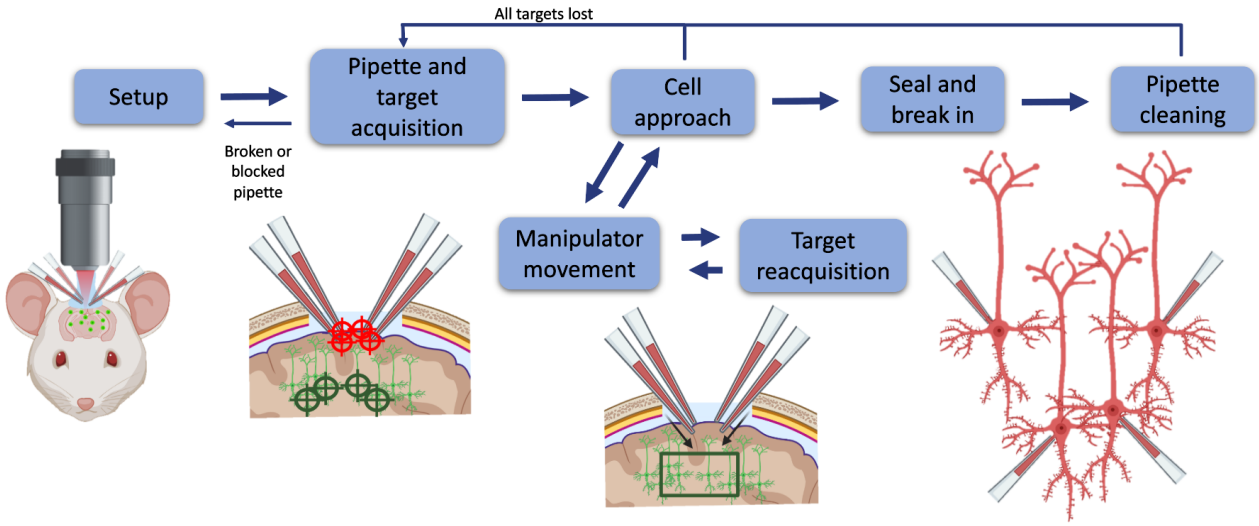


Figure 7.1: Possible algorithm for the *in vivo* mode, where a more iterative approach than the current algorithm might be needed.

Neurological disorders are the second leading cause of deaths worldwide (Feigin et al., 2017). With an increasingly aging population, the number of people affected by neurological disorders will just keep growing. To mitigate the effects, we only have so many tools that can help us understand the brain, both during normal and abnormal behavior. Following a bottom-up approach, we must start by studying the most reduced unit of the system: the cell.

Whole-cell patch-clamp is the gold standard technique to determine cell type and function in electrically active cells like neurons. When patch-clamp is performed simultaneously in multiple neurons, it enables unambiguous measurement of the connectivity between them,

with a spatiotemporal precision unachievable by any other technique, making it possible to understand how cells communicate with each other and function. However, multi-patch-clamp is a very low-throughput, tedious technique and has an extremely steep learning curve, which requires extensive training. Thus, only a few laboratories in the world are capable of it.

The two-photon targeted quad patch-clamp automated system presented in this thesis allows scalable and reproducible high-throughput electrophysiology studies to be conducted across a variety of laboratory settings, offering for the first time robotically automated recording of subthreshold signals from multiple genetically and optically targeted cells simultaneously. RITA achieves a good seal success rate both on 'blind' and two-photon targeted modes, yielding recordings with membrane potential, input and series resistances comparable to manual experiments. Besides the expansion to four channels, a key advance has been made over its predecessor, the work presented in Annecchino et al. (2017), whereby there is no need for manual adjustment of the pipettes before sealing. Furthermore, the pipette cleaning module allows pipettes to be reused, further limiting the attention required from the user, while the 'follow' function facilitates swift movement to new, unpatched brain regions. The system is easy to use and has a software with a friendly user interface and multiple added features. Temperature control for the perfusion system is integrated. The output and cell information of each channel is automatically recorded for each trial. Basic injection and connectivity protocols are also available to run within the program, making the software a complete set for the basic needs of any experimenter, regardless of their skill set.

The system developed during this thesis will not only facilitate the widespread dissemination of the quad patch-clamp technique, but also will increase the throughput. With a reduced time frame as compared to manual experiments, and, most importantly, drastically reduced attention load required from the researcher, any user could potentially attend more than one automated patch-clamp system at a time, increasing throughput. Another advantage to bear in mind is the mental health of the researchers, as this technique is very demanding and frustrating to both learn and perform, and it can be relieved by the system. Finally, given the sanitary measures adopted in the last few years, this robot offers a more health-conscious manner to conduct research.

We have plans to make our technology available to laboratories all over the world by commercializing it through LabMaker, a company which builds and sells open science instruments (who

we are in talks with), but also making it DIY for those who wish to build their own. For the latter, we are creating a website that will contain all relevant (open-access) information.

The system developed can be employed to not only assess cell function and connectivity within brain microcircuits of specific cell subtypes, but also can help determine the responses of specific cell subpopulations to diverse inputs at high throughput. It also has the capability to assess the characteristics and behaviour of labelled cells that have been transfected via viruses, plasmid DNA or peptides that modulate physiological functions. Moreover, after patch-clamp electrophysiological recording and stimulation of a cell, suction could be used to aspirate the contents of the cell, for high-throughput transcriptome sequencing. This was already done by Koos et al. (2021) and could potentially be implemented in our system, for increased throughput (Koos et al. (2021) had a single channel). A compelling case for performing single-cell RNA expression analysis is made by variances in gene expression in rare cell types that make up a modest (often undiscovered) portion of the entire tissue transcriptome (Annecchino, 2016).

The system has been developed with brain slices and will be adapted to *in vivo* mode over the next few months, starting with anaesthetised mice, and finally, in awake mice, if possible.

Most likely, the main obstacles to overcome *in vivo* will be: (1) the target movement induced by the heartbeat and breathing of the mouse, (2) the inability to accurately assess target-cell distance in failed attempts (to optimize targeting) and (3) the potential reduced number of healthy cells available to patch due to the older age of the animals, as they should be 5 to 6 weeks old for head-plate installation (Jordan, 2021), compared to the current 2 to 3 weeks old.

Regarding (1), there are several approaches used to reduce movement as much as possible. On one hand, movement can be reduced by physically restraining the animal. Robust head-plate design and attachment are key, but the use of a thin film of agar on top of the craniotomy has also been proved to help in movement reduction (Jordan, 2021). Furthermore, a retro-fit cranial window insert has also been shown to reduce movement (Dacre et al., 2023). Physical restriction of movement will be specially crucial for the sealing part of the algorithm, whereby sealing can fail due to target movement with respect to the tip. On the other hand, the effects of movement can be minimized through the use of algorithms that take it into consideration. One option is to align the galvanometric mirrors that scan the tissue to the heartbeat of the animal, which has been used to reduce heart movement in the work of Streich et al. (2021) ('ECG gating'). Another option that could potentially adapt our algorithm to an oscillating

target is to align the target scanning and pipette movement to the same time point within the period of the movement. A similar idea is presented in the work of Stoy et al. (2021), where the algorithm compensates for physiological movements during the patch-clamp process, and thus will be a good guide for the task at hand. For the filtering of the signals (to remove oscillations arising from heartbeat and breathing motions), we could develop a baseline wandering removal algorithm (similar to the one proposed in NationalInstruments (2020) or similar to the one in Stoy et al. (2021)).

Another approach that could help regarding (1) would be the use of artificial intelligence (AI) methods for image analysis. While our image processing is clearly effective, the more complicated paradigm of *in vivo* patching might need more evolved solutions. Deficient gene expression on transgenic/virus transfected animals combined with photobleaching and background signal from internal dye and cortical haemorrhage, is a potential concern for cell detection and tracking. Recent publications on patch-clamp automation, like Koos et al. (2021) and Kolb et al. (2019) use machine vision and deep neural networks, respectively, to detect healthy target cells to patch as well as optimizing the automation, with good results. These publications apply AI to infrared-visually-guided systems, but AI has also successfully been applied to track cells and extract features from them in two-photon calcium imaging (Sità et al., 2022). Thus, cell tracking in our system could potentially be improved with AI. Furthermore, our current system struggles to target cells that express calcium dyes like GCaMP, but an algorithm similar to the one in Sità et al. (2022) could potentially adapt the system to work with such samples. This would be extremely beneficial as it could provide a ground truth for the calcium signals, allowing researchers to transform these signals back to action potentials. Not only that, but the combination of multi-patch-clamp with voltage/calcium imaging would help elucidate the cellular or even molecular mechanisms that connect network phenomena with single-cell behaviour.

Regarding (2), we have so far used our infrared imaging to determine the cell to pipette tip distance in failed attempts, which was key in optimizing the targeting algorithm. In two-photon imaging, however, there is no good compromise between having enough dye in the internal solution (so that the pipette is seen) and the dye diffusing throughout, which increases drastically background fluorescence. We opted to have lower background fluorescence (by having really small amounts of dye), which meant that the pipette tip was often indistinguishable from the

background once inside the brain tissue. From general literature, it does seem like this is an issue for most two-photon systems, but to my knowledge, no one has tried finding a balance in the amount of dye by applying AI to infer pipette position (in two-photon imaging; in IR systems it has been done extensively and successfully, as the pipette is very visible). Thus, applying AI machine vision algorithms for pipette detection could be a potential solution to the issue. Another potential solution would be to use quantum dots to line the pipette tips, which makes the tip visible in much deeper tissues and does not affect seal quality (Andrásfalvy et al., 2014). However, this would only be a viable solution if the dots do not affect and are unaffected by pipette cleaning (meaning they are not degraded by the cleaning process and they do not prevent pipettes from being properly cleaned). Thus, further testing would be necessary to corroborate that. Either of these solutions would be helpful when moving to *in vivo* to visualize the pipette during the approach and thus optimize the targeting, but if the current algorithm fails to work and a more iterative approach (like the one in 7.1 is required), pipette visualization would be crucial for optimal targeting. This is because, as proven in section 4.3.9, repeated manipulator movements tend to accumulate error. Given the four channels of the system, however, checking pipette and cell position along the approach would need to be limited to a few times per approach, so as to balance optimal targeting with approach duration. Therefore, it would probably not be as iterative as the work by Annecchino et al. (2017).

Finally, regarding (3), we must bear in mind that we have generally used relatively sparse labelling methods on our young slices (which have many more healthy cells than older ones). If a less sparse labelling method was to be used on the older animals, this could counterbalance the decrease in the number of healthy cells. However, less sparse labelling usually translates to higher background signal from neuropil. This might be counteracted by either soma or nuclei targeted fluorescence, with a virus such as AAV PHP.eB CAG-NLS-GFP (AddGene). This virus achieves good nuclear fluorescence while keeping background fluorescence at bay and has the advantage of being able to express in mice of any age when injected intravenously. Cap-B10 and PHP.eB have emerged as promising viruses, since they can cross the blood-brain-barrier in adult mice, thus making CNS-wide expression possible through, for example, tail injections.

Neuroscience research has made significant advances in the past decades. Even though we now have access to techniques like fMRI and calcium imaging, knowledge about what brain-wide signals mean at the cellular level is still lacking. Unfortunately, techniques (such as

targeted multi-patch-clamp) that can inform on this knowledge gap are usually difficult to perform and do not scale well in the hands of a human operator. Therefore, there is a need for robotic automation in neuroscience, to both scale up and increase throughput and to perform experiments that humans are not capable of. The work developed in this thesis hopes to contribute to a future where researchers that have been trained for years (and whose time is thus extremely valuable) could focus on experiment design and drawing conclusions from the data. Experiments could run with little to no supervision, data analysis pipelines would be automated, and science would progress at an unprecedented rate.

Bibliography

Alegria, A., Joshi, A., O'Brien, J., and Kodandaramaiah, S. B. (2020). Single neuron recording: progress towards high-throughput analysis.

Andrásfalvy, B. K., Galiñanes, G. L., Huber, D., Barbic, M., Macklin, J. J., Susumu, K., Delehanty, J. B., Huston, A. L., Makara, J. K., and Medintz, I. L. (2014). Quantum dot-based multiphoton fluorescent pipettes for targeted neuronal electrophysiology. *Nature Methods*, 11(12):1237–1241.

Annecchino, L. (2016). *Development and validation of a robotic two-photon targeted whole-cell recording system for in vivo electrophysiology*. PhD thesis, Imperial College London.

Annecchino, L. A., Morris, A. R., Copeland, C. S., Agabi, O. E., Chadderton, P., and Schultz, S. R. (2017). Robotic automation of in vivo two-photon targeted whole-cell patch-clamp electrophysiology. *Neuron*, 95(5):1048–1055.

Annecchino, L. A. and Schultz, S. R. (2018). Progress in automating patch clamp cellular physiology. *Brain and Neuroscience Advances*, 2:2398212818776561.

Antzelevitch, C., Pollevick, G. D., Cordeiro, J. M., Casis, O., Sanguinetti, M. C., Aizawa, Y., Guerchicoff, A., Pfeiffer, R., Oliva, A., Wollnik, B., et al. (2007). Loss-of-function mutations in the cardiac calcium channel underlie a new clinical entity characterized by st-segment elevation, short qt intervals, and sudden cardiac death. *Circulation*, 115(4):442–449.

Antzelevitch, C., Sicouri, S., Litovsky, S. H., Lukas, A., Krishnan, S. C., Di Diego, J. M., Gintant, G. A., and Liu, D.-W. (1991). Heterogeneity within the ventricular wall. electrophysiology and pharmacology of epicardial, endocardial, and m cells. *Circulation research*, 69(6):1427–1449.

Bestvater, F., Spiess, E., Stobrawa, G., Hacker, M., Feurer, T., Porwol, T., Berchner-Pfannschmidt, U., Wotzlaw, C., and Acker, H. (2002). Two-photon fluorescence absorption and emission spectra of dyes relevant for cell imaging. *Journal of microscopy*, 208(2):108–115.

Cadwell, C. R., Palasantza, A., Jiang, X., Berens, P., Deng, Q., Yilmaz, M., Reimer, J., Shen, S., Bethge, M., Tolias, K. F., et al. (2016). Electrophysiological, transcriptomic and morphologic profiling of single neurons using patch-seq. *Nature Biotechnology*, 34(2):199–203.

Crochet, S. and Petersen, C. C. (2006). Correlating whisker behavior with membrane potential in barrel cortex of awake mice. *Nature Neuroscience*, 9(5):608–610.

Dacre, J., Sanchez-Rivera, M., Schiemann, J., Currie, S., Ammer, J. J., and Duguid, I. (2023). A cranial implant for stabilizing whole-cell patch-clamp recordings in behaving rodents. *Journal of Neuroscience Methods*, page 109827.

Denk, W., Strickler, J. H., and Webb, W. W. (1990). Two-photon laser scanning fluorescence microscopy. *Science*, 248(4951):73–76.

Desai, N. S., Siegel, J. J., Taylor, W., Chitwood, R. A., and Johnston, D. (2015). Matlab-based automated patch-clamp system for awake behaving mice. *Journal of Neurophysiology*, 114(2):1331–1345.

DeWeese, M. R. (2007). Whole-cell recording in vivo. *Current Protocols in Neuroscience*, 38(1):6–22.

Doetschman, T., Gregg, R. G., Maeda, N., Hooper, M. L., Melton, D. W., Thompson, S., and Smithies, O. (1987). Targetted correction of a mutant hprt gene in mouse embryonic stem cells. *Nature*, 330(6148):576–578.

Dunlop, J., Bowlby, M., Peri, R., Vasilyev, D., and Arias, R. (2008). High-throughput electrophysiology: an emerging paradigm for ion-channel screening and physiology. *Nature reviews Drug discovery*, 7(4):358–368.

Feigin, V. L., Abajobir, A. A., Abate, K. H., Abd-Allah, F., Abdulle, A. M., Abera, S. F., Abyu, G. Y., Ahmed, M. B., Aichour, A. N., Aichour, I., et al. (2017). Global, regional, and national burden of neurological disorders during 1990–2015: a systematic analysis for the global burden of disease study 2015. *The Lancet Neurology*, 16(11):877–897.

Feng, G., Mellor, R. H., Bernstein, M., Keller-Peck, C., Nguyen, Q. T., Wallace, M., Nerbonne, J. M., Lichtman, J. W., and Sanes, J. R. (2000). Imaging neuronal subsets in transgenic mice expressing multiple spectral variants of gfp. *Neuron*, 28(1):41–51.

Finol-Urdaneta, R. K., McArthur, J. R., Aboelela, A., Bujaroski, R. S., Majed, H. H., Rangel, A., Adams, D. J., Ranson, M., Kelso, M. J., and Buckley, B. J. (2022). Automated patch clamp screening of amiloride and 5-n, n-hexamethyleneamiloride (hma) analogs identifies 6-iodoamiloride as a potent acid-sensing ion channel inhibitor. *bioRxiv*.

Fischer, F., Stegen, C. F., Koetzner, C. A., and Masters, P. S. (1998). Construction of a mouse hepatitis virus recombinant expressing a foreign gene. In *Coronaviruses and Arteriviruses*, pages 291–295. Springer.

Foust, K. D., Nurre, E., Montgomery, C. L., Hernandez, A., Chan, C. M., and Kaspar, B. K. (2009). Intravascular aav9 preferentially targets neonatal neurons and adult astrocytes. *Nature Biotechnology*, 27(1):59–65.

Ghanbari, L., Rynes, M. L., Hu, J., Schulman, D. S., Johnson, G. W., Laroque, M., Shull, G. M., and Kodandaramaiah, S. B. (2019). Craniobot: A computer numerical controlled robot for cranial microsurgeries. *Scientific Reports*, 9(1):1–12.

Go, J., Fan, A., Lu, C., Kodandaramaiah, S., Holst, G. L., Stoy, W., Kolb, I., Boyden, E. S., and Forest, C. R. (2013). Fully-automated in vivo single cell electrophysiology. American Society for Precision Engineering.

Haery, L., Deverman, B. E., Matho, K. S., Cetin, A., Woodard, K., Cepko, C., Guerin, K. I., Rego, M. A., Ersing, I., Bachle, S. M., et al. (2019). Adeno-associated virus technologies and methods for targeted neuronal manipulation. *Frontiers in Neuroanatomy*, page 93.

Hamill, O. P., Marty, A., Neher, E., Sakmann, B., and Sigworth, F. (1981). Improved patch-clamp techniques for high-resolution current recording from cells and cell-free membrane patches. *Pflügers Archiv: European Journal of Physiology*, 391(2):85–100.

Helmchen, F. and Denk, W. (2005). Deep tissue two-photon microscopy. *Nature Methods*, 2(12):932–940.

Hillier, D., Fiscella, M., Drinnenberg, A., Trenholm, S., Rompani, S. B., Raics, Z., Katona, G., Juettner, J., Hierlemann, A., Rozsa, B., et al. (2017). Causal evidence for retina-dependent and-independent visual motion computations in mouse cortex. *Nature Neuroscience*, 20(7):960–968.

Hodgkin, A. L. and Huxley, A. F. (1939). Action potentials recorded from inside a nerve fibre. *Nature*, 144(3651):710–711.

Hodgkin, A. L. and Huxley, A. F. (1952). A quantitative description of membrane current and its application to conduction and excitation in nerve. *The Journal of Physiology*, 117(4):500.

Holst, G. L., Stoy, W., Yang, B., Kolb, I., Kodandaramaiah, S. B., Li, L., Knoblich, U., Zeng, H., Haider, B., Boyden, E. S., et al. (2019). Autonomous patch-clamp robot for functional characterization of neurons in vivo: development and application to mouse visual cortex. *Journal of Neurophysiology*, 121(6):2341–2357.

Horton, N. G., Wang, K., Kobat, D., Clark, C. G., Wise, F. W., Schaffer, C. B., and Xu, C. (2013). In vivo three-photon microscopy of subcortical structures within an intact mouse brain. *Nature Photonics*, 7(3):205–209.

Jordan, R. (2021). Optimized protocol for in vivo whole-cell recordings in head-fixed, awake behaving mice. *STAR protocols*, 2(1):100347.

Jouhanneau, J.-S. and Poulet, J. F. (2019). Multiple two-photon targeted whole-cell patch-clamp recordings from monosynaptically connected neurons in vivo. *Frontiers in Synaptic Neuroscience*, 11:15.

Kalmbach, A. S. and Waters, J. (2012). Brain surface temperature under a craniotomy. *Journal of Neurophysiology*, 108(11):3138–3146.

Kitamura, K., Judkewitz, B., Kano, M., Denk, W., and Häusser, M. (2008). Targeted patch-clamp recordings and single-cell electroporation of unlabeled neurons in vivo. *Nature Methods*, 5(1):61–67.

Kodandaramaiah, S. B., Boyden, E. S., and Forest, C. R. (2013). In vivo robotics: the automation of neuroscience and other intact-system biological fields. *Annals of the New York Academy of Sciences*, 1305(1):63–71.

Kodandaramaiah, S. B., Flores, F. J., Holst, G. L., Singer, A. C., Han, X., Brown, E. N., Boyden, E. S., and Forest, C. R. (2018). Multi-neuron intracellular recording in vivo via interacting autopatching robots. *Elife*, 7:e24656.

Kodandaramaiah, S. B., Franzesi, G. T., Chow, B. Y., Boyden, E. S., and Forest, C. R. (2012). Automated whole-cell patch-clamp electrophysiology of neurons in vivo. *Nature Methods*, 9(6):585–587.

Kodandaramaiah, S. B., Holst, G. L., Wickersham, I. R., Singer, A. C., Franzesi, G. T., McKinnon, M. L., Forest, C. R., and Boyden, E. S. (2016). Assembly and operation of the autopatcher for automated intracellular neural recording in vivo. *Nature Protocols*, 11(4):634.

Kolb, I., Landry, C. R., Yip, M. C., Lewallen, C. F., Stoy, W. A., Lee, J., Felouzis, A., Yang, B., Boyden, E. S., Rozell, C. J., et al. (2019). Patcherbot: a single-cell electrophysiology robot for adherent cells and brain slices. *Journal of Neural Engineering*, 16(4):046003.

Kolb, I., Stoy, W., Rousseau, E., Moody, O., Jenkins, A., and Forest, C. (2016). Cleaning patch-clamp pipettes for immediate reuse. *Scientific Reports*, 6(1):1–10.

Komai, S., Denk, W., Osten, P., Brecht, M., and Margrie, T. W. (2006). Two-photon targeted patching (tptp) in vivo. *Nature Protocols*, 1(2):647–652.

Koos, K., Oláh, G., Balassa, T., Mihut, N., Rózsa, M., Ozsvár, A., Tasnadi, E., Barzó, P., Faragó, N., Puskás, L., et al. (2021). Automatic deep learning-driven label-free image-guided patch clamp system. *Nature Communications*, 12(1):1–11.

Lalanne, T., Abrahamsson, T., and Sjöström, P. J. (2016). Using multiple whole-cell recordings to study spike-timing-dependent plasticity in acute neocortical slices. *Cold Spring Harbor Protocols*, 2016(6):pdb–prot091306.

Lampe, S. E. G., Kaspar, B. K., and Foust, K. D. (2014). Intravenous injections in neonatal mice. *Journal of Visualized Experiments: JoVE*, (93):e52037.

Landry, C. R., Yip, M. C., Kolb, I., Stoy, W. A., Gonzalez, M. M., and Forest, C. R. (2021). Method for rapid enzymatic cleaning for reuse of patch clamp pipettes: Increasing throughput by eliminating manual pipette replacement between patch clamp attempts. *Bio-Protocol*, 11(14):4085.

Lin, M. Z. and Schnitzer, M. J. (2016). Genetically encoded indicators of neuronal activity. *Nature Neuroscience*, 19(9):1142.

Long, B., Li, L., Knoblich, U., Zeng, H., and Peng, H. (2015). 3d image-guided automatic pipette positioning for single cell experiments in vivo. *Scientific Reports*, 5(1):1–8.

Lukacs, P., Pesti, K., Földi, M. C., Zboray, K., Toth, A. V., Papp, G., and Mike, A. (2021). An advanced automated patch clamp protocol design to investigate drug—ion channel binding dynamics. *Frontiers in Pharmacology*, 12:738260.

Lundstrom, K. (2001). Alphavirus vectors for gene therapy applications. *Current Gene Therapy*, 1(1):19–29.

MacLean, J. N. and Yuste, R. (2009). Imaging action potentials with calcium indicators. *Cold Spring Harbor Protocols*, 2009(11):pdb–prot5316.

Mainen, Z., Maletic-Savatic, M., Shi, S., Hayashi, Y., Malinow, R., and Svoboda, K. (1999). Two-photon imaging in living brain slices. *Methods*, 18(2):231–239.

Margrie, T. W., Brecht, M., and Sakmann, B. (2002). In vivo, low-resistance, whole-cell recordings from neurons in the anaesthetized and awake mammalian brain. *Pflügers Archiv: European Journal of Physiology*, 444(4):491–498.

Margrie, T. W., Meyer, A. H., Caputi, A., Monyer, H., Hasan, M. T., Schaefer, A. T., Denk, W., and Brecht, M. (2003). Targeted whole-cell recordings in the mammalian brain in vivo. *Neuron*, 39(6):911–918.

Margrie, T. W., Sakmann, B., and Urban, N. N. (2001). Action potential propagation in mitral cell lateral dendrites is decremental and controls recurrent and lateral inhibition in the mammalian olfactory bulb. *Proceedings of the National Academy of Sciences*, 98(1):319–324.

Markram, H., Lübke, J., Frotscher, M., and Sakmann, B. (1997). Regulation of synaptic efficacy by coincidence of postsynaptic aps and epsps. *Science*, 275(5297):213–215.

Mauleon, G., Lo, J. F., Peterson, B. L., Fall, C. P., and Eddington, D. T. (2013). Enhanced loading of fura-2/am calcium indicator dye in adult rodent brain slices via a microfluidic oxygenator. *Journal of Neuroscience Methods*, 216(2):110–117.

Meyer, A. H., Katona, I., Blatow, M., Rozov, A., and Monyer, H. (2002). In vivo labeling of parvalbumin-positive interneurons and analysis of electrical coupling in identified neurons. *Journal of Neuroscience*, 22(16):7055–7064.

Mun, J., Camarena, A., Walker, C., Lin, M. Y., Wolseley, V., Souaiaia, T., Thornton, M., Grubbs, B., Chow, R. H., Evgrafov, O. V., et al. (2020). Robust rna-seq of arna-amplified single cell material collected by patch clamp. *Scientific Reports*, 10(1):1–9.

Nakai, J., Ohkura, M., and Imoto, K. (2001). A high signal-to-noise ca2+ probe composed of a single green fluorescent protein. *Nature Biotechnology*, 19(2):137–141.

NationalInstruments (2018). Cluster control on labview front panel causes high cpu usage. https://knowledge.ni.com/KnowledgeArticleDetails?id=kA00Z0000019SO3SAMl=en-GB [Online; accessed 04-December-2022].

NationalInstruments (2020). Overview of curve fitting models and methods in labview: Removing baseline wandering. https://www.ni.com/en-gb/innovations/white-papers/08/overview-of-curve-fitting-models-and-methods-in-labview.html [Online; accessed 03-December-2022].

NationalInstruments (2022a). Dynamically loading and calling vis. https://www.ni.com/docs/en-US/bundle/labview/page/lvconcepts/dynamic_loadcall_vis.html [Online; accessed 04-December-2022].

NationalInstruments (2022b). Labview tutorial: Getting started with labview programming basics. https://learn.ni.com/learn/article/labview-tutorial [Online; accessed 19-November-2022].

NationalInstruments (2022c). Ni-visa overview. https://www.ni.com/en-gb/support/documentation/supplemental/06/ni-visa-overview.html [Online; accessed 19-November-2022].

Neher, E. and Sakmann, B. (1976). Single-channel currents recorded from membrane of denervated frog muscle fibres. *Nature*, 260(5554):799–802.

NeuromaticDevices (2021). Products. https://neuromaticdevices.com/products/ [Online; accessed 16-March-2021].

Okada, Y. (2012). *Patch clamp techniques*. Springer.

Otsu, N. (1979). A threshold selection method from gray-level histograms. *IEEE Transactions on Systems, Man, and Cybernetics*, 9(1):62–66.

Pattali, R., Mou, Y., and Li, X.-J. (2019). Aav9 vector: a novel modality in gene therapy for spinal muscular atrophy. *Gene Therapy*, 26(7):287–295.

Pei, X., Vidyasagar, T., Volgushev, M., and Creutzfeldt, O. (1994). Receptive field analysis and orientation selectivity of postsynaptic potentials of simple cells in cat visual cortex. *Journal of Neuroscience*, 14(11):7130–7140.

Pei, X., Volgushev, M., Vidyasagar, T., and Creutzfeldt, O. (1991). Whole cell recording and conductance measurements in cat visual cortex in-vivo. *Neuroreport*, 2(8):485–488.

Peng, Y., Mittermaier, F. X., Planert, H., Schneider, U. C., Alle, H., and Geiger, J. R. P. (2019). High-throughput microcircuit analysis of individual human brains through next-generation multineuron patch-clamp. *Elife*, 8:e48178.

Perin, R. and Markram, H. (2013). A computer-assisted multi-electrode patch-clamp system. *Journal of Visualized Experiments: JoVE*, e50630(80).

Petros, T. J., Bultje, R. S., Ross, M. E., Fishell, G., and Anderson, S. A. (2015). Apical versus basal neurogenesis directs cortical interneuron subclass fate. *Cell Reports*, 13(6):1090–1095.

Planert, H., Mittermaier, F. X., Grosser, S., Fidzinski, P., Schneider, U. C., Radbruch, H., Onken, J., Holtkamp, M., Schmitz, D., Alle, H., et al. (2021). Intra-individual physiomic landscape of pyramidal neurons in the human neocortex. *bioRxiv*.

Poulet, J. F. and Petersen, C. C. (2008). Internal brain state regulates membrane potential synchrony in barrel cortex of behaving mice. *Nature*, 454(7206):881–885.

Rahim, A. A., Wong, A. M., Hoefer, K., Buckley, S. M., Mattar, C. N., Cheng, S. H., Chan, J. K., Cooper, J. D., and Waddington, S. N. (2011). Intravenous administration of aav2/9 to the fetal and neonatal mouse leads to differential targeting of cns cell types and extensive transduction of the nervous system. *The FASEB Journal*, 25(10):3505–3518.

Rubenstein, J. and Rakic, P. (2013). *Cellular migration and formation of neuronal connections: comprehensive developmental neuroscience*, volume 2. Academic Press.

Rynes, M. L., Ghanbari, L., Schulman, D. S., Linn, S., Laroque, M., Dominguez, J., Navabi, Z. S., Sherman, P., and Kodandaramaiah, S. B. (2020). Assembly and operation of an open-source, computer numerical controlled (cnc) robot for performing cranial microsurgical procedures. *Nature Protocols*, 15(6):1992–2023.

Sadovsky, A. J. and MacLean, J. N. (2014). Mouse visual neocortex supports multiple stereotyped patterns of microcircuit activity. *Journal of Neuroscience*, 34(23):7769–7777.

Sands, M. S. and Barker, J. E. (1999). Percutaneous intravenous injection in neonatal mice. *Comparative Medicine*, 49(3):328–330.

Sensapex (2021). Sensapex umc automated pressure control. https://www.sensapex.com/products/umc-automated-pressure-control/ [Online; accessed 16-March-2021].

Sensapex (2022). Sensapex ump micromanipulators. https://www.sensapex.com/products/ump-micromanipulators/overview [Online; accessed 14-November-2022].

Simons, T. J. (1988). Calcium and neuronal function. *Neurosurgical review*, 11(2):119–129.

Sità, L., Brondi, M., Lagomarsino de Leon Roig, P., Curreli, S., Panniello, M., Vecchia, D., and Fellin, T. (2022). A deep-learning approach for online cell identification and trace extraction in functional two-photon calcium imaging. *Nature communications*, 13(1):1–22.

Stoy, W. A., Kolb, I., Holst, G., Liew, Y., Pala, A., Yang, B., Boyden, E. S., Stanley, G. B., and Forest, C. R. (2017). Robotic navigation to subcortical neural tissue for intracellular electrophysiology in vivo. *Journal of Neurophysiology*, 118(2):1141–1150.

Stoy, W. M., Yang, B., Kight, A., Wright, N. C., Borden, P. Y., Stanley, G. B., and Forest, C. R. (2021). Compensation of physiological motion enables high-yield whole-cell recording in vivo. *Journal of Neuroscience Methods*, 348:109008.

Streich, L., Boffi, J. C., Wang, L., Alhalaseh, K., Barbieri, M., Rehm, R., Deivasigamani, S., Gross, C. T., Agarwal, A., and Prevedel, R. (2021). High-resolution structural and functional deep brain imaging using adaptive optics three-photon microscopy. *Nature Methods*, 18(10):1253–1258.

Suk, H.-J., Boyden, E. S., and van Welie, I. (2019). Advances in the automation of whole-cell patch clamp technology. *Journal of Neuroscience Methods*, 326:108357.

Suk, H.-J., van Welie, I., Kodandaramaiah, S. B., Allen, B., Forest, C. R., and Boyden, E. S. (2017). Closed-loop real-time imaging enables fully automated cell-targeted patch-clamp neural recording in vivo. *Neuron*, 95(5):1037–1047.

Takada, T., Awaji, T., Itoh, K., Takahashi, R., Shibui, A., Yoshida, K., Sugano, S., Tsujimoto, G., et al. (1997). Selective production of transgenic mice using green fluorescent protein as a marker. *Nature Biotechnology*, 15(5):458–461.

Thomas, K. R. and Capecchi, M. R. (1987). Site-directed mutagenesis by gene targeting in mouse embryo-derived stem cells. *Cell*, 51(3):503–512.

Ting, J. T., Daigle, T. L., Chen, Q., and Feng, G. (2014). Acute brain slice methods for adult and aging animals: application of targeted patch clamp analysis and optogenetics. *Methods Molecular Biology*, (1183):221–242.

Tremblay, R., Lee, S., and Rudy, B. (2016). Gabaergic interneurons in the neocortex: from cellular properties to circuits. *Neuron*, 91(2):260–292.

Tsien, R. Y. (1981). A non-disruptive technique for loading calcium buffers and indicators into cells. *Nature*, 290(5806):527–528.

van Welie, I., Roth, A., Ho, S. S., Komai, S., and Häusser, M. (2016). Conditional spike transmission mediated by electrical coupling ensures millisecond precision-correlated activity among interneurons in vivo. *Neuron*, 90(4):810–823.

Wang, R., Hughes, T., Beck, S., Vakil, S., Li, S., Pantano, P., and Draper, R. K. (2012). Generation of toxic degradation products by sonication of pluronic® dispersants: implications for nanotoxicity testing. *Nanotoxicology*, 7(7):1272–1281.

Wang, X., Zhang, C., Szábo, G., and Sun, Q.-Q. (2013). Distribution of camkiiα expression in the brain in vivo, studied by camkiiα-gfp mice. *Brain Research*, 1518:9–25.

Wellis, D. P., DeFelice, L. J., and Mazzanti, M. (1990). Outward sodium current in beating heart cells. *Biophysical Journal*, 57(1):41–48.

Wu, Q. and Chubykin, A. A. (2017). Application of automated image-guided patch clamp for the study of neurons in brain slices. *Journal of Visualized Experiments: JoVE*, 56010(125).

Wu, Q., Kolb, I., Callahan, B. M., Su, Z., Stoy, W., Kodandaramaiah, S. B., Neve, R., Zeng, H., Boyden, E. S., Forest, C. R., et al. (2016). Integration of autopatching with automated pipette and cell detection in vitro. *Journal of Neurophysiology*, 116(4):1564–1578.

Xu, C. and Webb, W. W. (1996). Measurement of two-photon excitation cross sections of molecular fluorophores with data from 690 to 1050 nm. *Journal of the Optical Society of America B*, 13(3):481–491.

Yang, H. H. and St-Pierre, F. (2016). Genetically encoded voltage indicators: opportunities and challenges. *Journal of Neuroscience*, 36(39):9977–9989.

Yardeni, T., Eckhaus, M., Morris, H. D., Huizing, M., and Hoogstraten-Miller, S. (2011). Retro-orbital injections in mice. *Lab Animal*, 40(5):155–160.

Zhao, Q., Qiu, J., Han, Y., Jia, Y., Du, Y., Gong, H., Li, M., Li, R., Sun, M., and Zhao, X. (2022). Robotic patch clamp based on noninvasive 3-d cell morphology measurement for higher success rate. *IEEE Transactions on Instrumentation and Measurement*, 71:1–12.

Appendices

Appendix A

Instructions to install and assemble the standalone pressure system

A.1 Hardware setup

1. The piece of tubing numbered as (1) in Figure A.1 needs to be connected to a high-pressure source. This might be the one that maintains the air tables stable, the one used in the bath perfusion outlet, a compressed air outlet/tap on the wall or a store-bought air pump. Since the chosen method might provide a different pressure to the one the system was developed/tested in, an initial calibration of the PID controller that adjusts the pressure might be necessary, or/and the pair of manual valves on the acrylic block where (1) connects might need adjusting (the two white and blue valves). See troubleshooting for pressure system calibration.

2. The smaller tubing on the opposite end (number 2) connects to the pressure inlet on the electrode holder (where traditionally there is a syringe that is used as a mouthpiece to do the sealing and break-in).

3. Next, connect the D-sub cable (3) on one end to the black control box, making sure to tighten the screw locking, and on the other end to the D-sub connector on the pneu-

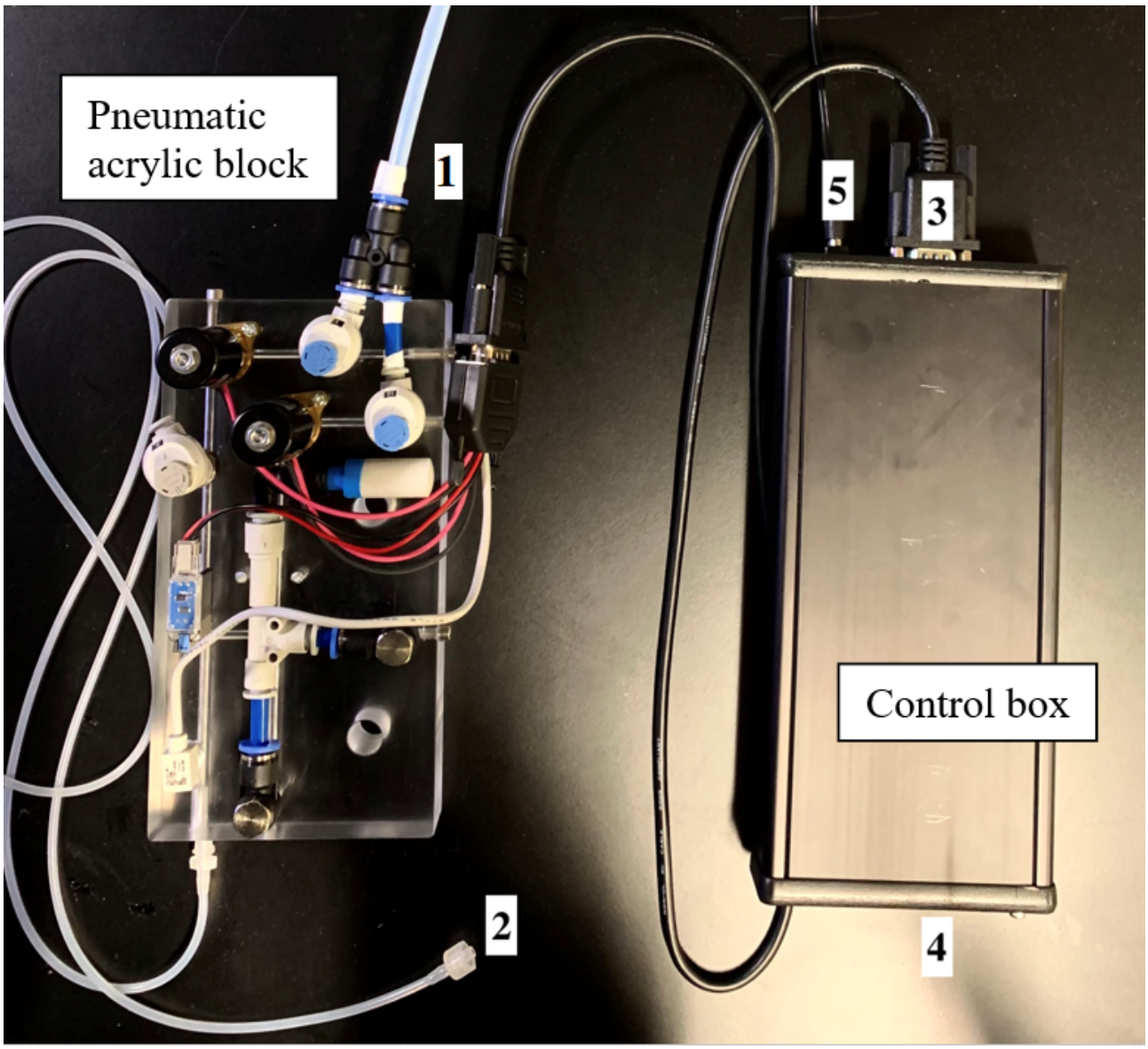


Figure A.1: Numbered and labelled parts of the standalone pressure system.

matic block. The control box houses an Arduino Due and PCB that relay power and sends/receives signals from/to the pneumatic components to the computer.

4. With a USB-A to USB-A cable, connect the USB port on the control box (4) to a USB port on the computer. Once done, note the COM port assigned to the pressure system, as this information is required later on.

5. As a final step, connect the power adapter jack to the control box to power on the system.

A.2 Software installation

The computer where the app will run should have MATLAB installed, as well as the MATLAB Arduino support package. Double click on the app named 'PressureApp.mlappinstall' to install it. Once this is done, the app should appear under the Apps tab in Matlab. Click on the app

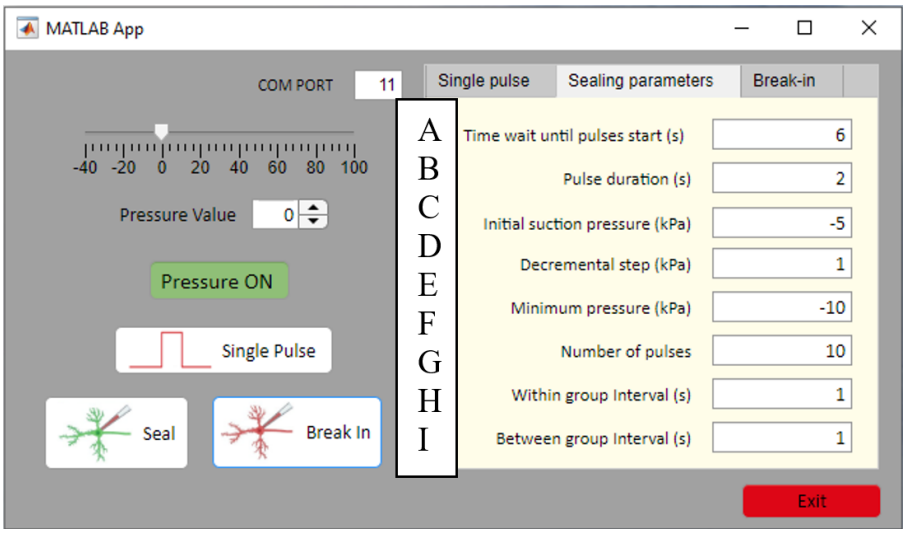


Figure A.2: GUI of the Matlab App.

to open it. Change the COM port to the corresponding one. Then press the 'Pressure OFF' button, which will turn green and read 'Pressure ON'. Pressure can now be applied applied with either the slider on top or by directly inputting the number on the tab underneath, as seen in Figure A.3. The units are in kPa and + 10-15 kPa is recommended for the insertion of the pipette in the brain slice and its movement to the target cell. Once you have approached the cell and observed a dimple, you can press the Seal button. It will change colors once pressed. Once sealing is achieved, unpress the button if it is still applying pressure and press the break-in button. Once break-in is achieved, unpress the button, as, contrary to the sealing one, this will never stop applying suction pulses on its own. If you want to change the pattern of pressure pulses applied, you can do so in the corresponding tabs on the right (this should be done before pressing the corresponding button for the changes to take place).

The predetermined values were found to be good at sealing/break-in, but the user can change them if desired. The idea is that once the button to Seal is pressed, it will release the positive pressure (set the pressure to zero) and wait for the number of seconds denoted in A (6 seconds in the example in Figure A.2). Then it will apply the number of pulses denoted in F, each of B duration in seconds, and C kPa in amplitude. The time wait between pulses is G. Once this

train of pulses is done (10 x 2-second-pulses of -5 kPa, with a 1 second (s) wait between them), it will wait for H seconds before starting a new train of pulses (1 s in the example), this time at C-D kPa (-6 kPa), and this will keep going until the applied pulses are E kPa in amplitude (-10 kPa), at which point it will stop and set the pressure to zero (so in the above example, it will have applied 10 x 2-s-pulses of -5 kPa, 1 s wait, 10 x 2-s-pulses of -6 kPa, 1 s wait, 10 x 2-s-pulses of -7 kPa, 1 s wait, 10 x 2-s-pulses of -8 kPa, 1 s wait, 10 x 2-s-pulses of -9 kPa, 1 s wait and 10 x 2-s-pulses of -10 kPa, unless it was stopped before by pressing the Seal button).

Once done for the day, press EXIT before closing the app window, so that the COM port connection is closed and will work properly the next time.

A.3 Troubleshooting

A.3.1 PID values

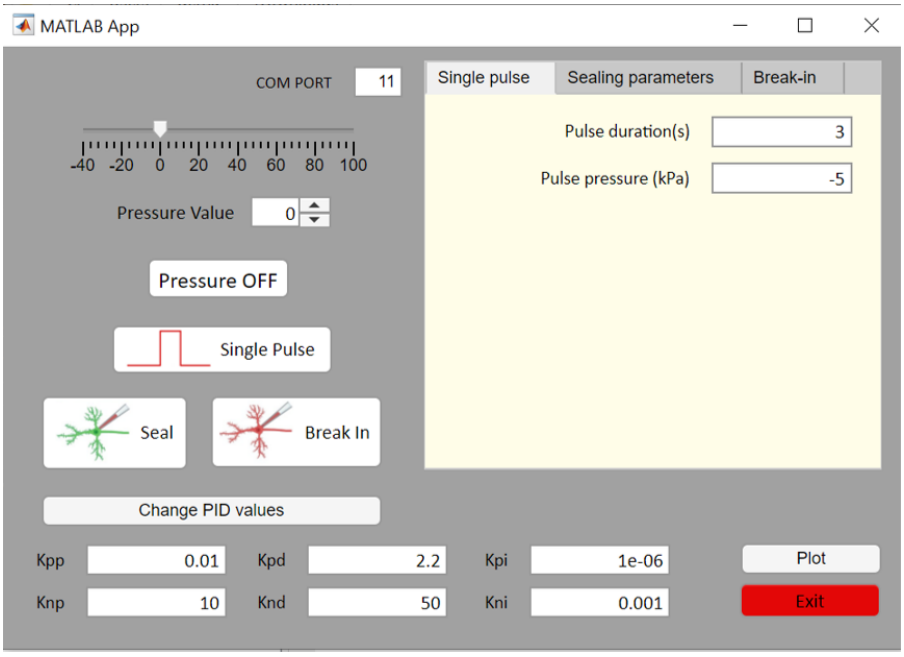


Figure A.3: GUI of the extended Matlab App that allows the user to adjust the PID values.

If the pressure system takes a long time to reach the selected pressure point, it might need a calibration of the PID values. The app 'PressureAppPIDAdjust.mlappinstall' (Figure A.3) should be installed in this case. This app will let the user adjust the PID values by entering the values in the corresponding boxes and clicking on 'Change PID values' button. Changes in

measured pressure can be seen in real time by pressing Plot button. Note this will not work if the pressure is not ON beforehand, and it will stop plotting if the pressure is turned off. Also note that it will only plot once, so if the user wants to plot again, Exit the app and then run it again.

A.3.2 Arduino code

If at some point the app/pressure system randomly stops working, it might need reuploading of the Arduino code, in which case please do install the Arduino IDE software. The version should be Arduino 1.8.10. The Arduino board connected might not be automatically detected by the Arduino IDE, in which case the message 'Board at null is not available' when trying to upload the code will appear. To make the error disappear, follow the subsequent steps:

1. Go to Tools → Board → Board manager
2. Install the Arduino SAM boards (32-bit ARM Cortex-M3) by Arduino version 1.6.12
3. Go to Tools → Programmer and select 'AVR ISP'. See Figure A.4
4. Finally, select Arduino Due: Tools → Board
5. Afterwards, upload the code 'PID_algorithm.ino' by opening it and pressing the forward arrow. The arrow will turn yellow.

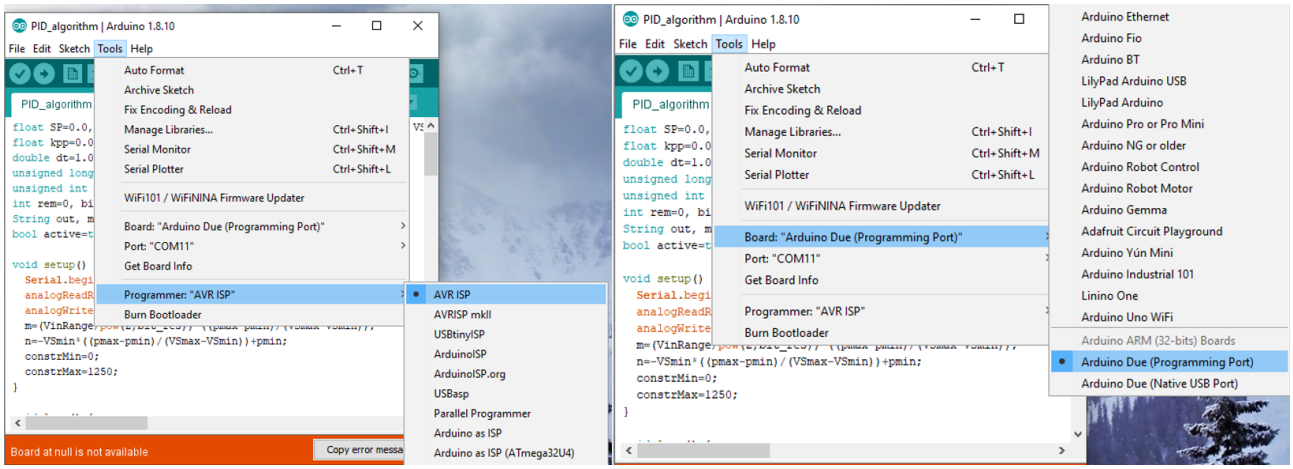


Figure A.4: Reuploading the code to the Arduino Board.

If this process does not solve the issue, a reset of the Arduino board would definitely do.This is done by pressing the reset button on the Arduino board (by opening the black control box) and then reuploading the code.

A.3.3 Incorrect COM port

If MATLAB displays the error message 'Selected COM port is not available', it will likely be one of two reasons: (1) in the previous session the app was not closed properly or (2) the app was opened twice simultaneously. In any of the two cases, close both the app and MATLAB and the error message will disappear.